Aspects of charmonium physics in Lattice QCD

Gabriela Bailas

UNIVERSITÉ CLERMONT AUVERGNE

ÉCOLE DOCTORALE DES SCIENCES FONDAMENTALES

THÈSE

présentée pour obtenir le grade de
DOCTEUR D'UNIVERSITÉ
Spécialité: **PHYSIQUE des PARTICULES**

par

Gabriela BAILAS

Aspects of Charmonium Physics in Lattice QCD

Thèse soutenue publiquement le 27 septembre 2018, devant la commission d'examen:

M. Nicolas Garron	*Rapporteur*
Mme. Mariane Mangin-Brinet	*Rapporteur*
M. Vincent Tisserand	*Président du Jury*
Mme. Asmâa Abada	*Examinateur*
Mme. Hélène Fonvieille	*Examinateur*
M. Vincent Morénas	*Directeur de thèse*

"What you see isn't what you get."

Frank Wilczek

Abstract

Charmonium states provide a relevant source of knowledge for determining fundamental parameters of the Standard Model. An important aspect of understanding Quantum ChromoDynamics (QCD) is to make precise predictions of the hadron spectrum and to test them against high-quality experimental data. Our theoretical framework is Lattice QCD, which is considered to be the only known way to treat the full QCD Lagrangian non perturbatively from first principles, in a manner well suited to numerical computation. By using the Wilson-Clover action with $N_f = 2$ dynamical flavors, we will study the two charmonium mesons η_c and J/ψ. We will also investigate some properties of their first radial excitations $\eta_c(2S)$ and $\psi(2S)$.

Keywords:

Heavy Flavour Physics - Lattice QCD - Standard Model - Charmonium Spectroscopy - Decay constants - Excited States

Résumé

Les états de charmonium fournissent une source de connaissances pertinente pour déterminer les paramètres fondamentaux du Modèle Standard. Un aspect important de la compréhension et des tests de la QCD est de faire des prédictions précises du spectre des hadrons et de les tester par rapport à des données expérimentales de haute qualité. Notre cadre théorique est Lattice QCD, qui est considéré comme le seul moyen connu de traiter le lagrangien QCD complet de manière non perturbative et bien adaptée au calcul numérique. En utilisant l'action Wilson-Clover avec $N_f = 2$ saveurs dynamiques, nous étudierons les deux mésons charmonium η_c et J/ψ. Nous allons également étudier certaines propriétés de leur première excitation radiale $\eta_c(2S)$ et $\psi(2S)$.

Keywords:

Physique des saveurs lourdes - QCD sur le réseau - Modèle standard - Spectroscopie du charmonium - Constantes de désintégration - États excités

Acknowledgements

I would like to thank all the people who contributed positively to the good progress of my PhD. I begin by thanking the Laboratoire de Physique de Clermont (LPC) for the support provided during these three years. Thank you for the funding provided so that I could attend conferences, physics schools and French classes. My thanks to the two LPC directors during my doctorate: Alain Falvard and Dominique Pallin. In addition, I am grateful for the Centre National de la Recherche Scientifique (CNRS) and the Région d'Auvergne for the financial support during my PhD.

I am glad for being part of the LPC theory team and especially I am grateful for my director of these: Vincent Morénas. Thank you for giving me the opportunity to get my PhD. I enjoyed every moment that you dedicated yourself to my work with corrections, rehearsals and advices. This was very important to me. Moreover, I would like to say thanks to the leader of the LPC theory team Ana Teixeira for all her commitment and support during my journey in the LPC.

In addition, my special thanks to the members of the LQCD group of the Laboratoire de Physique Théorique (LPT) - Orsay, particularly to Benoit Blossier who gave me the opportunity to work with him during these three years of PhD.

Finally, I would like to thank all those who have truly supported me during this PhD and know everything I have experienced during my three years. My doctorate was a unique experience and will be unforgettable.

To my beloved family.

Contents

List of Figures

List of Tables

Chapter 1

Introduction

Quantum Chromodynamics (QCD) is the theory of strong interactions. At short distances (at high energy scales), the strong coupling constant becomes small (asymptotic freedom), and it is possible to make theoretical predictions based on perturbation theory. However, at long distances (or low energy scales), the strong coupling increases and perturbation theory is no longer valid: quarks and gluons cannot be seen as asymptotic states but are bound into hadrons. Hence, nonperturbative techniques are necessary to perform calculations of quantities that are sensitive to the long distance behavior of QCD.

Lattice QCD (LQCD) is the only available method to calculate physical observables in a non-perturbative way from first principles, in which all sources of systematic errors can be kept under control and the precision can be systematically improved. It is a specific regularization of the QCD Lagrangian, convenient for numerical studies, where space-time is discretized into a hypercubic lattice. Quarks are restricted to occupy the sites of the lattice, and gluons are the links connecting the sites. LQCD calculations have made major strides in the last decade, and are now playing an important role in constraining the Standard Model (SM) [1]. LQCD was formulated in such a way that computational physics can be applied to calculate properties of QCD without relying on approximations.

The production and decays of charmed states can provide rich information on how strong interactions manifest themselves in ordinary matter [2]. In particular, charmonium ($c\bar{c}$) physics is both a challenging and promising topic for lattice QCD simulations and there are accurate experimental results that can serve as a precision test, provided all systematic errors are under control. Such states occupy a valuable intermediate position within QCD, being neither in the purely non-relativistic regime nor in the regime in which chiral symmetry breaking dominates. This makes the charmonium a relatively clean system to study non-perturbative QCD dynamics, using for example QCD-inspired quark-potential models as well as lattice QCD, which have been successful in describing the observed features of the charmonium spectrum [3, 4].

Nevertheless, not all charmonium states are well characterized. In recent years new charmonium resonances have been discovered in experiments, but they cannot be easily reconciled with the predictions of simple quark-potential models. New investigations of properties

of these states can give useful information about heavy quark dynamics. On the one hand, charmonium states are well established below the heavy flavor meson pair ($D\bar{D}$) production threshold. On the other hand, there are many charmonium and charmonium-like states above this ($D\bar{D}$) threshold, which have not been yet identified as charmonium states[1]. For a wide discussion on the topic see, for example Refs. [5–7].

Moreover, the observation of many new $c\bar{c}$ states at various dedicated facilities such as those carried by the BABAR [8], Belle [9], CLEO [10] and BES-III [1] collaborations, have fueled the research efforts in this sector. These new investigations have increased the challenges in the theoretical understanding of heavy hadrons and have provided new tools to explore these bound states in QCD.

Charmonium states like η_c have been observed to have partial widths consistent with quark model predictions. Moreover, η_c can decay into two gluons [11], which accounts for a substantial portion of the hadronic decays for states below the $c\bar{c}$ threshold. Similarly, the phenomenological studies of the small$-x$ gluon distribution function from the inclusive production of η_c require the knowledge of the decay constant f_{η_c} [12]. Other studies have investigated the possibility of the J/ψ (another charmonium state) to form bound states with nuclei [13], due to its attractive interaction with nuclear matter [14]. Furthemore, η_c and J/ψ can be helpful in describing the non-leptonic B-decays and to check deviations between experimental measures and theoretical results [1]. These bound states are clearly important to increase the accuracy of the predictions of masses, decay constants and widths for all experimentally-accessible $c\bar{c}$ mesons.

In this work, we focus on studying the mass spectrum and the decays of the ground and the first radially excited states of the pseudoscalar and the vector mesons η_c and J/ψ. Among the techniques used in lattice hadron spectroscopy, one has variational methods which can give access to the excited states. In this work, we will use a tool derived from this method: the *Generalized Eigenvalue Problem* (GEVP).

This thesis is organized as follows. The first three chapters introduce the basic concepts, which are applied to the computation of observables, which is done in the remaining chapters of this document. We introduce in Chapter 2 the basics of both Quantum Chromodynamics and LQCD. We also provide the ingredients of LQCD which will be used in the following chapters. In particular, we describe the discretization of the QCD action, and the construction of both fermion and gluon actions on the lattice. In Chapter 3, we discuss the procedure to compute observables. We explore the formalism of Path Integrals and Monte Carlo techniques. We also present the correlation functions, which are used to extract masses and decay constants. Another topic of interest exposed is the estimation of errors in our computations. In Chapter 4, we explain why lattice calculations of excited state properties are challenging and we discuss methods used for excited-state spectroscopy. In particular, we introduce our

[1] Some of these states have unusual quantum numbers and they can not be reached by pure quark states.

method of choice, the Generalized Eigenvalue Problem. In Chapter 5 we use the techniques introduced in the previous chapters to study the spectroscopy of charmonium states. We motivate our investigation by commenting on the experimental situation concerning such states. Then, we explain how we have applied the method described in Chapter 4 in order to suit our purpose. A full description of this method can be found in Appendix B. Chapter 6 is devoted to our analysis and results. We will provide the results of a lattice study considering $N_f = 2$ dynamical quarks, as mentioned before. Moreover, we will compare our results to those available in the literature. To conclude, we will summarize our main findings and outline a few possibilities to extend our research in Chapter 7.

Chapter 2

Lattice QCD

In the low-energy regime of QCD, the strong coupling is large and the use of non-perturbative techniques is mandatory in order to determine the properties of QCD. The most promising method is called Lattice QCD. It is a lattice gauge theory first introduced by Wilson in 1974 [15] and which is still being improved. This procedure provides a regularization of QCD by a grid in four-dimensional Euclidean space time, which enables ab-initio calculations of strongly interacting phenomena in the non-perturbative regime. For calculations one applies the path integral quantization and obtains integrals similar to those in statistical physics.

In lattice QCD, quark fields are located at the lattice sites, while the gluon fields are located on the links connecting neighboring sites (see Fig. 2.1). Two neighboring lattice points are separated by what is known as the lattice spacing a. When the size of the lattice is taken to be infinitely large and its sites infinitesimally close to each other, the continuum QCD is recovered.

With LQCD, it is possible to extract non perturbatively, for example, masses, decay constants and form factors from hadronic transition amplitudes. Currently, LQCD is the only known method to solve the QCD theory from first principles, without perturbative developments nor approximations. In principle, in this approach we do not need to introduce extra parameters besides the bare coupling and the quark masses. The predictions made by LQCD should match the experimental data in order to test the reliability of QCD as the theory of strong interactions.

In the following sections we will discuss the Standard Model of Particle Physics and QCD as well as Lattice QCD.

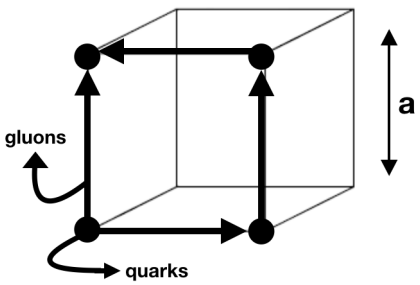

FIGURE 2.1: Lattice QCD symbolic representation.

2.1 Standard Model

The Standard Model is a relativistic quantum field theory and was formulated during the sixties in order to describe the fundamental particles. The SM can account for a huge range of physical phenomena and it is considered one of the most successful models in Physics. This theory involves three of the four fundamental forces: strong, weak and electromagnetic.

The SM particles are classified in four fundamental groups: quarks, leptons, gauge bosons (force mediators) and the Higgs boson. The quarks and leptons (also known as fermions) are the fundamental matter constituents and the interactions between these particles are mediated by (gauge) bosons. All elementary particles of the SM have been experimentally (directly or indirectly) discovered (see Fig. 2.2). The Standard Model is a non-abelian gauge theory and combines the QCD (the theory of strong interaction) and the electroweak (EW) theory (the theory of weak and eletromagnetic interactions) in a single gauge theory based on the symmetry group $SU(3)_C \times SU(2)_L \times U(1)_Y$. The group $SU(3)_C$ is the gauge group of QCD, where the massless gauge field of this theory is the gluon. The group $SU(3)$ has eight generators, which means there are eight types of gluons predicted by the theory. The gauge symmetry $SU(2)_L \times U(1)_Y$ is related to the EW theory. In this case we have three massive weak gauge bosons (W^+, W^- and Z) and one massless gauge boson, the photon. Then, the SM has a total of twelve gauge bosons: the photon, three weak bosons and eight gluons.

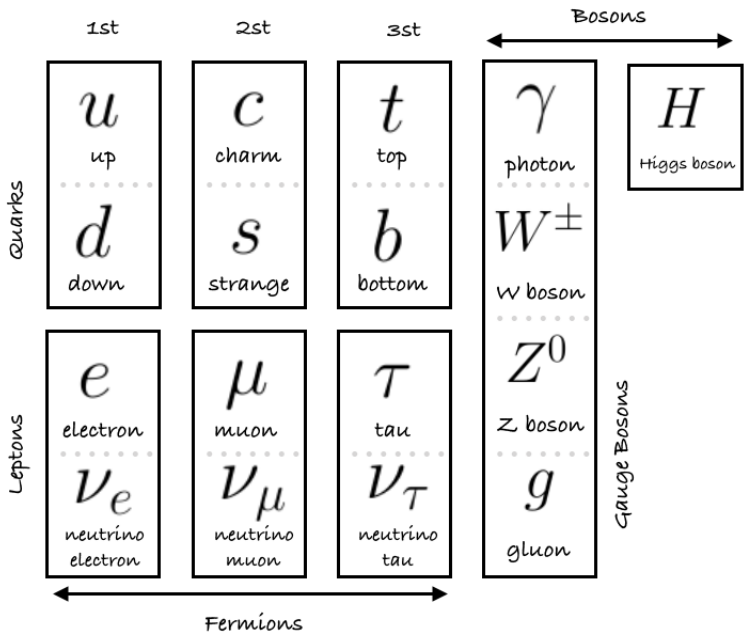

FIGURE 2.2: The elementary particles of the Standard Model.

Fermions

The SM contains 24 (particles and antiparticles) spin 1/2 fermions divided into two groups: quarks and leptons. Moreover, each of these fermions has a corresponding antiparticle. Fermions obey the Pauli exclusion principle. In the Standard Model, there are $N_f = 6$ different flavours

of quarks named up (u), down (d), strange (s), charm (c), botton (b) and top (t) and six leptons named electron (e), e-neutrino (ν_e), muon (μ), μ-neutrino (ν_μ), tau (τ) and τ-neutrino (ν_τ). Pairs of quarks or leptons are grouped together, according to their flavour quantum number and mass, to form a generation (there are three generations - see Fig. 2.2 and Table 2.1).

The most important property of quarks is that they carry a color charge, enabling them to interact through the strong force, while leptons (blind to color) cannot. As a consequence, there is a phenomenon known as color confinement, which makes these particles strongly bound to each other, forming composite states called hadrons. A hadron can be made of a quark-antiquark pair (mesons) or three quarks (baryons). In other words, it is not possible to observe an isolated quark and in the regime of low-energies, quarks are always bounded inside hadrons. Quarks carry also an electric charge and a weak isospin, and they interact with all the other particles by electromagnetic and weak interactions.

The leptons, as mentioned before, do not carry color charge. The three neutrinos (ν_e, ν_μ and ν_τ) do not carry electric charge either, so they interact only through the weak force. On the other hand, the electron, the muon and the tau, carry electric charge and are sensitive to electromagnetic interactions.

Gauge Bosons

The gauge bosons are known as the force carrier of the strong, weak and electromagnetic interactions (see the Table 2.2). They have a spin equal to 1. One of the gauge bosons is the photon (γ), which is the mediator of the electromagnetic force between electrically ($U(1)_{EM}$) charged particles[1]. It has no mass. The bosons W^+ and W^-, together with the boson Z^0, are the mediators of the weak interaction between the different fermions. They are massive. W^+ and W^- carry, respectively, an electric charge of $+1$ and -1, while the Z^0 boson is electrically neutral. The eight gluons mediate the strong interaction between quarks (color charged particles) as well as between themselves since they carry also a color charge.

Higgs Boson

The Higgs boson is another massive elementary particle from the SM. The Higgs boson was experimentally discovered by the ATLAS and CMS experiments in 2012 [16]. In the SM, the Higgs particle is a boson with spin zero, no electric charge and no color charge. Moreover, the origin of mass in the SM is a consequence of the spontaneous symmetry breaking (SSB) of the $SU(2)_L \times U(1)_Y$ into $U(1)_{EM}$, triggered by the Higgs mechanism (see, for example, Refs. [17–20]).

[1] We work here with the electroweak $SU(2)_L \times U(1)_Y$ symmetry which is spontaneously broken to the electromagnetic $U(1)_{EM}$ symmetry.

	Leptons			Quarks		
	Particle	Q	Mass (GeV)	Particle	Q	Mass (GeV)
First Generation	electron	-1	5.1×10^{-4}	up	-1/3	0.002
	neutrino electron	0	$< 2 \times 10^{-8}$	down	+2/3	0.005
Second Generation	muon	-1	0.105	charm	-1/3	1.28
	neutrino muon	0	$< 1.9 \times 10^{-4}$	strange	+2/3	0.095
Third Generation	tau	-1	1.78	top	-1/3	173
	neutrino tau	0	< 0.018	bottom	+2/3	4.18

TABLE 2.1: The Standard Model fermions classified by their charges and masses. From Ref. [21].

Force	Boson	Spin	Mass/GeV
Strong	Gluon	1	0
Electromagnetism	Photon	1	0
Weak	Z boson	1	80.4
	W boson	1	91.2

TABLE 2.2: The gauge bosons of the Standard Model. From Ref. [21].

2.2 Quantum Chromodynamics

QCD is a non-abelian gauge field theory, which describes the strong interactions (between quarks and gluons). It is a quantum field theory gauged by the $SU(3)_C$ symmetry group. The parameters of this theory are the quark masses and the strong coupling constant. Quantum ChromoDynamics has been studied for over more than fourty years and work is still ongoing as, for example, the many open questions related to the non-perturbative domain (such as confinement and hadronization) which are still to be addressed. Moreover, other observables like decay constants and form factors need to be computed more precisely. In the search for new physics, the background of QCD should be studied and understood as much as possible and all QCD parameters need to be measured as precisely as possible.

In the following sections some of the important features of this theory will be developed.

The QCD Lagrangian Density

The full QCD Lagrangian density in Minkowski space-time is given by

$$\mathcal{L}_{QCD}(x) = \sum_{f=1}^{N_f} \sum_{c=1}^{3} \bar{\psi}_{f,c}(x)(i\gamma^\mu D_\mu - m_f)\psi_{f,c}(x) - \frac{1}{4} F^a_{\mu\nu} F^{a\mu\nu} \tag{2.1}$$

where γ^μ are the Dirac γ-matrices, $\psi_{f,c}$ are quark field spinors for a quark of flavor f and mass m_f. The color-index is denoted by c. In eq. (2.1), the covariant derivative is defined by

$$D_\mu \equiv \partial_\mu - i g_s \sum_{a=1}^{8} A^a_\mu(x) \frac{\lambda_a}{2} \tag{2.2}$$

where λ_a stands for the Gell-Mann matrices (generators of $SU(3)$) and g_s is the strong coupling of the theory. The four-vector $A^a_\mu(x)$ with Lorentz index $\mu = 0, 1, 2, 3$ corresponds to the gluon field. The color index a in the gluon field runs from $a = 1$ to 8, which means that there are eight types of gluons. Finally, the field strength tensor is given by

$$F^a_{\mu\nu} \equiv \partial_\mu A^a_\nu - \partial_\nu A^a_\mu + g_s f^{abc} A^b_\mu A^c_\nu \tag{2.3}$$

The last term of the eq. (2.3) is responsible for the gluon field self-interaction. The f^{abc} factors are the structure constants of the $SU(3)$ group and they are defined by the commutation relations

$$[\lambda^a, \lambda^b] = i f^{abc} \lambda^c \tag{2.4}$$

Hence, the generators do not commute, so the $SU(3)$ group is non-abelian, which is at the source of gluon self-interactions (cf. last two diagrams of Fig. 2.3).

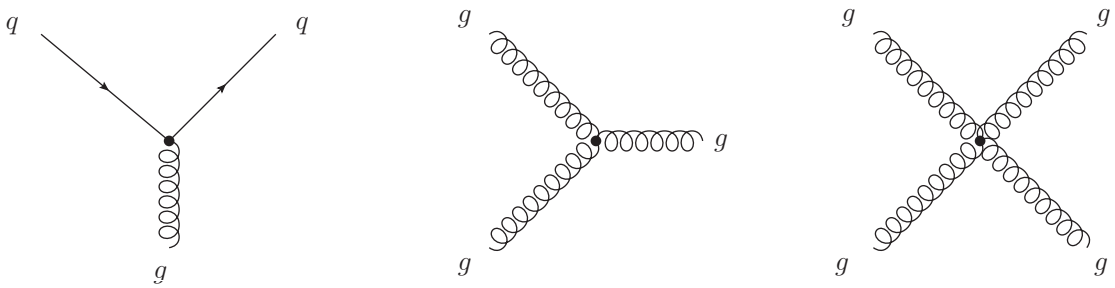

FIGURE 2.3: Feynman diagrams of the QCD Lagrangian for the quark-gluon vertex, the cubic and the quartic self-interactions of gluons.

The QCD coupling constant gives the interaction intensity, and it depends on the energy scale according to renormalization. Then, the relation for the one-loop running coupling constant in QCD is

$$\alpha_s(Q^2) = \frac{1}{\beta_0 \ln(\frac{Q^2}{\Lambda^2_{QCD}})} \tag{2.5}$$

where $\beta_0 = \left(11N_c - 2N_f\right)/12\pi$. The Λ_{QCD} parameter is not predicted by QCD: it should be inferred by experimental data. Since QCD has $N_c = 3$ and $N_f \leq 6$ fermions, the parameter β_0 will be always positive. We can understand from eq. (2.5) the origin of both regimes of QCD. Because $\beta_0 > 0$ we find that $\alpha_s \to 0$ for $Q^2 \to \infty$. This vanishing coupling is named *asymptotic freedom* and is responsible for the fact that quarks behave like free particles at short distances. At Q^2 values close to Λ, the coupling constant becomes large and perturbative QCD breaks down. As previously mentioned, the fundamental parameters of QCD are the coupling g_s (or $\alpha_s = g_s^2/4\pi$) and the quark masses m_q.

2.3 From Minkowski to Euclidean space-time

As will be explained in a coming chapter, one can extract the observables of interest from correlation functions, which can be expressed in terms of path integrals. In this formalism, the weight associated to each path is $e^{iS_{\text{QCD}}}$ where S_{QCD} stands for the action evaluated along the path considered. However, the complex variable i can make the integrand oscillate rapidly for small variations of S_{QCD}, which is a problem for numerical simulations. The usual method to circumvent this problem is to work in Euclidean space-time, after performing a Wick rotation

$$x_0 \to -ix_4 \ , \ \ x_i \to x_i \tag{2.6}$$

In Euclidean space-time $e^{iS_{\text{QCD}}} = e^{-S^E_{\text{QCD}}}$ where the QCD Euclidean action is given by

$$S^E_{\text{QCD}} = \int d^4x \left(\sum_{f=1}^{N_f} \sum_{c=1}^{3} \bar{\psi}_{f,c}(x)(\gamma^E_\mu D_\mu + m_f)\psi_{f,c}(x) + \frac{1}{4} F^a_{\mu\nu} F^{a\mu\nu} \right) \tag{2.7}$$

The Euclidean scalar product is $a^\mu b_\mu = \sum_{\mu=1}^4 a_\mu b_\mu$ and γ^E_μ are the Euclidean gamma matrices. In this formulation, the physical results are obtained by rotating back to Minkowski space-time. However, many important quantities like masses, decay constants and form factors are directly accessible from the Euclidean formulation. The Wightman axioms [22] and the Osterwalder-Schrader theorem [23, 24] give the equivalence between Euclidean and Minkowski formulation. The Wightman axioms allow for an analytic continuation from Minkowski to Euclidean space-time while the Osterwalder-Schrader theorem states that, given some conditions, the reverse operation is also justified.

In the following, we always work in Euclidean space-time so we will drop the subscript E. The scalar product also stands for the Euclidean scalar product except when otherwise stated.

2.4 Discretizing the QCD action

Discretizing space-time amounts to replace an infinite volume of continuous space-time points with a lattice of points in a finite volume Λ, of size $L^3 \times T$, with a lattice spacing a (isotropic lattice)

$$\Lambda \equiv \{x = (n_1, n_2, n_3, n_4)a \ ; \ \ (n_1, n_2, n_3) \in [0, L-1] \ , \ n_4 \in [0, T-1]\} \tag{2.8}$$

where L and T are, respectively, the size of the spatial and temporal extension of the lattice. In LQCD, the quark-fields are located at each lattice site

$$\psi(x), \bar{\psi}(x), \ \ x \in \Lambda, \ \ x = na \tag{2.9}$$

Moreover, they carry the same color, Dirac and flavor indices as in the continuum (they were suppressed for simplicity). By limiting the space-time to a finite hypercubic lattice, the number of degrees of freedom is considerably reduced and the phase space decreases. As a consequence, Monte Carlo techniques are employed in order to generate the gauge fields. The introduction of a hyper-cubic lattice breaks Lorentz invariance, however this is restored when the continuum limit is taken. The continuum QCD Lagrangian is transcribed to the lattice using finite difference techniques. In the lattice QCD formulation the gauge invariance is keep explicitly. The quark fields are located on the sites of the lattice. The gauge fields connect adjacent lattice points. In the following sections we will study transcription for lattice in more detail.

2.4.1 Boundary Conditions

In Lattice QCD, we simulate a finite box. In order to maintain translational invariance, boundary conditions are imposed. For fermions, in order to preserve the translational symmetry, all space directions are set up with periodic boundary conditions [25]. For the time direction for reconstruction of Hilbert space from the Euclidean space, the anti-periodic boundary condition is used [26, 27]. And for the gauge field, one chooses periodic boundary conditions in space and time. Periodic and anti-periodic boundary conditions correspond to a torus in four dimensions, where each direction behaves like a circle. The toroidal boundary conditions preserve the discrete translation symmetry of the lattice.

2.4.2 Gauge Field on the Lattice

The next step is the discretization of the gauge field, A^a_μ, while preserving the local gauge invariance of the theory. In the continuum, the gauge fields $A^a_\mu(x)$ carry 4−vector Lorentz indices and mediate interactions between fermions. In order to write them on the lattice, Wilson proposed to associate gauge field variables with links that connect sites [15]. The discretized version of a path ordered product proposed by him, denoted the gauge link, is defined by

$$U(x, x + a\hat{\mu}) \equiv U_\mu(x) = \exp\left(ig_s a A_\mu(x + \frac{\hat{\mu}}{2})\right) \tag{2.10}$$

where $\hat{\mu}$ is a unit vector pointing in the μ direction. The link matrix in (2.10) is associated to each link of the lattice: it corresponds to the parallel transporter from $x + a\hat{\mu}$ to x. The set for all μ and for all lattice points x of $U_\mu(x)$ is named *gauge configuration*. A configuration is the possibility to find a possible value of a gluon field anywhere in the lattice. The gauge invariant objects are either products of gauge links between quark and anti-quark fields, or products of gauge links that form closed paths as shown in the following.

The link variables are oriented, so it is possible to have them pointing towards the negative μ direction (see Fig. 2.5) satisfying the following relation,

$$U(x, x - a\hat{\mu}) \equiv U_{-\mu}(x) = \exp\left(-ig_s a A_\mu\left(x - \frac{\hat{\mu}}{2}\right)\right) = U^\dagger(x - a\hat{\mu}, x) \tag{2.11}$$

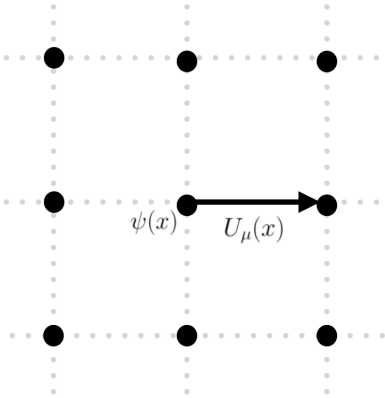

FIGURE 2.4: The sites are occupied by the quark fields, $\psi(x)$, while the links between the lattice sites, $U_\mu(x)$, represent the gauge fields.

FIGURE 2.5: The link variables $U_\mu(x)$ and $U_{-\mu}(x)$ on the lattice.

Gauge Action on the Lattice

Let us turn now to the discretized version of the gauge field action,

$$S_G[A] = -\frac{1}{4}\int d^4x F^a_{\mu\nu}F^a_{\mu\nu} \tag{2.12}$$

Since we are considering the Euclidean space-time there is no need to distinguish covariant and contravariant indices. In the following section, we will construct gauge invariant quantities (observables) on the lattice.

A gauge transformation is done by a rotation of the color space at each site through an $SU(3)$ matrix $G(x)$. In particular, the gauge link U_μ transforms according to

$$U_\mu(x) \to G(x)U_\mu(x)G^\dagger(x + a\hat{\mu}) \tag{2.13}$$

The action (2.12) must be invariant with respect to the transformation law (2.13). To do this, we can use traces of products of U matrices around closed paths, known as Wilson loops. The simplest case is the 1×1 loop (Fig. 2.6), which is the shortest, nontrivial, closed loop on the lattice, the so-called *plaquette*. This gauge invariant quantity is defined by

$$U_{\mu\nu}(x) = \text{Re}\ \left[\text{Tr}\left[\ U_\mu(x)U_\nu(x + a\hat{\mu})U^\dagger_\mu(x + a\hat{\nu})U^\dagger_\nu(x)\right]\right] \tag{2.14}$$

whose invariance follows from (2.13). A Wilson loop is complex in the fundamental representation, with the two possible path-orderings giving complex conjugate values. Taking the trace ensures gauge invariance and the real part is equivalent to averaging the loop and its charge conjugate. We can express directly the *plaquette* in terms of gauge field variables,

$$U_{\mu\nu}(x) = e^{iag_s A_\mu(x+\frac{\hat{\mu}}{2})} e^{iag_s A_\nu(x+\hat{\mu}+\frac{\hat{\nu}}{2})} e^{-iag_s A_\mu(x+\hat{\nu}+\frac{\hat{\mu}}{2})} e^{-iag_s A_\nu(x+\frac{\hat{\nu}}{2})} \tag{2.15}$$

Using the Baker-Campbell-Hausdorff formula for the product of exponentials matrices

$$e^A e^B = e^{A+B+\frac{1}{2}[A,B]+\ldots} \tag{2.16}$$

we have

$$U_{\mu\nu}(x) = e^{ia^2 g_s(\partial_\mu A_\nu(x) - \partial_\nu A_\mu(x) + i[A_\mu(x), A_\nu(x)]) + \mathcal{O}(a^3)} = e^{ia^2 g_s F_{\mu\nu}(x) + \mathcal{O}(a^3)} \tag{2.17}$$

Making an expansion in powers of a in (2.17), we get

$$U_{\mu\nu}(x) = 1 + ia^2 g_s^2 F_{\mu\nu} - \frac{a^4 g_s^2}{2} F_{\mu\nu}^2 + \mathcal{O}(a^6) \tag{2.18}$$

The second (imaginary) term of (2.18) vanishes due to the trace[2] and the real part makes the action real. The gauge action on the lattice can now be written as

$$S_G[U] = \frac{2}{g_s^2} \sum_{x\in\Lambda} \sum_{\mu<\nu} \text{Re Tr}[1 - U_{\mu\nu}(x)] \tag{2.20}$$

The reason for defining the action in terms of small loops is to increase the computation speed and to reduce the size of the discretization errors (see Section 3.8). As an example we can mention that the leading correction to 1×1 loops is proportional to $a^2/6$ whereas for 1×2 loops it increases to $5a^2/12$. Also, the cost of simulation increases by a factor of $2-3$. Inserting (2.18) in the above equation, the following relation appears

$$S_G[U] = \frac{2}{g_s^2} \sum_{x\in\Lambda} \sum_{\mu<\nu} \text{Re Tr}[1 - U_{\mu\nu}] = \frac{a^4}{2g_s^2} \sum_{x\in\Lambda} \sum_{\mu<\nu} \text{Tr}[F_{\mu\nu}(x)^2] + \mathcal{O}(a^2) \tag{2.21}$$

The relation above is also called Wilson gauge action. The factor a^4 and the sum over Λ are the discretization of the space-time integral. The Wilson plaquette action is equivalent to the continuum action, $\lim_{a\to 0} S_G[U] = S_G[A]$, up to discretization errors quadratic in the lattice spacing $\mathcal{O}(a^2)$. The eq. (2.21) can also be written in terms of the parameter $\beta = 2N/g_s^2$, which controls the lattice spacing a and is related to the bare strong coupling.

[2]One may use

$$\text{Tr}\ [U_{\mu\nu}(x)]^* = \ \text{Tr}\ [U_{\mu\nu}(x)^\dagger] = \ \text{Tr}\ [U_{\mu\nu}(x)] \tag{2.19}$$

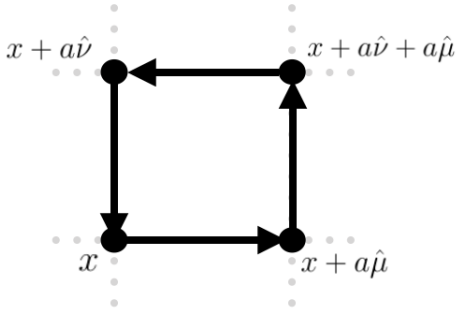

FIGURE 2.6: The plaquette associated to the site x is represented by $U_{\mu\nu}(x)$.

Improvement of the Gauge Action

For any finite lattice spacing, results differ from their continuum limit values, by so-called discretization errors. As we have already shown, the Wilson gauge action (2.21) reproduces the continuum limit up to terms $\mathcal{O}(a^2)$. In order to make the errors smaller, we have to decrease the lattice spacing and increase the number of lattice points, which is numerically expensive. Thus in a numerical simulation one always works with finite a and the discretization errors have to be dealt with, which means they need to be included in the extrapolation to vanishing a. Since it is impossible to choose arbitrarily small lattice spacings, we need to use other strategies in order to minimize discretization effects and try to make the extrapolation to the continuum less dependent on a. One possible way is the Symanzik improvement program [28–30], which improve the convergence properties of the discretized theory. This scheme involves the addition of higher dimensional operators which can be tuned to cancel out the leading order discretization errors:

$$S = \int d^4x \left(\mathcal{L}^{(0)}(x) + a\mathcal{L}^{(1)} + a^2\mathcal{L}^{(2)}(x) + \ldots \right) \tag{2.22}$$

where $\mathcal{L}^{(0)}$ is the QCD Lagrangian, $\mathcal{L}^{(1)}$ is the Lagrangian composed of all dimensional 5 operators, $\mathcal{L}^{(2)}$ is a Lagrangian composed of all dimension-6 operators and so on. The higher dimensional terms do not contribute to the action in the continuum limit ($a \to 0$). However they can reduce lattice artefacts at small a.

For the $SU(N)$ theory, the first terms in the expansion of the *plaquette* in power of the lattice spacing are

$$\text{Re} \ \ [\text{Tr} \ \ (U_{\mu\nu})(x)] = N + \frac{1}{2}a^4 O_4 + a^6 O_6 + \ldots \tag{2.23}$$

where N is the trace of the $1_{N\times N}$ identity matrix. In this case, the dimension-four operator corresponds to the continuum gauge action

$$O_4 = g_s^2 \sum_{\mu\nu} \ \ \text{Tr} \ \ F^a_{\mu\nu} F^{\mu\nu}_a \tag{2.24}$$

The dimension-five operator does not exist, and $O_6 = \sum_j r_j O_6^j$, where O_6^j are the dimension-six

operators allowed by lattice symmetries. The dimension-six operator in the discretized lattice gauge part of the Wilson action leads to discretization errors proportional to a^2. Then, in order to apply this improvement to the gauge part of the Wilson action of QCD, one adds six-link loops involving six gauge links to define $\mathcal{O}(a^2)$ improved actions (see Fig. 2.7),

$$S_G = \frac{2}{g_s^2} \sum_x \left(b_0 \sum_{\mu,\nu}^{4} [1 - \mathrm{Re}(\mathrm{Tr}\, U_{\mu\nu}^{1\times 1}(x))] + b_1 \sum_{\mu,\nu}^{4} [1 - \mathrm{Re}(\mathrm{Tr}\, U_{\mu\nu}^{1\times 2}(x))] \right) \tag{2.25}$$

where $b_0 = 1 - 8b_1$. The gauge part of Wilson action is recovered by doing $b_1 = 0$ and the tree-level Symanzik improved action [31] for $b_1 = -1/12$ [30], which is the form of the gauge action used by the European Twisted Mass Collaboration (ETMC).

Another popular action is the Iwasaki action [32], which considers $b_1 = -0.331$.

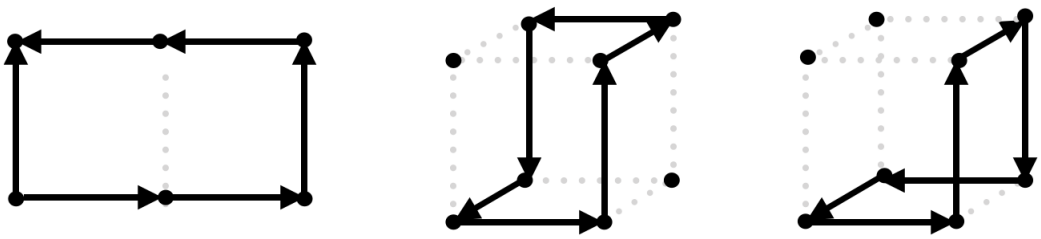

FIGURE 2.7: The only three six-link loops that one can draw on the lattice: from left to right, planar, twisted and L shaped.

2.4.3 Fermion Fields on the Lattice

Working with fermions on the lattice is a very challenging task, and many methods have been suggested over the years. As we proceed to discuss, when the fermions are discretized in a naïve way, some unphysical states appear. In the next sections, several fermionic actions will be presented and their advantages and shortcomings will be identified. Moreover, we will introduce the Wilson-Clover formulation, which is the one used in this work.

Naïve discretization of fermions and the doubler problem

In order to simplify the notations, here we consider the case of a single flavor. The Euclidean action for free Dirac fermions of mass m is given by

$$S_F[\psi, \bar{\psi}] = \int d^4x \bar{\psi}(x) \left[\gamma_\mu \partial_\mu + m \right] \psi(x) \tag{2.26}$$

Going to the lattice, the fields are now defined at the lattice points and the derivative is substituted by its discrete version. We therefore find the so-called *naïve fermion action*[3]

$$\begin{aligned} S_F[\psi,\bar{\psi}] &= a^4 \sum_{a,b,\alpha,\beta} \bar{\psi}_{a,\alpha}(x)(\gamma_\mu)_{\alpha,\beta}\left[\frac{1}{2}(\partial_\mu + \partial_\mu^*) + m\right]\psi_{b,\beta}(x) \\ &= a^4 \sum_{x,y\in\Lambda}\sum_{a,b,\alpha,\beta} \bar{\psi}(x)_{a,\alpha} D(x|y)^{ab}_{\alpha\beta}\psi(y)_{b,\beta} \end{aligned} \tag{2.27}$$

where the discrete forward and backward derivatives are

$$\partial_\mu \psi(x) = \frac{1}{a}\left[\psi(x + a\hat{\mu}) - \psi(x)\right] \tag{2.28}$$

$$\partial_\mu^* \psi(x) = \frac{1}{a}\left[\psi(x) - \psi(x - a\hat{\mu})\right] \tag{2.29}$$

The *naïve Dirac operator* in (2.27) is defined as

$$D(x|y)^{ab}_{\alpha\beta} = \sum_{\mu=1}^{4}(\gamma_\mu)_{\alpha\beta}\frac{1}{2a}\left(\delta_{yx+a\hat{\mu}} - \delta_{yx-a\hat{\mu}}\right) + m\delta_{\alpha\beta}\delta_{ab}\delta_{xy} \tag{2.30}$$

However, by doing this naïve discretization, non-physical degrees of freedom (doublers) appear, even in the continuum limit. For free fermions, the inverse $D(x|y)^{-1}$ of the lattice Dirac operator is the *quark propagator* $G(x|y)^F$ (lattice Green function)

$$\sum_y D(x|y)G(y|z)^F = \delta_{x,z} \tag{2.31}$$

By combining (2.30) and the inverse Fourier transform, we get

$$G(y|z)^F = \frac{1}{\Lambda}\sum_p \tilde{G}^F(p)e^{ip\cdot(y-z)} \tag{2.32}$$

where Λ represents the total number of lattice points[4]. From (2.31) we obtain the Fourier transform of the quark propagator

$$\frac{1}{\Lambda}\sum_p\left(\sum_\mu \gamma_\mu \frac{e^{ip\cdot(x+\hat{\mu}-z)} - e^{ip\cdot(x-\hat{\mu}-z)}}{2a} + me^{ip\cdot(x-z)}\right)\tilde{G}^F(p) = \delta_{x,z} \tag{2.33}$$

$$\Leftrightarrow \frac{1}{\Lambda}\sum_p e^{ip\cdot(x-z)}\left(\sum_\mu \gamma_\mu \frac{e^{iap_\mu} - e^{-iap_\mu}}{2a} + m\cdot\mathbb{1}\right)\tilde{G}^F(p) = \delta_{x,y} \tag{2.34}$$

Using the discretized version of the Dirac function $\delta_{x,z} = \frac{1}{\Lambda}\sum_p e^{ip\cdot(x-z)}$, we arrive at the inverse of the quark propagator in momentum space

$$\tilde{G}^F(p)^{-1} = m\cdot\mathbb{1} + \frac{i}{a}\sum_{\mu=1}^{4}\gamma_\mu \sin(p_\mu a) \tag{2.35}$$

[3] In this equation a and b are the color indices and α and β are the Dirac indices.
[4] $\Lambda \equiv V$: lattice volume.

Finally, we invert the above equation[5],

$$\tilde{G}(p) = \tilde{D}(p)^{-1} = \frac{m \cdot \mathbb{1} - \frac{i}{a}\sum_\mu \gamma_\mu \sin(p_\mu a)}{m^2 + \frac{1}{a^2}\sum_\mu \sin(p_\mu a)^2} \tag{2.37}$$

However, considering a massless fermion ($m = 0$) and taking the continuum limit, the propagator is given by

$$\widetilde{G}(p) = \frac{-\frac{i}{a}\sum_\mu \gamma_\mu \sin(p_\mu a)}{\frac{1}{a^2}\sum_\mu \sin(p_\mu a)^2} \xrightarrow{a\to 0} \frac{-i\sum_\mu \gamma_\mu p_\mu}{p^2} \tag{2.38}$$

which correctly gives a pole at $p = (0,\ 0,\ 0,\ 0)$, as expected in the continuum. However, the lattice expression of the free propagator (2.38) contains also unphysical poles at

$$p = (\pi/a,\ 0,\ 0,\ 0),\ (0,\ \pi/a,\ 0,\ 0),\ \ldots,\ (\pi/a,\ \pi/a,\ \pi/a,\ \pi/a) \tag{2.39}$$

In the end, the naïve Dirac operator $\tilde{D}(p)$ exhibits sixteen poles, fifteen of them being unwanted poles. This is the famous doubler problem. This problem is caused by the choice of discretization and can be seen as a lattice artifact[6]. In the interacting theory the doublers can interact with each other via quantum loop corrections (in particular the gluons couple to each doublers): it is important to remove them properly. In the following, we will understand how to overcome this difficulty.

Discrete Covariant Derivatives

On the lattice, we introduce the discretized version of the covariant derivative, that is

$$\vec{\nabla}_\mu \psi(x) = \frac{U(x, x+a\hat{\mu})\psi(x+a\hat{\mu}) - \psi(x)}{a} \tag{2.40}$$

$$\vec{\nabla}^*_\mu \psi(x) = \frac{\psi(x) - U_{-\mu}(x)\psi(x-\hat{\mu})}{a} \tag{2.41}$$

These derivatives are used to replace the standard derivatives when gluon interactions are introduced. The anti-hermicity of the lattice Dirac operator can be ensured by the symmetric covariant derivative,

$$\nabla\psi(x) = \frac{1}{2}\left(\vec{\nabla}_\mu + \vec{\nabla}^*_\mu\right)\psi(x) = \frac{U(x, x+a\hat{\mu})\psi(x+a\hat{\mu}) - U_{-\mu}(x)\psi(x-a\hat{\mu})}{2a} \tag{2.42}$$

[5] It is easier to write $\tilde{D}(p)^{-1}$ by considering the equation for the inverse of linear combinations of gamma matrices ($a, b_\mu \in \Re$), which is

$$\left(a\cdot\mathbb{1} + i\sum_{\mu=1}^{4}\gamma_\mu b_\mu\right)^{-1} = \frac{a\cdot\mathbb{1} - i\sum_{\mu=1}^4 \gamma_\mu b_\mu}{a^2 + \sum_{\mu=1}^4 b_\mu^2} \tag{2.36}$$

[6] A lattice artefact is a contribution that is present in the lattice, but absent in the continuum.

Wilson Fermions

As we already saw, the lattice action is not unique and it is possible to add irrelevant operators to it, without changing the continuum limit. To overcome the doubler problem Wilson proposed to add an extra momentum-dependent *mass term* to the fermion action [33]. From now on, we are considering the interacting case (interactions with gluons), unless we say the opposite. The new mass term is defined as

$$-\frac{ar}{2}\sum_{\mu}\vec{\nabla}^{*}_{\mu}\vec{\nabla}_{\mu}\psi_{x} \tag{2.43}$$

where r is the so-called Wilson parameter. The Wilson term (2.43), together with the Dirac operator, reads

$$D^{W} = \frac{1}{2}\{\gamma_{\mu}(\vec{\nabla}_{\mu} + \vec{\nabla}^{*}_{\mu}) - a\frac{r}{2}\vec{\nabla}^{*}_{\mu}\vec{\nabla}_{\mu}\} + m \tag{2.44}$$

and the Wilson's fermion action is defined by

$$\begin{aligned} S^{W}[U_{\mu},\psi,\bar{\psi}] &= m\sum_{x,y}\bar{\psi}_{x,\alpha,a}\psi_{y,\beta,b}\delta_{xy}\delta_{\alpha\beta}\delta_{ab} \\ &+ \frac{1}{2a}\sum_{x,\mu}\bar{\psi}_{x,\alpha,a}(\gamma_{\mu})_{\alpha\beta}[U_{\mu}(x)_{ab}\psi_{x+\hat{\mu},\beta,b} - U^{\dagger}_{\mu}(x-\hat{\mu})_{ab}\psi_{x-\hat{\mu},\beta,b}] \\ &- \frac{ra}{2a^{2}}\sum_{x,\mu}\bar{\psi}_{x,\alpha,a}[U_{\mu}(x)_{ab}\psi_{x+\hat{\mu},\beta,b}\delta_{\alpha\beta} - 2\psi_{x,\beta,\beta}\delta_{ab}\delta_{\alpha\beta} \\ &+ U^{\dagger}_{\mu}(x-\hat{\mu})_{ab}\psi_{x-\hat{\mu},\beta,b}] \end{aligned} \tag{2.45}$$

which can also be put in a compact form

$$S^{W}[U_{\mu},\psi,\bar{\psi}] \equiv a^{4}\sum_{x,y}\sum_{\alpha,\beta,a,b}\bar{\psi}_{x,\alpha,a}D^{W}(x,y)^{ab}_{\alpha,a}\psi_{y,\beta,b} \tag{2.46}$$

The Wilson term gives no contributions for $a \to 0$. To work with lattice simulations, it is useful to make a rescaling of the fermionic field in order to introduce the so-called hopping parameter κ which is a simple rescaling factor that is related to the quark mass and acts as a coupling between neighboring sites [34],

$$\psi(x) \to \sqrt{\frac{2\kappa}{a^{3}}}\psi(x) \tag{2.47}$$

$$\kappa^{-1} = 2ma + 8r \tag{2.48}$$

Using the hopping parameter, the Wilson Dirac operator has the form

$$\begin{aligned} D^{W}(x,y)^{ab}_{\alpha\beta} &= \frac{1}{2a}\Bigg(\kappa^{-1}\delta_{xy}\delta_{\alpha\beta}\delta_{ab} - \sum_{\mu}\big[(1-\gamma_{\mu})_{\alpha\beta}\delta_{x,y-\hat{\mu}}U_{\mu}(x)_{ab} \\ &+ (1+\gamma_{\mu})_{\alpha\beta}\delta_{x,y+\hat{\mu}}U^{\dagger}_{\mu}(x-\hat{\mu}_{ab})\big]\Bigg) \end{aligned} \tag{2.49}$$

Following the same idea as in the previous section (2.4.3) the Fourier transformed Dirac operator reads

$$\widetilde{D}(p) = m\mathbb{1} + \frac{i}{a}\sum_{\mu=1}^{4}\gamma_\mu \sin(p_\mu a) + \mathbb{1}\frac{1}{a}\sum_{\mu=1}^{4}(1-\cos(p_\mu a)) \tag{2.50}$$

As already noted, the Wilson term keeps the pole $p_\mu = 0$. However, for the components for which $p_\mu = \pi/a$, an extra contribution of $2/a$ emerges, which behaves as an additional mass term. In fact, the mass of these extra poles is given by

$$m + \frac{2l}{a} \tag{2.51}$$

where l is the number of momentum components with $p = \pi/a$. In the continuum, when $a \to 0$, the doublers become infinitely heavy and decouple from the theory: at the end, only the physical pole remains. A drawback is that the Wilson term breaks explicitly chiral symmetry, as discussed in the following sections.

Wilson-Clover Fermion

The improvement of the fermion action is achieved in a similar way to the one used for the Symanzik improvement scheme (see Section 2.4.2), however we are able to form operators using both fermion fields and link variables. The Wilson action for quarks (2.46), which contains the Wilson term introduced to eliminate the doublers, has discretization errors of order $\mathcal{O}(a)$. Since we will use Monte Carlo algorithms to evaluate the path integral in lattice simulations, we need to find ways to reduce the discretization errors. The lattice discretization is not unique and one can construct improved actions in order to converge to the continuum limit faster. According to Sheikholeslami and Wohlert [35] a possible alternative to improve the fermion action (by canceling $\mathcal{O}(a)$ effects) can be derived by adding the so-called *clover* term

$$S^W_{\text{improv.}} = S^W[U_\mu, \psi, \bar{\psi}] + c_{SW}\frac{ia^5}{4}\sum_{x\in\Lambda}\bar{\psi}(x)\sigma_{\mu\nu}F_{\mu\nu}\psi(x) \tag{2.52}$$

where $\sigma_{\mu\nu} \equiv [\gamma_\mu, \gamma_\nu]/2i$ is the Pauli matrix written in terms of the gamma matrices [26]. The coefficient c_{SW} can be calculated non-perturbatively and $F_{\mu\nu}$ is the discretized version of the gluon field strength. The $F_{\mu\nu}$ normalization differs from the one in the continuum (2.3) by a factor ig_s. A convenient regularization is obtained by averaging the four plaquettes lying in the (μ, ν) plane around the point x (see Fig. 2.8)

$$F_{\mu\nu}(x) = \frac{-i}{8a^2}[Q_{\mu\nu}(x) - Q_{\nu\mu}(x)] \tag{2.53}$$

with (see [35])

$$\begin{aligned} Q_{\mu\nu} &= (U_\mu(x)U_\nu(x+a\hat{\mu})U_{-\mu}(x+a\hat{\mu}+a\hat{\nu})U_{-\nu}(x+a\hat{\nu}) \\ &+ U_\mu(x)U_{-\nu}(x+a\hat{\mu})U_{-\mu}(x+a\hat{\mu}-a\hat{\nu})U_\nu(x-a\hat{\nu}) \\ &+ U_{-\mu}(x)U_{-\nu}(x-a\hat{\mu})U_\mu(x-a\hat{\mu}-a\hat{\nu})U_\nu(x-a\hat{\nu}) \\ &+ U_{-\mu}(x)U_\nu(x-a\hat{\mu})U_\mu(x-a\hat{\mu}+a\hat{\nu})U_{-\nu}(x+a\hat{\nu})) \\ &= U_{\mu,\nu}(x) + U_{\nu,-\mu}(x) + U_{-\mu,-\nu}(x) + U_{-\nu,\mu}(x) \end{aligned} \tag{2.54}$$

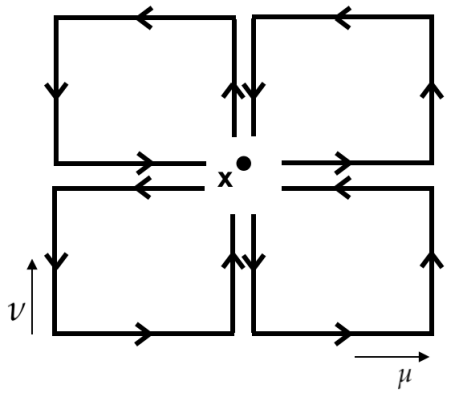

FIGURE 2.8: Schematic representation of the sum $Q_{\mu\nu}$(x) of plaquettes in the (μ,ν) plane used for the discretized field strength operator $F_{\mu\nu}$.

Due to the shape of the above terms which is reminiscent of a clover leaf, the last term in (2.52) is called *clover term* or *clover improvement* [26].

The $\mathcal{O}(a)$ improvement, at tree level, is achieved with $c_{SW} = 1$. However, in the interacting theory, c_{SW} depends on the bare coupling g_s, but does not depend on the quark mass. As we mentioned before, c_{SW} can be computed through perturbation theory [35, 36] and for $N_f = 2$ dynamical quarks (which will be explained later) we have [37]

$$c_{SW} = \frac{1 - 0.454g_s^2 - 0.175g_s^4 + 0.012g_s^6 + 0.045g_s^8}{1 - 0.720g_s^2} \tag{2.55}$$

It is also possible to compute non-perturbatively c_{SW} by imposing suitable improvement conditions [37]. For a discussion on this topic see, for example Ref. [38].

As we mentioned before, this action is the one we will use for the simulations in our study.

Chiral Symmetry Comments

The chiral symmetry is a symmetry of the Lagrangian for massless fermions. The corresponding Lagrangian, in Euclidean space, is

$$\mathcal{L} = \sum_f \bar{\psi}_f \gamma_\mu D_\mu \psi_f \equiv \sum_f \bar{\psi}_f D \psi_f \tag{2.56}$$

which defines the massless Dirac operator D and $\psi_f \equiv \psi$ is a fermion field. The spinor field can be decomposed into chiral fields ψ_L and ψ_R

$$\psi = \psi_L + \psi_R = \frac{1}{2}(1-\gamma_5)\psi + \frac{1}{2}(1+\gamma_5)\psi = P_L\psi + P_R\psi \tag{2.57}$$

where P_L and P_R are, respectively, the left-handed and right-handed projectors with

$$P_L^2 + P_R^2 = 1 \;\; ; \;\; P_L P_R = 0 \;\; ; \;\; P_L^2 = P_L \;\; ; \;\; P_R^2 = P_R \tag{2.58}$$

The Lagrangian can be rewritten as

$$\mathcal{L} = \bar{\psi}_L D\psi_L + \bar{\psi}_R D\psi_R \tag{2.59}$$

Since the chiral symmetry holds only for massless quarks, the limit of vanishing quark mass is often referred to as the *chiral limit*. By writing together eqs. (2.56) and (2.59)

$$\mathcal{L} = \bar{\psi}D\psi = \bar{\psi}_L D\psi_L + \bar{\psi}_R D\psi_R \tag{2.60}$$

and substituing the relations given in eq. (2.57) we obtain

$$D\gamma_5 + \gamma_5 D = 0 \tag{2.61}$$

which is considered the essence of the chiral symmetry in the continuum: the massless Euclidean Dirac operator $D = \gamma_\mu(\partial_\mu + ig_s A_\mu)$ anticommutes with γ_5.

Chiral Symmetry and the Lattice

The lattice results need to respect the continuum limit of the massless fermions, so the chiral symmetry has to be respected for $a \neq 0$. Although the Wilson term is very helpful to remove the doublers, the Wilson Dirac operator D^W does not respect the relation (2.61). In other words, the Wilson operator breaks the chiral symmetry, and introduces $\mathcal{O}(a)$ artifacts that were not present in the naïve quark action. The chiral symmetry is only recovered in the continuum limit, when $a \to 0$. As a consequence of the chiral symmetry breaking, there is an additive mass renormalization term in the action (2.45) which diverges in the continuum limit. The critical value of the hopping parameter (κ_{crit}) is defined as the value of κ at which the pion mass vanishes:

$$m = \frac{1}{2a}\left(\frac{1}{\kappa} - \frac{1}{\kappa_{\text{crit}}}\right) \tag{2.62}$$

In the free theory $\kappa_{\text{crit}} = 1/8$, but when interactions are turned on, its value gets renormalized and has to be computed numerically [34].

Nielsen and Ninomiya [39, 40] have analyzed in detail the implementation of the chiral symmetry on the lattice. Their results, known as the Nielsen-Ninomiya no-go theorem, can be summarized as follows: it is impossible to have a chirally invariant, doubler-free, local and

translation invariant fermion action on the lattice. Then, at first sight, it seems impossible to have a chirally invariant action without doublers. However, there exists a clever way to circumvent this problem: the *Ginsparg-Wilson relation* [41, 42]

$$D\gamma_5 + \gamma_5 D = aD\gamma_5 D \tag{2.63}$$

The right-hand side vanishes for $a \to 0$ and the chiral symmetry is recovered in the continuum limit. The above equation also allows to define the chiral symmetry on the lattice for a finite a. Currently, in numerical simulations, two types of Ginsparg-Wilson fermions are being used: *domain-wall fermions* (DWF) and *overlap fermions*. The first, is defined in a fifth dimension, while the second have an explicit form that exactly satisfies the Ginsparg-Wilson relation. Both methods have a computational cost which is at least an order of magnitude greater than for other choices.

The Wilson Clover Dirac operator, which is used in this work, obeys the so-called γ_5-hermicity relation[7]

$$\gamma_5 D^W \gamma_5 = D^{\dagger W} \tag{2.64}$$

and will be used to compute the objects known as correlation functions on the lattice. The spectrum of the operator $\gamma_5 D^W$ can have real or complex conjugated pairs of eigenvalues. In particular, the determinant of the Dirac operator is real.

Twisted-mass fermions

Another choice of lattice regularization for the spinor field, which does not suffer from unphysical fermion zero modes (the doublers) is the twisted mass fermion action (tmQCD) [43–45]. For two mass-degenerate quarks[8], the fermionic twisted mass QCD action is given by:

$$\begin{aligned} S_F^{tm}[\psi, \bar{\psi}, U] &= \int d^4x \bar{\psi}_{a,\alpha,f_{(1)}}(x) \Big[(\gamma_\mu)_{\alpha\beta} (D_\mu)_{ab} \delta_{f_{(1)}f_{(2)}} + m\delta_{ab}\delta_{\alpha\beta}\delta_{f_{(1)}f_{(2)}} \\ &+ i\mu(\gamma_5)_{\alpha\beta}(\tau^3)_{f_{(1)}f_{(2)}}\delta_{ab} \Big] \psi_{b,\beta,f_{(2)}}(x) \end{aligned} \tag{2.65}$$

where D_μ is the covariant derivative, m the bare mass and τ^3 is the third Pauli matrix acting on the $SU(2)$ flavor space. The real parameter μ is called the twisted mass and the term $i\mu\gamma_5\tau^3$ has a non trivial structure in both Dirac space (due to the presence of γ_5) and in flavour space (due to the Pauli matrix τ^3). The mass term of tmQCD in (2.65) can be written as

$$m + i\mu\gamma_5\tau^3 = Me^{i\omega\gamma_5\tau^3} \tag{2.66}$$

[7] The γ_5-hermiticity is a symmetry of lattice Dirac operators. Almost all Dirac operators D are γ_5-hermitian, i.e., they obey

$$(\gamma_5 D)^\dagger = \gamma_5 D \quad \text{or, equivalently,} \quad D^\dagger = \gamma_5 D \gamma_5$$

[8] Represented in eq. (2.65) by the flavor indices: $f_{(1)}$ and $f_{(2)}$.

where M is the polar (or invariant) mass and w is the twist angle,

$$M = \sqrt{m^2 + \mu^2} \tag{2.67}$$

$$\tan(w) = \frac{\mu}{m} \tag{2.68}$$

From here on, the indices will be suppressed to simplify the notation. Using (2.66), eq. (2.65) becomes

$$S_F^{tm}[\psi, \bar{\psi}, U] = \int d^4x \bar{\psi}(x)[\gamma_\mu D_\mu + Me^{iw\gamma_5\tau^3}]\psi(x) \tag{2.69}$$

Here, we can observe an additional twist mass term that does not exist in the standard action of QCD. Performing an axial transformation on both quark and antiquark fields

$$\begin{aligned} \psi &\to \psi' = e^{i\frac{\alpha}{2}\gamma_5\tau^3}\psi \\ \bar{\psi} &\to \bar{\psi}' = \bar{\psi}e^{i\frac{\alpha}{2}\gamma_5\tau^3} \end{aligned} \tag{2.70}$$

one recovers the standard QCD action, where α is the chiral rotation angle. In doing so, we also redefine the mass parameters through the following transformations

$$\begin{aligned} m &\to m' = m\cos(\alpha) + \mu\sin(\alpha) \\ \mu &\to \mu' = \mu\cos(\alpha) - m\sin(\alpha) \end{aligned} \tag{2.71}$$

Under these transformations the new twisted-mass expression can be written as

$$S_F'^{tm}[\psi, \bar{\psi}, U] = \int d^4x \bar{\psi}'(x)[\gamma_\mu D_\mu + Me^{iw'\tau^3\gamma_5}]\psi'(x) \quad \text{and} \quad M' = M \tag{2.72}$$

The invariant mass is indeed invariant under the transformations (2.71) and the new twist angle is $\tan(w') = \frac{\mu'}{m'}$ with $\tan(w') = \tan(w - \alpha)$. This confirms that the theory is invariant under the chiral rotations (2.70). The transformations (2.71) and (2.70) change the field variables and the mass definitions, but do not change the theory. As a conclusion, one can say that tmQCD is a family of equivalent theories parametrized by the invariant mass M and the twist angle w.

Lattice tmQCD

We now replace the continuum Euclidean space-time by a hypercubic lattice of spacing a. Then, the tmQCD action on the lattice with Wilson fermions is

$$S_F^W[\psi, \bar{\psi}, U] = a^4 \sum_x \bar{\psi}(x) \left[\frac{1}{2}\sum_\mu \left(\gamma_\mu(\nabla_\mu^* + \nabla_\mu) - a\frac{r}{2}\nabla_\mu^*\nabla_\mu\right) + m + i\mu\tau^3\gamma_5\right]\psi(x) \tag{2.73}$$

Recalling the Wilson Dirac operator given in (2.44), eq. (2.73) can be written as

$$S_F^W[\psi, \bar{\psi}, U] = a^4 \sum_x \bar{\psi}(x) \left[D^W + m + i\mu\tau^3\gamma_5\right]\psi(x) \tag{2.74}$$

The tmLQCD action is constructed with Wilson fermions and has an extra twisted mass term. The Wilson term (mandatory to remove the doublers) breaks the axial symmetry and the twist mass term is not removed by the transformation described in eq. (2.70). The equivalence between QCD and twisted mass QCD is only valid in the continuum and the two lattice discretizations are different.

Maximal Twist

We have two bare parameters m and μ, which define the physics we want to describe. These two parameters are related by the twist angle w. The twist angle can be defined in the renormalized theory by

$$\tan w = \frac{\mu_R}{m_R} = \frac{Z_\mu \mu_q}{Z_m \underbrace{[m_0 - m_{cr}]}_{m_q}} \tag{2.75}$$

where Z_μ is the renormalization constant of the twisted quark mass μ_q and Z_m is the renormalization constant of the untwisted quark mass m_0. In addition, m_R and μ_R are the renormalized parameters. When $w = \pi/2$ (the so-called *maximal twist*), [46] we have $m_0 = m_{cr}$. For maximal twist, the discretization effects of $\mathcal{O}(a)$ vanish and the leading corrections appear only at $\mathcal{O}(a^2)$. This property is known as the $\mathcal{O}(a)$ *improvement*.

Moreover, since the chiral symmetry at finite lattice spacing is not present, the bare untwisted mass term renormalizes with a counter term called the critical mass m_{cr} [46]. This term corresponds to the value of m_0 at the point where the untwisted quark mass m_R vanishes. In order to tune the value of w, one has to determine the ratio between Z_μ and Z_m and the critical mass m_{cr}.

Advantages and Disadvantages of tmQCD

For the tmQCD action, choosing maximal twist ($w = \pi/2$) simplifies, in most situations, the renormalization of the weak interaction matrix elements [47]. Weak interactions account for large variety of physical processes such as muon and tau decays, neutrino interactions and decays of lightest mesons. This is important, not only in terms of computational difficulty, but also in terms of the uncertainty entering the computation of the observables on the lattice, as for example the decay constants. The error associated with the computation of the renormalization constants does enter the systematics. Moreover, choosing the maximal twist implies an important property called $\mathcal{O}(a)$ improvement, i.e. the discretization effects of $\mathcal{O}(a)$ vanish and the leading corrections appear only at $\mathcal{O}(a^2)$. The advantages of using the tmQCD regularization are described in great detail in Ref. [45]. On the other hand, twisted terms break explicitly the parity and isospin at finite lattice spacing. However, these terms are $\mathcal{O}(a^2)$ and they disappear in the continuum limit: those symmetries are restored in the continuum.

2.5 Summary

In this chapter we have discussed the discretization of gauge and fermion fields as well as the issues related to the discretizations. In our study, we will use the Wilson-Clover action and in the next chapter we will focus on the lattice computation and some of our results.

Chapter 3

Computation of Observables in Lattice QCD

Lattice QCD requires highly intensive numerical simulations on high performance computing facilities. Since we have a computational limit, statistical and systematic errors associated with the calculation must be taken into consideration: precision phenomenology requires these errors to be under control.

In this chapter, we will focus on the computation of observables in lattice QCD by using the formalism of path integrals. We will discuss the procedure to calculate correlation functions, extract the physical observables in Lattice QCD and extrapolate them to the *real world* (continuum limit).

In addition, we will describe some techniques to compute propagators, as well as the Gaussian smearing and APE smearing methods which improve the overlap of the lattice hadron interpolators with the physical state.

3.1 Path Integrals in Lattice QCD

In order to compute an observable in LQCD, we are interested in calculating the vacuum expectation value of some operator given in path integral form as,

$$\langle O \rangle = \frac{1}{\mathcal{Z}} \int \mathscr{D}[\psi]\mathscr{D}[\bar{\psi}]\mathscr{D}[U_\mu]\mathcal{O}[U_\mu,\psi,\bar{\psi}]e^{-(S_G+S_F)} \tag{3.1}$$

where $\mathcal{Z}$ is the Euclidean partition function of QCD,

$$\mathcal{Z} = \int \mathscr{D}[\psi]\mathscr{D}[\bar{\psi}]\mathscr{D}[U_\mu]e^{-(S_G+S_F)} \tag{3.2}$$

The gluonic and fermionic part of the QCD action are, respectively, $S_G = S_G[U_\mu]$ and $S_F = S_F[U_\mu,\psi,\bar{\psi}]$, and were both described in the preceding chapter. In eq. (3.1) the path integral runs over all values of the quark (ψ) and gluon (U) fields at every point in space-time. The quantity $\mathscr{D}[\psi]\mathscr{D}[\bar{\psi}]\mathscr{D}[U_\mu]$ is the integration measure of the fermion and gauge link variables. In this formalism, the quantization of the system is implemented as an integral over all field configurations.

On the lattice, the continuous integral is replaced by a discrete sum over all degrees of freedom. Since the volume and the spacing of the lattice are both finite, eq. (3.1) is well

defined and the measure in the path integral reads

$$\mathscr{D}[\psi,\bar{\psi}] = \sum_{x\in\Lambda}\sum_{\alpha,a} d\psi_{f,\alpha,a}(x)d\bar{\psi}_{f,\alpha,a}(x) \tag{3.3}$$

$$\mathscr{D}[U_\mu] = \sum_{x\in\Lambda}\sum_{\mu=1}^{4} dU_\mu(x) \tag{3.4}$$

where α and a are the Dirac and color indices, respectively. The Haar measure[1] on the compact $SU(3)$ group is represented by $dU_\mu(x)$.

There are two complex Grassmann vectors, $\psi(x)$ and $\bar{\psi}(x)$ associated to each site of the lattice. In general, it is difficult to compute Grassmann numbers appearing in the calculation of the integral in eq. (3.1) due to degrees of freedom in the lattice (as will be explained below). In order to circumvent this problem, we need to rewrite the equations in a different way. We thus start by rewriting the fermion action as

$$S_F = \sum_{x\in\Lambda} \bar{\psi}_f(x) D \psi_f(x) \tag{3.5}$$

From now on, color and Dirac indices are omitted for simplicity. Since the fermion fields are Grassmann numbers, it is possible to use the corresponding Gaussian integral formula to get

$$\int \mathscr{D}[\psi]\mathscr{D}[\bar{\psi}] e^{-S_F[U_\mu,\psi,\bar{\psi}]} = \det[D[U_\mu]] \tag{3.6}$$

Then, the average value of a fermionic variable can be written as

$$\langle\Omega|\psi(x_1)\dots\psi(x_n)\bar{\psi}(y_1)\dots\bar{\psi}(y_m)|\Omega\rangle = \frac{\int \mathscr{D}[U_\mu]\mathscr{D}[\psi]\mathscr{D}[\bar{\psi}]\psi(x_1)\dots\psi(x_n)\bar{\psi}(y_1)\dots\bar{\psi}(y_m)e^{-S_F[U_\mu,\psi,\bar{\psi}]-S_G[U_\mu]}}{\int \mathscr{D}[U_\mu]\mathscr{D}[\psi]\mathscr{D}[\bar{\psi}]e^{-S_F[U_\mu,\psi,\bar{\psi}]-S_G[U_\mu]}} \tag{3.7}$$

where $|\Omega\rangle \equiv$ vacuum. Using the preceding results we can rewrite the latter expression as

$$\langle\Omega|\psi(x_1)\dots\psi(x_n)\bar{\psi}(y_1)\dots\bar{\psi}(y_m)|\Omega\rangle = \frac{\int \mathscr{D}[U_\mu]\,\langle\Omega|\psi(x_1)\dots\psi(x_n)\bar{\psi}(y_1)\dots\bar{\psi}(y_m)|\Omega\rangle_F \det[D[U_\mu]]e^{-S_G[U_\mu]}}{\int \mathscr{D}[U_\mu]\det[D[U_\mu]]e^{-S_G[U_\mu]}} \tag{3.8}$$

in which

$$\langle\Omega|\psi(x_1)\dots\psi(x_n)\bar{\psi}(y_1)\dots\bar{\psi}(y_m)|\Omega\rangle_F = \frac{\int \mathscr{D}[\psi]\mathscr{D}[\bar{\psi}]\psi(x_1)\dots\psi(x_n)\bar{\psi}(y_1)\dots\bar{\psi}(y_m)e^{-S_F[U_\mu,\psi,\bar{\psi}]}}{\int \mathscr{D}[\psi]\mathscr{D}[\bar{\psi}]e^{-S_F[U_\mu,\psi,\bar{\psi}]}} \tag{3.9}$$

[1] In mathematical analysis, the Haar measure is a way of assigning an invariant volume to subsets of locally compact groups and then defining an integral for functions on those groups [26].

is the fermionic path integration (depends on the U_μ) which can be analytically computed because of the structure of $S_F[U_\mu, \psi, \bar{\psi}]$ (Gaussian integral). Moreover, we know that $\langle \psi(x)\bar{\psi}(y)\rangle_F$ is the fermionic propagator from the point y (known as source) to the point x (known as sink) for a particular gauge configuration $[U_\mu]$. Hence, using Wick's theorem, the average value of any fermionic observable will be written using the average value of fermionic propagators over a set of gauge configurations.

Degrees of Freedom

On the lattice grid there is a large number of degrees of freedom, which makes it impossible to evaluate in a simple way integrals like the ones in eq. (3.1). As an example, let us calculate the total number of integrals for a lattice size, for example $L^3 \times T = 24^3 \times 48$:

- $\psi(x)$: 24 degrees of freedom for every flavor (2 particles/antiparticles, 3 colors, 4 spins)
- U_μ: 32 gluon degrees of freedom (8 colors, 4 spins)

For the lattice size we have choosen, and multiplying the numbers above, we get

$$24^3 \times 48 \times (24 + 32) \approx 37 \times 10^6 \text{ integrals.} \tag{3.10}$$

Since the number of integration variables is huge, complete numerical integration is impractical. One possible way is to use Monte Carlo techniques.

3.2 Monte Carlo Techniques

3.2.1 Importance Sampling

We would like to evaluate the expectation value in eq. (3.1) and it can be done through Monte Carlo simulations. The idea in a Monte Carlo is the following: let us assume that we want to compute some vacuum expectation value $\langle O\rangle$; to do so, we need to generate a set of gauge field configurations $\{U_\mu\}$ distributed with the (Boltzmann) probability $e^{-S[U_\mu]}$, and then average over these configurations:

$$\langle O\rangle = \frac{\int \mathscr{D}[U_\mu]\mathcal{O}[U_\mu]e^{-S[U_\mu]}}{\int \mathscr{D}[U_\mu]e^{-S[U_\mu]}} = \frac{1}{N_c}\sum_{i=1}^{N_c}\mathcal{O}[U_\mu^{(i)}] + O_{\text{err}}\left(\frac{1}{\sqrt{N_c}}\right) \tag{3.11}$$

where N_c is the number of configurations in the set. Under the assumptions of the central limit theorem[2], for a sufficiently large N_c we estimate the error on $\langle O\rangle$ to be about $1/\sqrt{N_c}$. An accurate estimate of the error is done by using *Jackknife* techniques, that we will explain later.

Moreover, here

$$S[U_\mu] = S_G[U_\mu] + \ln\left(\det[U_\mu]\right) \tag{3.12}$$

[2]The central limit theorem (CLT) establishes the normal distribution as the distribution to which the mean (average) of almost any set of independent and randomly generated variables rapidly converges.

Physically, the logarithmic term corresponds to the contributions of the quarks in the sea and is numerically very demanding. If we neglect this contribution we are performing a *quenched* simulation, whereas the simulation is said *unquenched* when taking the sea quarks into account. This will be further discussed in Section 3.5.1.

3.2.2 The Hybrid Monte Carlo Algorithm

The Hybrid Monte Carlo (HMC) was introduced as a fast method for simulating molecular dynamics [48]. It has been proposed as a method to improve the Markov Chain Monte Carlo (MCMC) algorithms [49]. In our studies, we would like to perform global transformations of the gauge field, because the local transformations require the full determinant (which is a non-local quantity). Moreover, since the Markov Process generates the new gauge configuration from the previous one, it introduces autocorrelation effects which need to be reduced. However, after a global transformation, the corresponding value of the action can substantially change and the new gauge configuration is unlikely to contribute significantly to the action. Therefore, very small steps are required in the updated algorithm, which generates high autocorrelation effects. One of the advantages of the HMC algorithm [48] is to solve these problems. In this work we have used two different algorithms which implement the HMC. Both cases will be discussed later. For more details about HMC see, for example Ref. [50].

3.3 Correlation Functions at the Hadronic Level

Hadron masses can be computed in LQCD simulations using two-point correlation functions, where a particle of interest is created at some initial time and destroyed at a later time, on a four dimensional Euclidean lattice space-time.

In general a two-point correlation function is defined by

$$C(t_y - t_x) = \langle \Omega | \mathcal{O}(t_y) \mathcal{O}^\dagger(t_x) | \Omega \rangle \tag{3.13}$$

where the creation operator $\mathcal{O}$ has the structure

$$\mathcal{O}(t_x) = \sum_{\vec{x}} \bar{\psi}_f(\vec{x}, t_x) \Gamma \psi_f(\vec{x}, t_x) \tag{3.14}$$

and Γ can contain a combination of Dirac matrices and even non-local operators such as derivatives. In eq. (3.13) the operator $\mathcal{O}^\dagger(t_x)$ creates a hadron state with a vanishing momentum and the correct quantum numbers (see Table 3.1), while $\mathcal{O}(t_y)$ annihilates a state with the same properties. A more complete discussion of the topic will be conducted in the next chapter and in the Appendix A.

On the lattice, the two-point correlation functions can be expressed as traces over products of quark propagators, Dirac matrices and color structures (details in Appendix A) as

$$C(t \equiv t_y - t_x) = -\sum_{\vec{x},\vec{y}} \langle \mathrm{Tr} \left[G(\vec{x}, t_x; \vec{y}, t_y) \Gamma G(\vec{y}, t_y; \vec{x}, t_x) \bar{\Gamma} \right] \rangle \tag{3.15}$$

	J^{PC}	Γ
Scalar	0^{++}	1
	0^{+-}	γ_0
Pseudoscalar	0^{-+}	γ_5
		$\gamma_0\gamma_5$
Vector	1^{--}	γ_i
		$\gamma_0\gamma_i$
Axial	1^{++}	$\gamma_5\gamma_i$
Tensor	1^{+-}	$\gamma_i\gamma_j$

TABLE 3.1: Quantum numbers associated with some local interpolating operators, which have the form $\mathcal{O} = \bar{\psi}(x)\Gamma\psi(x)$.

where $G(x, t_x; y, t_y)$ propagates a fermion from $(\vec{y}, t_y)$ to the lattice site $(\vec{x}, t_x)$ and $G(y, t_y; x, t_x)$ propagates another fermion in the opposite direction (as in Fig. 3.1). During our studies, we always considered two degenerate dynamical quarks, therefore the propagator $G(x, t_x; y, t_y)$ and $G(y, t_y; x, t_x)$ are numerically the same (but formally, they are different). Usually, we can use γ_5-hermiticity to express the forward Dirac propagators $G(x; y)$ in terms of the backward Dirac propagator $G(y; x)$

$$G(x; y) = \gamma_5 G(y; x)^\dagger \gamma_5 \tag{3.16}$$

and (3.15) becomes

$$C(t) = -\sum_{\vec{x},\vec{y}} \langle \mathrm{Tr}\left[G^\dagger(\vec{y}, t_y; \vec{x}, t_x)\Gamma\gamma_5 G(\vec{y}, t_y; \vec{x}, t_x)\gamma_5\bar{\Gamma}\right]\rangle \tag{3.17}$$

The γ_5-hermiticity is very useful in this case, because the number of propagators to be computed is reduced and only one inversion of the Dirac operator is needed.

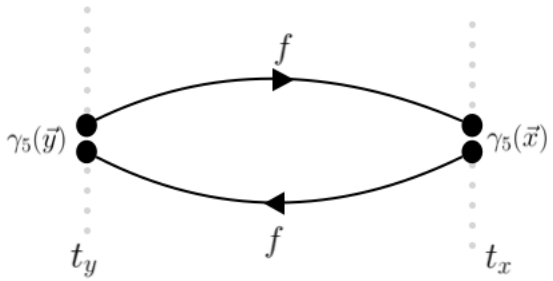

FIGURE 3.1: Schematical representation of a two-point correlation function.

3.4 Extraction of an Effective Mass

In the rest-frame, the two point correlation functions are defined as (see Appendix A for details)

$$C(t) = \sum_n \frac{1}{2m_n} |\langle \Omega|\mathcal{O}|n\rangle|^2 e^{-m_n t} = \sum_n e^{-m_n t}\mathcal{Z}_n \tag{3.18}$$

where m_n is the mass of the n$^{\text{th}}$ eigenstate of the Hamiltonian. The matrix elements are denoted

$$\mathcal{Z}_n \equiv \frac{|\langle \Omega|\mathcal{O}|n\rangle|^2}{2m_n} \tag{3.19}$$

where $\mathcal{Z}_n$ corresponds to the strength of the overlap between the interpolating field $\mathcal{O}$ and the n^{th} state. In the large Euclidean time limit, all contributions will be suppressed relative to the ground state. Being a sum of exponentials, eq. (3.18) can be put into the form

$$C(t) \approx \mathcal{Z}_0 e^{-m_0 t}\left(1 + \frac{\mathcal{Z}_1}{\mathcal{Z}_0} e^{-(m_1 - m_0)t} + \dots\right) \tag{3.20}$$

where m_0 is the ground state mass and m_1 the mass of the first excited state, and so on. For small times, all terms will contribute to the calculation, but for large times (t larger than the inverse of the first energy gap ($\delta m_1 = m_1 - m_0$) the terms inside the brackets become negligible, hence

$$C(t) \approx \mathcal{Z}_0 e^{-m_0 t} \tag{3.21}$$

For correlators which are symmetric with respect to the exchange $t \leftrightarrow T - t$, the time dependence should be

$$C(t) = \mathcal{Z}_0 \cosh\left[m_0\left(\frac{T}{2} - t\right)\right] e^{-T\frac{m_0}{2}} \tag{3.22}$$

where T is the lattice time dimension. Then, the effective mass can be extracted from

$$m_{eff} = \ln \frac{C(t)}{C(t+1)} \tag{3.23}$$

Using the relation (3.23) we can extract the ground state mass. We can also extract the excited state masses from a multiple exponential fit. However, in practice this is a numerically non-trivial task, because of the noise in the data from the calculation. We can point out that a significant factor complicating these calculations is the signal-to-noise problem [51, 52]. The signal-to-noise ratio degrading $\sim \exp^{(m_M - m_\pi)t}$ [27], we can observe that the signal-to-noise ratio will get worse as the mass of the hadron increases. In order to extract masses and other observables of excited states, we will present another method in the next chapter. Figure 3.2

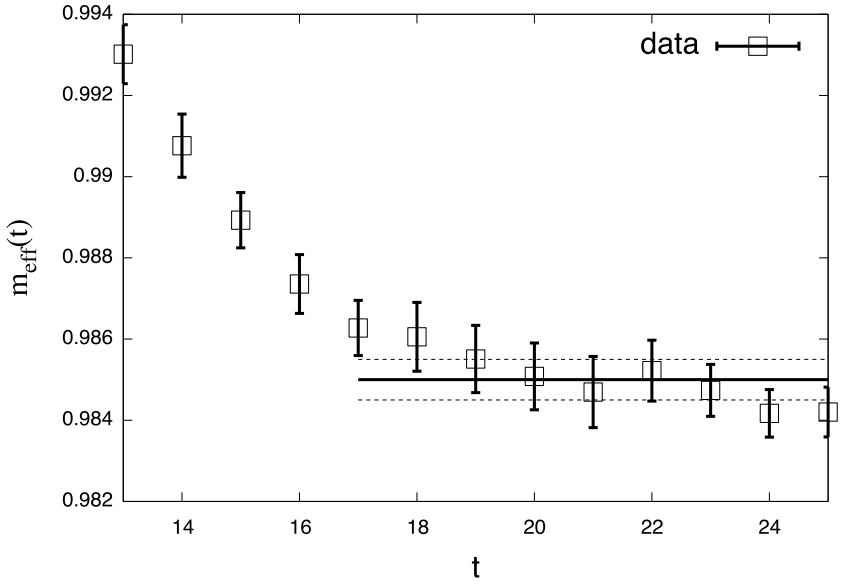

FIGURE 3.2: Results of the fit for the effective mass (ground state) from the computation of the two-point correlation functions.

displays a plot of the effective mass for the ground state as a function of time for the charmonium pseudoscalar state η_c. In this simulation, the fermions are $\mathcal{O}(a)$ improved Wilson-Clover with an ensemble provided by the consortium named *Coordinated Lattice Simulations* (CLS)[3], with $N_f = 2$ sea quarks, a lattice spacing $a = 0.065$ fm, a lattice size $32^3 \times 64$, a pion mass of 440 MeV (will be explained later) and 200 configurations. As expected, we can see a plateau where the low-lying state dominates and the fitting range of the mass term can be set. The results extracted from the lattice are dimensionless.

3.5 The Lattice Quark Propagator

The essential building block for dealing with hadrons on the lattice is the quark propagator: indeed, eq. (3.17) shows that the correlation functions can be calculated as a product of inverse Dirac operators. The Dirac operator for a specific flavor, in lattice QCD, is written as $D^{ab}_{\mu\nu}(y,x)$, where the indices $(a(b), \mu(\nu), x(y))$ are color, Lorentz and space-time, associated to the source (sink). The calculation of a propagator in lattice QCD is an arduous work, since the size of the matrix is $12N \times 12N$ (N is the number of lattice points), so it is only possible to calculate a subset of each matrix. The propagator G, defined as the inverse of the Dirac operator, satisfies

$$D^{ab}_{\mu\nu}(x,y)G^{bc}_{\nu\gamma}(y,z) = \delta(x,z)\delta_{ac}\delta_{\mu\gamma} \tag{3.24}$$

and depends on the lattice action. The Dirac operator contains only neighboring points of the lattice because it is built out of backwards/forwards derivatives. As a consequence we have a sparse matrix which allows (3.24) to be efficiently solved by algorithms based on conjugate

[3]The CLS is a community effort, launched in 2007, whose aim is to bring together the human and computer resources of several teams in Europe interested in lattice QCD. All information about this project can be found at https://twiki.cern.ch/twiki/bin/view/CLS/WebIntro.

gradient methods. Computing the solution from any source point to any sink point of the lattice (also called all-to-all inversion) is not currently possible due the existing computing capabilities. In some situations, when the computation of the all-to-all propagators [53] is really necessary (as for example in the case of non-local interpolating fields), one can use stochastic techniques or the distillation [54] method to obtain an estimation. In order to simplify the problem and find a solution, let us consider the following equation

$$D(x,y)\psi(y) = \delta(x) \tag{3.25}$$

where spinor and color indices are ommitted for simplicity. The solution vector $\psi(y) = G(y,x)\delta(x)$, corresponds to the one-to-all[4] solution for a point source placed at the origin ($\delta(x)$). Finally, using the γ_5-hermiticity relation $G(x,y) = \gamma_5 G(x,y)^\dagger \gamma_5$, we can obtain the backward propagator $G(y,x)$ without another inversion.

3.5.1 Quenching and partial quenching

Lattice QCD is a powerful tool for computing QCD observables which are connected with phenomenological studies such as hadron masses, decay constants, weak matrix elements and the strong coupling constant.

As mentioned in a former section, an issue arises from the fermion determinant, the logarithm of which is a non-local part of the gluon effective action (specially for light quark masses). This non-locality dramatically slows down the Monte Carlo algorithms. In order to circumvent this problem one can use an approximation called the *quenched approximation*, which consists in neglecting the effects of the determinant by setting the fermion determinant equal to one [55, 56], so that only valence quarks[5] are used to compute the correlators. The simulation considering quenched dynamical quarks corresponds to $N_f = 0$ (no dynamical flavor) simulation. However, not considering the contribution of the sea quarks, introduces an uncontrolled systematic error. In this case, it is highly recommended to work with the unquenched approximation to obtain precise predictions.

Unquenched QCD

When the dynamics of the sea quarks is included in the simulation, it is called *unquenched* lattice calculation. We then need to include the fermionic determinant that arises from integrating over the (Grassmann) quark fields. When refering to $N_f = 2$ lattice simulations, we are taking into account the effect of the light quarks in the sea (the quark up and the quark down are assumed to be degenerate). However, when one works with small quark masses, the computation time increases and the number of lattice points has to be increased in order to make the discretization effects negligible when compared to the statistical ones. A way out

[4] *Point(or one)-to-all* propagators: computation of quark propagators from one or a few points on the lattice (usually the origin) to all other points. This method works by inverting the fermion matrix with a point source, and combining the resulting propagators with appropriate operators to produce the desired hadronic correlators.

[5] Hadrons contain, along with the valence quarks (q_{val}) that contribute to their quantum numbers, virtual quark–antiquark ($q\bar{q}$) pairs known as sea quarks (q_{sea}). Sea quarks form when a gluon of the hadron's color field splits; this process also works in reverse in that the annihilation of two sea quarks produces a gluon [57].

consists in doing the computation assuming a large (unphysical) mass for the light quarks and, in the end, extrapolate to the real physical mass. In order to avoid the quenching effect of other flavors, the ETM Collaboration performs computations with $N_f = 2+1+1$ gauge ensembles [58–60] which include the unquenched strange and charm quarks. The heavy quarks impact at long distance of the QCD vacuum fluctuation should be much less important, since their mass is much larger than the typical scale $\mathcal{O}(\Lambda_{\mathrm{QCD}})$.

Partial quenching and the chiral limit

In full QCD, there is no difference between sea quarks and valence quarks. However, a full QCD simulation on a lattice is both time consuming and costly. Most of the simulation time is used to calculate changes in the determinant of the Dirac operator of light quarks [61]. Therefore, a usual approximation to extract information from sets of field configurations obtained in dynamical lattice gauge simulations[6] is the so-called *partial quenching*. In this approach, the hadronic properties are computed through configurations generated for a set of fixed sea quark masses, and then the quark propagators are studied by considering different valence quark masses. In this work, we have performed partial quenching for the two up and down light sea quarks ($N_f = 2$ simulations), where these values are to be extrapolated to the physical light quark mass. The standard chiral symmetry prediction for the dynamical pions is that their mass is controlled by the average quark masses [62]

$$m_\pi^2 \sim m_q + \mathcal{O}(m_q^2) \quad \text{where} \quad m_q = \frac{m_u + m_d}{2} \tag{3.26}$$

For this reason the pion mass will be used in this work as an indicator of the light quark masses. It is worth remembering that the pion mass is a physical observable and can be measured experimentally.

3.5.2 Smearing Techniques

In Lattice Gauge Theory, the masses are computed from two-point correlation functions and, as we saw before, the mass ground state dominates at large times. Thus, to obtain a clean signal we need to work with a time interval as large as possible. However, the longer the time, the noisier the signal, and the statistical errors become larger. In order to try to reduce the statistical error, we would have to enlarge the number of configurations, which is computationally expensive. So, we need to use some practical techniques to extract observables in a reliable way and without a large number of configurations.

One of the techniques that meets our needs is known as *smearing*. In the following sections, we will study two kinds of smearing: the Gaussian smearing, which is applied to the fermion fields, and the APE (Array Processor Experiment - APE Collaboration) smearing, which is applied to the gauge fields.

[6] A simulation including the fermion determinant and therefore allowing for the full dynamical vacuum structure of fermions is called a simulation with *dynamical quarks* [26].

Gaussian Smearing

Smearing along the spatial dimensions at the source is used to increase the overlap with the hadronic ground state. The idea is to spread the hadronic interpolating operator around its central location in space.

Gaussian Smearing [63, 64] can be done through a generalization of eq. (3.24),

$$D^{ab}_{\mu\nu}(x,y)G^{bc}_{\nu\gamma}(y,z) = \eta^{ac}_{\mu\gamma}(x,z) \tag{3.27}$$

where $\eta^{ac}_{\mu\gamma}(x,z)$ is an arbitrary source vector. In order to maximize the overlap of the resulting interpolator, it is appropriate to choose the source vector at the origin. There are many ways to smear the operator, one of them is known as Jacobi smearing, which gives Gaussian shaped sources. To perform this computation, the point source is chosen to be

$$\eta^{(0)ac}_{\mu\gamma}(x) = \delta(x,z)\delta_{ac}\delta_{\mu\gamma} \tag{3.28}$$

It is then iteratively applied to the wave function $F(\vec{x},\vec{x}')$

$$\eta^{(i)}(\vec{x}) = \sum_{\vec{x}'} F(\vec{x},\vec{x}')\eta^{(i-1)}(\vec{x}') \tag{3.29}$$

where

$$F(\vec{x},\vec{x}') = (1-\alpha)\delta_{\vec{x},\vec{x}'} + \frac{\alpha}{6}H'(\vec{x},\vec{x}') \tag{3.30}$$

and $H'(\vec{x},\vec{x}')$ is known as the hopping matrix

$$H' = \sum_{\mu=1}^{3} U_\mu(\vec{x})\delta_{\vec{x}',x+\hat{\mu}} + U^\dagger_\mu(\vec{x}-\hat{\mu})\delta_{\vec{x}',\vec{x}-\hat{\mu}} \tag{3.31}$$

The operator H' is essentially the spatial part of the Wilson term without the constant terms. In (3.30) the parameter α is a normalization factor

$$\alpha = \frac{1}{1+6\kappa_s} \tag{3.32}$$

with κ_s being the coupling strength of the nearest neighbor in space directions. If the procedure is repeated N times, the resulting fermion source is

$$\eta^N(\vec{x}) = \sum_{\vec{x}'} F^N(\vec{x},\vec{x}')\eta^{(0)}(\vec{x}') \tag{3.33}$$

where the parameters N and α govern the size and shape of the smearing function. One can observe on Fig. 3.4 the effective mass analysis, where we have applied smearing techniques in the propagators (in the source and/or in the sink), where the curves LS and SS are the ones where we applied this technique. We can observe an increase in the plateau for the ground state, when LS and SS are compared to the curve where no smearing was applied (LL).

APE Smearing

While Gaussian smearing is applied to fermionic fields, the APE smearing [65] is applied on the gauge fields. This kind of smearing has the purpose of removing, from the gauge links, the fluctuations which have short wavelengths by averaging them with their nearest neighbors. In other words, the quantum field configurations at short distances fluctuate wildly. Then, we want to reduce these short distance fluctuations. The procedure of link variables are made along certain paths connecting the end point of a link. The link variables are then replaced by the weighted average of such variables. In this way, the short distances (wavelengths) fluctuations are supressed. The APE procedure replaces the existing set of links $U_\mu(x)$ by

$$U_\mu^{(n+1)}(x) = U_\mu^{(n)} + \alpha_{\text{APE}} \sum_{\mu \neq \nu} U_\nu^{(n)}(x) U_\mu^{(n)}(x+\nu) U_\nu^{(n)\dagger}(x+\mu) \tag{3.34}$$

where α_{APE} is the APE smearing parameter which governs the relative weight of the fluctuations. Usually the APE smearing parameter is restricted to the range $0 \leq \alpha_{\text{APE}} \leq 3/4$, since beyond $3/4$ APE smearing does not lead to smooth gauge configurations [66]. The equation above is represented by Fig. (3.3) and the ensemble used here is the same than those used to plot Fig. (3.2). This transformation does not belong to $SU(3)$, so it is necessary, in the end, to project $U_\mu^{(n+1)}(x)$ onto $SU(3)$ ($P_{SU(3)}$),

$$U_\mu^{\text{APE}}(x) = P_{SU(3)} U_\mu^{(n+1)}(x) \tag{3.35}$$

This smearing process is iterated N_{APE} times.

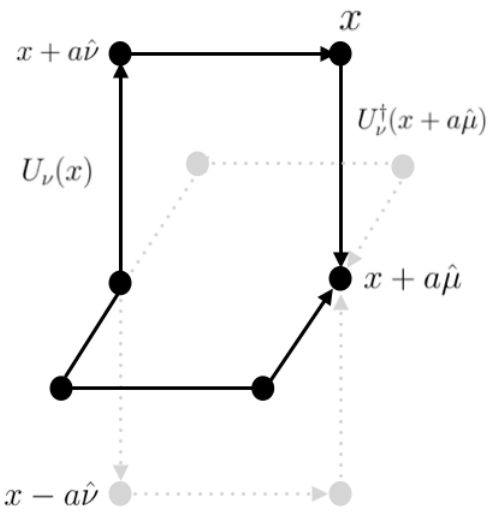

FIGURE 3.3: APE smearing applied in a gauge link.

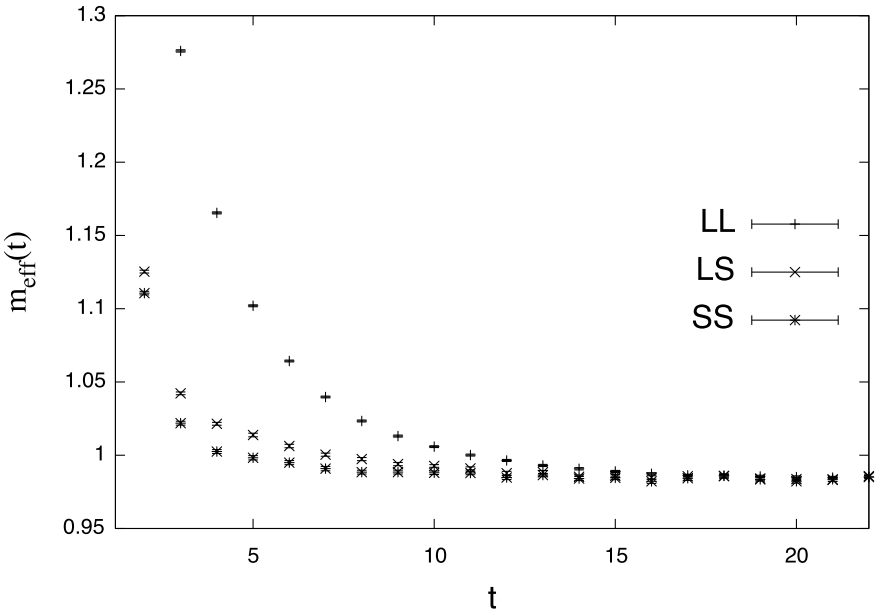

FIGURE 3.4: Effective mass extraction containing Smeared-Smeared (SS), Smeared-Local (SL) and Local-Local (LL) smearing techniques.

3.6 Matching to the Continuum Limit

3.6.1 The Continuum Limit

In the previous sections we have seen that the lattice action is reduced to the correct expression when we take the lattice spacing limit $a \to 0$. All observables extracted from the lattice are written in lattice units. Then, in order to compare the results with experiment, it is important to convert them into physical units. This procedure is called *scale setting* and consists in computing the lattice spacing in physical units by imposing one observable (computed on the lattice) to match its physical value. The setting of the scale and the adjust of the quark masses are related. The scale[7] is defined by [26]

$$a[\mathrm{MeV}^{-1}] = \frac{(aX)_{\mathrm{lattice}}}{X_{\mathrm{phys.}}[\mathrm{MeV}]} \tag{3.36}$$

where the value of the observable computed on the lattice is $(aX)_{\mathrm{lattice}}$ and $X_{\mathrm{phys.}}$ is its physical value in MeV. Usually the observables chosen for this task are: the pion and kaon decay constants f_π, f_K [67], a hadron mass (it could be the nucleon or the ρ mass) or the Sommer parameter r_0 [68]. However, the determination of such observables is not the same due to the difficulty of their evaluation. If one chooses to work with the nucleon mass as a reference, we need to extrapolate the result to the physical mass of quarks, which correspond to $m_\pi \simeq 139$ MeV [1]. Nevertheless, due to the limitation in computer power, we performed computations with a pion mass $m_\pi \gtrsim 300$ MeV [69], which introduces systematic errors. Then, in order to choose the good observable we need to take into account those which do not depend heavily on the mass of the quarks and are easily computed in the lattice. In addition,

[7] The conversion factor between fm and MeV is $1\ \mathrm{fm}^{-1} = 197.327$ MeV [1].

they should have small statistical error to allow for a precise estimation. The error on the scale affects not only the quantities expressed in physical units but also the continuum and chiral extrapolations.

Quark Masses

In this work, the light quarks (up and down) are assumed to be degenerate and their masses can be set by computing just one observable, like the pion mass (see Section 3.5.1). The pion mass is computed in lattice units $(am_\pi)_{\text{lattice}}$ and the result is converted in physical units using the previous estimation of the lattice spacing:

$$m_\pi[\text{MeV}] = \frac{(am_\pi)_{\text{lattice}}}{a[\text{MeV}]^{-1}} \tag{3.37}$$

An indirect consequence of setting the scale at finite lattice spacing is the so-called *scale ambiguity* [70]. That is, the calibration of the lattice spacing in physical units $a[\text{MeV}^{-1}]$, is dependent on the quantity $X_{\text{phys.}}$ which is used to set the scale. This ambiguity arises because different quantities $X_{\text{phys.}}$ are affected by quark loops in different ways. However, this ambiguity should vanish in the continuum limit and does not affect the results extrapolated to $a \to 0$.

Light Hadrons for $N_f = 2$

In this section we give more details on the simulation using the so-called *partially quenched* approximation (see Section 3.5.1). The two flavors of (degenerate) dynamical quarks with mass m^{sea} are normally identified with the physical u and d quarks . On the lattice it is possible to compute observables relating to hadrons whose valence quarks have a different mass than the sea quarks $m^{\text{val}} \neq m^{\text{sea}}$ (see Fig. 3.5). As a consequence, one has more freedom to explore separately the dependence of physical observables on m^{val} and m^{sea}. In this case, usually one introduces the strange quark as a valence quark. Nowadays, the values of m^{sea} which are accessible are still relatively large.

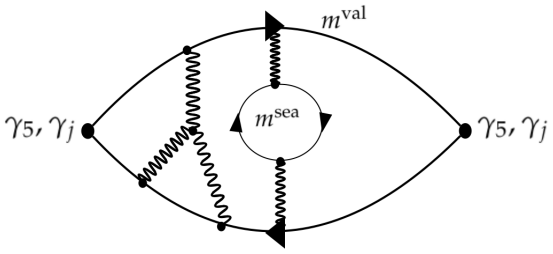

FIGURE 3.5: Quark and gluon contributions ot the two-point function for a pseudoscalar (vector) meson in partially quenched QCD with $m^{\text{val}} \neq m^{\text{sea}}$.

3.7 The Error Estimation

In order to efficiently extract the physical observables in LQCD, the errors must be controlled, and computer time should be left to a minimum. In a Monte Carlo simulation, the Markov chain has a finite size, then the same configurations are used to compute different observables which are therefore correlated. Moreover, since the Markov Process generates the new gauge configuration from the previous one, it also introduces autocorrelation. Consequently, the estimation of the statistical errors in numerical lattice QCD becomes a non-trivial task under these conditions. One possible solution to tackle these autocorrelation effects is the use of resampling techniques such as the *jackknife* or the *bootstrap* methods.

Data Blocking Methods

The idea is to divide the data into sub-blocks of data with size N, to compute the block mean values and consider them as new variables X_i. The variance of these blocked X_i should decrease like $1/N$ if the original data is independent. One needs to repeat this procedure for a sequence of different values for N. As soon as the behavior $1/N$ is observed for a large enough N one can consider these block variables as statistically independent. Once the data is considered independent, one can determine the expectation values of the observables of interest and their errors. If the data is too small to get a reliable estimate of the variance of the computed expectation values, one needs to use different tools such as the *jackknife* or the *bootstrap* method.

The Jackknife Method

The Jackknife samples are selected by taking the original data vector and subtracting one observation from the full set. Then, we will get N unique Jackknife samples (also called bins), since we are removing the n^{th} entry of the original set ($n = 1 \dots N$). If the n^{th} measurement is omitted, the corresponding jackknife sample is defined by [71]:

$$m_1, m_{n-1}, m_{n+1}, \dots, m_N \tag{3.38}$$

Then, the method consists in removing one configuration at each time and calculating the average $\bar{m}_{(n)}$ of the full set, using the data of the remaining configurations

$$\bar{m}_{(n)} = \frac{1}{N-1} \sum_{n' \neq n} \bar{m}_{(n')} \tag{3.39}$$

We divide our data into N blocks and each block has a length greater than the correlation time τ_{corr} in order to get rid of autocorrelations. The error on m is estimated by computing the deviation from $\bar{m}$

$$\delta_m = \sqrt{\frac{N-1}{N} \sum_{n=1}^{N} (\bar{m}_{(n)} - \bar{m})^2} \tag{3.40}$$

where the pre-factor $(N-1)$ corrects the fact that our variables are not independent.

The Bootstrap Method

This method is similar to the Jackknife method. We will separate our data into N blocks and each block has a length greater than the correlation time τ_{corr}. From the set of N blocks, we take N' blocks randomly, i.e. a bootstrap sample. Then we compute our variable of interest $\bar{m}$ over the selected data. And this procedure is repeated N_B times in order to generate the bootstrap sample $(\bar{m}_1, \bar{m}_2, \ldots, \bar{m}_{N_B})$. Thus the standard deviation writes:

$$\delta m = \sqrt{\frac{1}{N_B - 1}\sum_i (\bar{m}_n - \bar{m})} \quad \text{where} \quad \bar{m}_n = \frac{\sum_n \bar{m}_n}{N_b} \tag{3.41}$$

The size of the bootstrap samples will depend on the size of the data. And N_B can go up to 1000. In a practical implementation, both bootstrap and jackknife are combined with blocking. The idea is to construct subsets and remove blocks instead of single values. In our work, we compute quantities obtained from an exponential fit of the two-point correlation function. A single measurement of the correlator fluctuates too much for a reasonable fit. So we need to average many measurements of the correlator before perfoming a fit and for the error estimation we need many of those sets of data for the correlator. Therefore we use jackknife and bootstrap methods. They can be applied to the determination of statistical error for fitted quantities. The sets produced by those methods are large enough for performing a fit.

3.8 Systematic Errors

A lattice calculation is subject to different types of systematic errors, which are related to the simulation parameters.

Discretization Effects

The physical observables extracted from the lattice differ from the continuum value by finite terms. These additional terms are called, in general, discretization errors. In lattice QCD, the same physical observable is computed at various lattice spacings and then, in order to get the continuum limit, we extrapolate the lattice spacing to zero. To reduce the error as much as possible, one should work with the smallest lattice spacings. The size of the lattice spacing is actually determined by the computational power at our disposal.

Finite size effects

On the lattice, the finite lattice spacing a and the finite volume $(L^3 \times T)$ are sources of systematic errors. And as we mentioned before, all the results from the lattice are obtained in finite volumes. An important parameter to reduce the finite size effect is the boundary condition taken for quark fields. The use of periodic boundary conditions in the spatial direction helps to reduce the finite size effects asymptotically [72, 73] and they are exponentially supressed

($\sim (e^{-m_\pi L})$). The associated corrections of order $\mathcal{O}(e^{-m_\pi L})$ were computed in Ref. [74] and decrease exponentially with the volume. Some groups estimated that finite volume shifts are sub-percent effects when $m_\pi L \gtrsim 4$, and most large-scale simulations use lattices satisfying this condition. This becomes challenging as one approaches the physical pion mass, for which $L \simeq 5$ fm is required. At present, this can only be achieved by using relatively coarse lattices, $a \simeq 0.07$ fm. The CLS ensembles, which are the ones used in this work, follow the rule that for $Lm_\pi \gtrsim 4$ the finite size effect are expected to be very small and can be ignored.

Dynamical Quarks

The evaluation of the quark propagator on the lattice becomes more difficult as the pion mass gets closer to its physical value [26, 75]. Therefore, many lattice simulations are performed at non-physical quark masses. In order to estimate the systematic errors associated to these computations, different simulations at several quark masses are performed and the results are extrapolated to the chiral limit [76, 77]. Moreover, we have another source of systematic errors coming from the fact that only two dynamical quarks are used in the simulations (quark loops with c, s, b and t are neglected) and the associated error is more complicated to estimate.

3.8.1 Non-perturbative Renormalization Constants

The observables extracted from the lattice are all bare quantities. As a consequence, in many applications of lattice QCD it is mandatory to deal with renormalization. As an example, we can mention the extraction of quark masses. A more complex example is to compute a transition or decay amplitude of hadrons induced by interactions in the electroweak theory. The low energy effective operators are constructed through operator product expansion. They, in turn, are plugged in the QCD Lagrangian, with the Wilson coefficients calculated through (continuum) perturbation theory. The coefficients are often divergent, so we need to renormalize them with a certain renormalization scheme and scale. The lattice task is to calculate the matrix element of the operator between hadron states. The matrix element of the bare operator has the same divergence as the Wilson coefficient. In divergent cases, the matrix element or the operator must undergo a renormalization on the lattice. The same renormalization scheme and scale as the Wilson coefficient must be used to compensate the dependence on it, so that the final, physical matrix element is scheme and scale-independent. For further details, see for example Ref. [78].

An operator $\mathcal{O}$ can be renormalized as (multiplicative renormalization)

$$\mathcal{O}_{\text{ren}}(a) = Z_{\mathcal{O}}(a)\mathcal{O} \tag{3.42}$$

where $Z_{\mathcal{O}}$ is the renormalization factor, normally a function of a. The renormalization parameters are calculated using perturbative or non-perturbative theory.

The most popular non-perturbative renormalizations (NPR) on the lattice are the Rome-Southampton method (also known as the RI/MOM scheme) and the Schrödinger functional (SF) scheme [78]. In this work we use the renormalized constants provided by the ALPHA Collaboration, where the SF scheme is used [67].

RI/MOM scheme

The underlying idea is to compare bare lattice correlation functions, couplings, and masses determined in lattice calculations with quantities in the so-called *Regularization-independent* (RI) scheme (also known as RI/MOM scheme) [79]. The RI/MOM scheme is a popular NPR scheme for multiquark operators. The procedure is very similar to the one used in the continuum perturbation theory. The renormalization factors, obtained for different values of the renormalization scale, are evolved perturbatively to a reference scale $\mu = 2$ GeV.

The renormalized (R) quark field, mass and bilinear operator are written in terms of the bare (B) quantities as

$$\psi_R = \sqrt{Z_q^{\mathrm{RI/MOM}}}\psi \ , \ m_R = Z_m^{RI/MOM} m_B \ , \ \mathcal{O}_R = Z_{\mathcal{O}}^{RI/MOM}\mathcal{O}_B \tag{3.43}$$

$Z^{\mathrm{RI/MOM}}$ are the renormalization factors in the RI/MOM scheme. The computation of these renormalization factors was done in Ref. [80].

Generally, one wants to make contact with phenomenological studies, which almost exclusively refer to operators renormalized in a *Minimal Subtraction* ($\overline{\mathrm{MS}}$) scheme. In order to do that, one needs to connect the RI-MOM quantities to those defined in the $\overline{\mathrm{MS}}$ scheme, which can be accomplished in continuum perturbation theory [81]. In the two schemes, the renormalization factors are related by

$$Z^{\overline{\mathrm{MS}}}(\mu^2) = R^{\overline{\mathrm{MS}}/\mathrm{RI/MOM}}(\mu^2) Z^{\mathrm{RI/MOM}}(\mu) \tag{3.44}$$

where the ratio $R^{\overline{\mathrm{MS}}/\mathrm{RI/MOM}}(\mu^2)$ is computed in perturbation theory. Perturbative conversion ratios for RI/MOM to the $\overline{\mathrm{MS}}$ scheme can be found in Refs. [80, 82].

ALPHA Collaboration

As we mentioned before, the renormalized parameters we use in this work were computed by the ALPHA collaboration[8]. One of their main objectives is the computation of renormalized parameters with the highest precision possible. Some of the recent results have been presented in Refs. [83, 84]. The emphasis of the ALPHA project is on precision and directly associated with this, an attempt to carefully control systematic errors [85]. The idea is to compute non-perturbatively defined running couplings and quark masses over a wide range of energies where the contact with hadronic mass parameters is made in order to study for example hadron properties. In order to make a link with perturbation theory it is essential that the simulation reaches a range of high energy where the predicted behavior actually appears to set in. A full explanation about this project can be found in Ref. [85].

Schrödinger functional scheme

The SF scheme [86–88] is used as the intermediate scheme to carry out non-perturbative running from the low energy region, where the renormalization of the bare mass is performed

[8] For more information, please see https://www-zeuthen.desy.de/alpha/.

on the lattice, to the high energy perturbative region, where the conversion to the renormalization group invariant mass or the $\overline{\text{MS}}$ scheme is safely carried out [89]. In this framework, one studies the system in a cylindrical volume Λ with Dirichlet boundary conditions in one (the temporal) direction and periodic boundary conditions in the other (spatial) directions. The symmetry properties of the SF functional in LQCD should be the same if the choosen lattice Dirac operator preserves chiral symmetry via the Ginsparg–Wilson relation (see Chapter 2). However, since there are different boundaries conditions, the Dirac operator and the Ginsparg-Wilson relation should be both modified. The modifications should be local and be linked to the boundary conditions. In our simulations, we did not work directly with the SF scheme, since we applied the values already calculated by the ALPHA collaboration. For more details about the SF scheme computation, see, for example, Refs. [90, 91].

3.9 Summary

In this chapter, we have studied methods to extract an observable from the lattice. Also, we have presented techniques to calculate the propagators and methods to improve the signal. In addition, we discussed how to renormalize the results and how to transfer them from the lattice to the *real world*. In the following chapters, we will focus on the extraction of some meson properties.

Chapter 4

Hadron Spectroscopy for Excited States

The first step in Lattice QCD numerical simulations is the determination of the lowest hadron masses (coresponding to the ground state). Since these masses are experimentally well known with a high precision, the comparison with the numerical results is an important check of the method which can then be applied to infer information on the properties of excited states. In the previous chapter, we have discussed some topics in hadron spectroscopy, for example, the extraction of the ground state mass (see section 3.4). Moreover, we discussed how to obtain the relevant contributions to the ground state, by analyzing the correlator at large times.

The next step is the study of the excited states. In order to extract the spectrum of the excited states, we could perform a multi-exponential fit, but that approach is unstable. For this reason, other approaches have been developed. In this work, we decided to use one specific method, which is inspired by the variational method in quantum mechanics and consists in increasing the basis of operators in order to build a matrix of correlators $C_{ij}(t)$ for which a Generalized Eigenvalue Problem (GEVP) is formulated [92, 93]. The GEVP involves *all-to-all* propagators [53] instead of one-to-all point sources as indicated in the previous sections. *All-to-all* propagator represents a quark traveling from any point of lattice to any other point. Moreover, it is a helpful tool to reduce systematic errors. The GEVP will be explained in detail in Section 4.3. In this chapter (in Section 4.1), we also present two lattice techniques, which make the calculations easier and improve the quality of the signal over the noise. In lattice QCD the signal quality is indeed very important for a reliable extraction of the physical observables. Finally, we will describe some of our results for the excited state calculation.

4.1 Lattice Techniques

In Section 3.5 we have explored a method for computing the lattice quark propagator. However, a drawback of this method is that only a small part of the gauge information is used since we do not exploit the full translational invariance of the propagator (the source is fixed). Since generating gauge configurations is extremely costly, it would be preferable to exploit them to reduce the gauge noise. Moreover, point-to-all propagators are not suited when using non-local interpolating fields. In order to circumvent this issue, we will consider two methods. The first one is known as *all-to-all propagators* [53] and the second one, which is responsible for the reduction of the noise is called *time dilution* [53]. Furthermore, a stochastic estimation of the propagators will be implemented using the one-end trick method.

4.1.1 Stochastic All-to-all Propagators

Solutions exist to evaluate all-to-all propagators and are based on stochastic methods [53]. The idea is to use, for each gauge configuration, an ensemble of N_s[1] stochastic sources satisfying

$$\frac{1}{N_s}\sum_{s=1}^{N_s}\eta^a_\alpha(x)_s\left[\eta^b_\beta(y)_s\right]^* = \delta_{\alpha\beta}\delta^{ab}\delta_{x,y} \tag{4.1}$$

where each component is normalized to one, $\eta^a_\alpha(x)^*_{[r]}\eta^a_\alpha(x)_{[r]} = 1$ (no summation). The indices (a,α) and (b,β) respectively denote color and spinor pairs. In order to implement this method one can use random Gaussian numbers on each site of the lattice, for each color and spinor index. Then the Dirac operator is inverted for each source:

$$D^{ab}_{\alpha\beta}(x,y)\psi^b_\beta(y)_s = \eta^a_\alpha(x)_s \tag{4.2}$$

where $\psi^a_\alpha(x)_s$ is the solution vector of size $12N$. Finally, we have an unbiased estimator of the propagator from any spacetime point x to any other spacetime points y:

$$\psi^a_\alpha(x)_s = G^{ab}_{\alpha\beta}(x,y)\eta^b_\beta(y)_s \implies G^{ab}_{\alpha\beta}(x,y) = \frac{1}{N_s}\sum_{s=1}^{N_s}\psi^a_\alpha(x)_s\eta^b_\beta(y)^*_s \tag{4.3}$$

The number of stochastic sources is always finite and, since the inversion of the Dirac operator is often the most demanding part of the algorithm, it can be quite limited. Then, the condition (4.2) is only approximately fulfilled and the quark propagator obtained from eq. (4.3) can be very noisy. Naïvely estimating the signal-to-noise ratio leads to $S = V\sqrt{N_s^2/V^2} = N_s$ where $V = L^3 \times T$. A possible solution to reduce the noise is *time dilution*.

4.1.2 Time Dilution

This method consists in splitting the source η into several secondary (diluted) sources with vanishing overlap. We have a secondary source defined on a single time slice and equal to zero elsewhere. The advantage is that the condition (4.2) is automatically fullfield. Since the time dependence of the quark propagator is known to be large, this leads to a significant variance reduction

$$\eta(\vec{x},t) = \sum_\tau \eta(\vec{x},t)_{[\tau]} \quad , \quad \eta(\vec{x},t)_{[\tau]} = 0 \quad (t \neq \tau) \tag{4.4}$$

The Dirac operator is now inverted on each diluted source and the full propagator is recovered by summing over all the secondary sources:

$$G^{ab}_{\alpha\beta} = \frac{1}{N_\tau}\sum_\tau \psi^a_\alpha(x)_{[\tau]}\eta^b_\beta(y)^*_{[\tau]} \tag{4.5}$$

[1] Generally $N_s = 1$, i.e. a single inversion per gauge link configuration.

If $N_\tau = N_s \times T$, we have full-time dilution. Furthermore, dilution could also be applied to spinor or color indices. The limit where dilution is applied to all space-time, color and Dirac indices would correspond to the computation of the exact all-to-all propagator. An advantage of this method is that timeslices sources are usually more efficient than volume sources, when one is interested in the behavior of the correlation functions at large times. A naïve estimation of the signal-to-noise ratio now gives $S = V_s\sqrt{N_s^2/V_s^2} = N_s$ where $V_s = L^3$.

4.1.3 One-End Trick

The signal-to-noise ratio can be radically improved by using the so-called *one-end trick* [94–97]. In this method, which is slightly different from the previous ones, we start by considering the spin diluted timeslice sources,

$$\eta[\tilde{\alpha},t]^a_\alpha(x)_s \equiv \delta_{\alpha,\tilde{\alpha}}\cdot\Xi[\tilde{t}]^a(x)_s, \quad \text{with} \quad \Xi[\tilde{t}]^a(x) = \delta(t-\tilde{t})\cdot r \tag{4.6}$$

where r represents a random number. The sources are non-zero in a single time-slice $\tilde{t}$. All entries of Ξ on a time slice $\tilde{t}$ are chosen independently. The optimal way to choose the time-slice at which the stochastic source is located, is to change it randomly as the gauge configuration is changed. The sources now satisfy

$$\frac{1}{N_s}\sum_{i=1}^{N_s}\eta[\tilde{\alpha},\tilde{t}]^a_\alpha(x)_i\left[\eta[\tilde{\beta},\tilde{t}]^b_\beta(y)_i\right]^* = \delta_{ab}\delta_{\alpha\beta}\delta_{\alpha\tilde{\alpha}}\delta_{\beta\tilde{\beta}}\delta(x-y)\delta(t_x-\tilde{t})\delta(t_y-\tilde{t}) \tag{4.7}$$

The lattice Dirac operator D is inverted (for one given flavor) on each sample of this source. Also, one introduces the *ψ-propagator* which is a solution of the equation

$$\sum_y D[f]^{ab}_{\alpha\beta}(x,y)_s\psi[f,\tilde{\alpha},\tilde{t}]^b_\beta(y)_s = \eta[\tilde{\alpha},\tilde{t}]^a_\alpha(x)_s \tag{4.8}$$

where f represents the fermion flavor. By using the previous relations we can obtain an unbiased estimator of the all-to-all propagator, which is the inverse of the Dirac operator, by computing the quantity,

$$\frac{1}{N_s}\sum_{s=1}^{Ns}\psi[f,\tilde{\alpha},\tilde{t}]^b_\beta(x)_s\left[\eta[\tilde{\alpha},\tilde{t}]^a_\alpha(y)_s\right]^* \tag{4.9}$$

The major advantage of the one-end trick is that the signal-to-noise ratio is now $S = V_s\sqrt{N_s/V_s} = \sqrt{N_sV_s}$ where $V_s = L^3$. We have an improvement by a factor $\sqrt{V_s/N_s}$ (where $\frac{V_s}{N_s} \gg 1$) compared to what had been obtained for time dilution.

4.2 Decay Matrix Element

Before starting our discussion about the Generalized Eigenvalue Problem, we will study the procedure to compute decay constants. We present the direct method to extract the decay matrix elements, in particular for the pseudoscalar case and the vector case. The following

equations will be used to extract the physical observables for the ground state or for the excited states. In Section 4.3, we will describe the procedure we have used: the Generalized Eigenvalue Problem.

Vector Case

For an arbitrary vector meson[2] M_V, the definition of the decay constant f_V in the rest frame is (see Appendix A for details)

$$\langle \Omega | V_\mu | M_V(\lambda, \vec{p}) \rangle = \epsilon_\mu^{(\lambda)}(\vec{p}) f_V m_V \tag{4.10}$$

where $\epsilon_\mu^{(\lambda)}(p)$ is the polarization tensor of the vector state (λ is the polarization index) and $V_\mu \equiv \bar{q}\gamma_\mu q$ is the vector current. After inserting a complete set of eigenstates and assuming large enough times t

$$C_{ij}(t) \xrightarrow{t\to\infty} \underbrace{\underbrace{\sum_\lambda \epsilon_i^{(\lambda)}(\vec{0})\epsilon_j^{*(\lambda)}(\vec{0})}_{\delta_{ij}} f_V^2 m_V^2}_{2m_V \mathcal{Z}_{VV}\delta_{ij}} \times \frac{e^{-m_V t}}{2m_V} \tag{4.11}$$

Hence, we can compute the vector meson decay constant using,

$$f_V = \sqrt{\frac{2\mathcal{Z}_{VV}}{m_V}} \tag{4.12}$$

where we know the values of $\mathcal{Z}_{VV}$ by performing a fit in $C_{ij}(t)$ and m_V, since we extract the vector mass by fitting (4.10) at large times.

Pseudoscalar Case

For an arbitrary pseudoscalar meson[3] M_P, the definition of the decay constant f_P in the rest frame is (calculation similar to the vector case done in Appendix A),

$$\langle \Omega | A_0 | M_P(\vec{p} = \vec{0}) \rangle = f_P m_P \tag{4.13}$$

where m_P is the meson mass (already extracted by a fit) and A_0 is the temporal component of the axial current $\gamma_\mu\gamma_5$. To study the pseudoscalar case, we will use the two-point correlation function in (3.13), where $\mathcal{O}_1$ is the axial interpolating operator, $A \equiv \bar{q}\gamma_0\gamma_5 q$ and $\mathcal{O}_2$ the pseudoscalar $P \equiv \bar{q}\gamma_5 q$. In the rest frame we start from

$$C(t) = \sum_{\vec{x}} \langle \Omega | A(t, \vec{x}) P^\dagger(0, \vec{0}) | \Omega \rangle \tag{4.14}$$

[2] Total spin 1 and odd parity $J^P = 1^-$
[3] Total spin 0 and odd parity $J^P = 0^-$

After inserting a complete set of eigenstates and assuming large enough times t,

$$C(t) \xrightarrow{t\to\infty} \underbrace{\underbrace{\langle\Omega|A(0)|M_P\rangle}_{f_P m_P}\underbrace{\langle M_P|P^\dagger(0)|\Omega\rangle}_{\sqrt{2m_P}\sqrt{\mathcal{Z}_{PP}}}}_{2m_P\mathcal{Z}_{AP}} \times \frac{e^{-m_P t}}{2m_P} \tag{4.15}$$

and hence we obtain the final relation for the pseudoscalar decay constant

$$f_P = \sqrt{\frac{2}{m_P}}\frac{\mathcal{Z}_{AP}}{\sqrt{\mathcal{Z}_{PP}}} \tag{4.16}$$

where the coefficients $\mathcal{Z}_{PP}$ and m_P have already been calculated and $\mathcal{Z}_{AP}$ can be obtained by fitting (4.14) at large times.

Errors in Decay Constants

Normally the errors in decay constants are larger than those in the determination of masses. For example from eq. (4.15) one notes that for 1% error in the determination of the mass, the error in the decay amplitude is $\approx \sqrt{e^{0.01 m_P t}} - 1 \approx 0.005 m_P t$. If the fit has $m_P t \approx 5$ for $1/a \sim 2$ GeV lattices, the error in the decay constant is $\geq 3\%$. For more details see, for example, Ref. [98].

Renormalization

The quantities so far studied are bare quantities and, as we already discussed, we should renormalize the local operators, in order to define properly the physical quantities. There are many groups working on this renormalization procedure, and for our work we choose the renormalization constants proposed by [99] and [100]. We will thus rewrite (4.16) and (4.12) using the renormalization constants Z_A, for the pseudoscalar case, and Z_V, for the vectorial case, leading to

$$f_P^R = Z_A\sqrt{\frac{2}{m_P}}\frac{\mathcal{Z}_{AP}}{\sqrt{\mathcal{Z}_{PP}}} \tag{4.17}$$

and

$$f_V^R = Z_V\sqrt{\frac{2\mathcal{Z}_{VV}}{m_V}} \tag{4.18}$$

The values of Z_A and Z_V will be presented later, in Section 5.2.3.

4.3 The Generalized Eigenvalue Problem

The preceding chapter explained how to compute the ground state properties by studying the large time behaviour of two-point correlation functions. Using just one interpolating field,

the extraction of ground state information is often not very reliable, and the signal gets even worse for the first excited state. Therefore, more sophisticated methods are required.

One idea is to use different interpolating operators, with different overlaps with the excited states, and combine them to create an improved operator with the largest overlap with the ground state. This can be done systematically by solving a Generalized Eigenvalue Problem. The GEVP has been proven to be a robust and useful tool for this kind of studies (for a detailed discussion, see Refs [101–104]). Though our work only focuses on the study of two-point correlation functions, we point out GEVP studies, applied to three-point functions. An exhaustive discussion can be found in Refs [105–108].

The Method

An extensive explanation of the GEVP can be found in Appendix B, and here we will just discuss its main features. The basic idea is to use a basis $\mathcal{O}_D$ of several different interpolating fields with the same quantum numbers that ideally couple to different energy states. We construct a matrix of cross-correlators[4],

$$C_{ij}(t) = \begin{bmatrix} <\Omega|\mathcal{O}_1(t)\mathcal{O}_1^\dagger(0)|\Omega> & <\Omega|\mathcal{O}_1(t)\mathcal{O}_2^\dagger(0)|\Omega> & \dots \\ <\Omega|\mathcal{O}_2(t)\mathcal{O}_1^\dagger(0)|\Omega> & <\Omega|\mathcal{O}_2(t)\mathcal{O}_2^\dagger(0)|\Omega> & \dots \\ \vdots & \vdots & \ddots \end{bmatrix} \tag{4.19}$$

where the basis of interpolating fields is

$$\mathcal{O}_D = \{\mathcal{O}_1, \mathcal{O}_2, \mathcal{O}_3, \dots, \mathcal{O}_N\} \tag{4.20}$$

A variational analysis can then be undertaken to produce correlation functions that couple strongly to the state of interest.

Choosing Good Interpolating Fields

At this point, it is useful to ask how to construct a *good* set of interpolating fields in order to ensure a reliable state identification at finite lattice spacing, and to increase the statistical precision in our computation. The important features to be taken into account include:

- The operator should not be noisy, i.e., it should produce a correlator with acceptable statistical precision over a reasonable number of timeslices;
- The basis of operators should have a high overlap with the states of interest (which are the eigenvectors of the GEVP) and this basis of operators are or are close to be linearly independent.

Let us not forget that, in order to improve statistical precision, we can use smearing techniques (presented in Section 3.5.2) as well as noise reduction in all-to-all propagators through time dilution (4.1).

[4] We are assuming the rest-frame in the following discussion.

Having chosen the variational basis, the variational technique yields the so-called Generalized Eigenvalue Problem (GEVP), which amounts to solving

$$C(t)v_n(t,t_0) = \lambda_n(t,t_0)C(t_0)v_n(t,t_0) \tag{4.21}$$

where $C(t)$ is the $N \times N$ matrix of correlators $C_{ij}(t)$ that appears in eq. (5.7), $\lambda_n(t,t_0)$ and $v_n(t,t_0)$ are respectively the eigenvalues and the eigenvectors of this matrix. In GEVP, it is recommended to choose a time slice $t_0 < t$ in order to improve the signal by suppressing the contributions from higher excited states. The method can be improved by increasing the number of interpolators. However, when more operators are included, one enhances the statistical noise and thus the matrix has problems to converge to the eigenvalues.

4.3.1 Mass Extraction

When solving the GEVP (see Appendix B), the eigenvalues behave as

$$\lambda_n(t,t_0) = e^{-m_n(t-t_0)} \quad \text{(unbounded time)} \tag{4.22}$$

and the traditional method to extract the mass m_n of the n^{th} state is to consider

$$m_n^{\text{eff}}(t,t_0) = -\frac{\partial \log \lambda_n(t,t_0)}{\partial t} = \log \frac{\lambda_n(t,t_0)}{\lambda_n(t+1,t_0)} \tag{4.23}$$

Therefore, at large time separations ($t \to \infty$), each eigenvalue is dominated by a single state, allowing a stable two parameter fit. In practice, to extract the masses using the GEVP, one needs to do the following steps:

- Calculate the correlation matrix for a given set of interpolators;
- Check that the matrix has real eigenvalues, since the matrix $C(t)$ needs to be Hermitian for all Euclidean times t, and $C(t_0)$ needs to be positive definite;
- Diagonalize the $C(t)$ matrix at each time slice, and sort the eigenvalues according to their magnitude.

For the analysis, truncating the matrix to a suitable sub-matrix of interpolators could be useful as it may provide results with a smaller statistical uncertainty.

4.3.2 Matrix Element Extraction

We will also need to compute matrix elements, in order to extract other observables such as decay constants. While the mass extraction required the eigenvalues of the GEVP, extracting matrix elements further requires the eigenvectors of the GEVP.

First, we introduce the effective matrix element

$$\langle \Omega|\hat{\mathcal{P}}|n\rangle^{\text{eff}}(t) = \sqrt{2E_n}\left(\frac{\lambda_n(t,t_0)}{\lambda_n(t+1,t_0)}\right)^{t/2} \frac{\sum_{i=1}^{N}\langle \Omega|\mathcal{P}(t)\mathcal{O}_i^\dagger(0)|\Omega\rangle}{\sqrt{(v_n(t,t_0),C(t)v_n(t,t_0))}} \tag{4.24}$$

where $\mathcal{O}_i$ is one of the interpolating fields of the basis (4.20) and $\mathcal{P}$ is an operator (which can be, or not, one of the operators $\mathcal{O}_i$). We notice that in eq. (4.24) the matrix element is written taking into consideration all the elements provided by the GEVP method (the eigenvalues and the eigenvectors) as well as the correlator matrix (4.19) and the two-point correlation function. The effective matrix element will converge at large enough times t to the true matrix element

$$\langle \Omega | \hat{\mathcal{P}} | n \rangle^{\text{eff}} (t) \xrightarrow{t \to \infty} \langle \Omega | \hat{\mathcal{P}} | n \rangle (t) \tag{4.25}$$

To extract the matrix elements, one needs to use resampling techniques like jackknife (see Section 3.7) in the eigenvectors in order to get consistent samples. Besides, the GEVP depends on the reference timeslice t_0, so to be able to do a good analysis of the data, one needs to test this parameter to see the robustness of the results. Particularly, if t_0 is chosen too small, then the states with energies larger than that of interest will contaminate the results. On the other hand, if one chooses values of t_0 too large, numerical instabilities may result. We will later discuss the choice of t_0 in our simulations.

4.4 Data Analysis and Fitting Procedure

In this section, we will address some aspects regarding the fit done to extract the mass, and subsequently present the computational tools which were used to analyze the data.

Data Analysis

As in eq. (3.23), we define the effective mass

$$m_n^{\text{eff}}(t, t_0) = \log \frac{\lambda_n(t, t_0)}{\lambda_n(t+1, t_0)} \tag{4.26}$$

where the eigenvalue $\lambda_n(t, t_0)$ corresponds to the n^{th} state, as obtained from the GEVP. We can observe in Fig. 4.1 a plot of typical effective masses. We also present the effective mass (computed with eq. (4.26)) as a function of time for the charmonium pseudoscalar states $\eta_c(1S)$ and $\eta_c(2S)$ (respectively, ground and excited states). In this simulation, the fermions are $\mathcal{O}(a)$ improved Wilson-Clover with an ensemble provided by the CLS consortium with $N_f = 2$ sea quarks, a lattice spacing $a = 0.065$ fm, a lattice size $32^3 \times 64$, a pion mass of 440 MeV and 200 configurations. We have computed a 2×2 matrix

$$C(t) = \begin{bmatrix} \langle P(t)P(0) \rangle & \langle A_0(t)P(0) \rangle \\ \langle P(t)A_0(0) \rangle & \langle A_0(t)A_0(0) \rangle \end{bmatrix} \tag{4.27}$$

where $P = \bar{c}\gamma_5 c$ and $A_0 = \bar{c}\gamma_0\gamma_5 c$ are, respectively, the pseudoscalar and axial interpolating fields. We will discuss this topic in more details on Chapter 5. The effective mass plateaus (where we have performed a fit) are represented by a solid line within defined intervals of time. The plateau coming from the ground state is found in a wider interval of time than the excited state one: in Fig. 4.1 we choose $t \in [10, 13]$ for the excited state and $t \in [9, 15]$ for the

ground state. This difference is due to the fact that the data for the excited states is noisier than that of the fundamental states. Also, as t approaches large values for the excited states we can observe larger error bars when compared to the ground state. This behavior is not surprising since the data for the excited states are unstable.

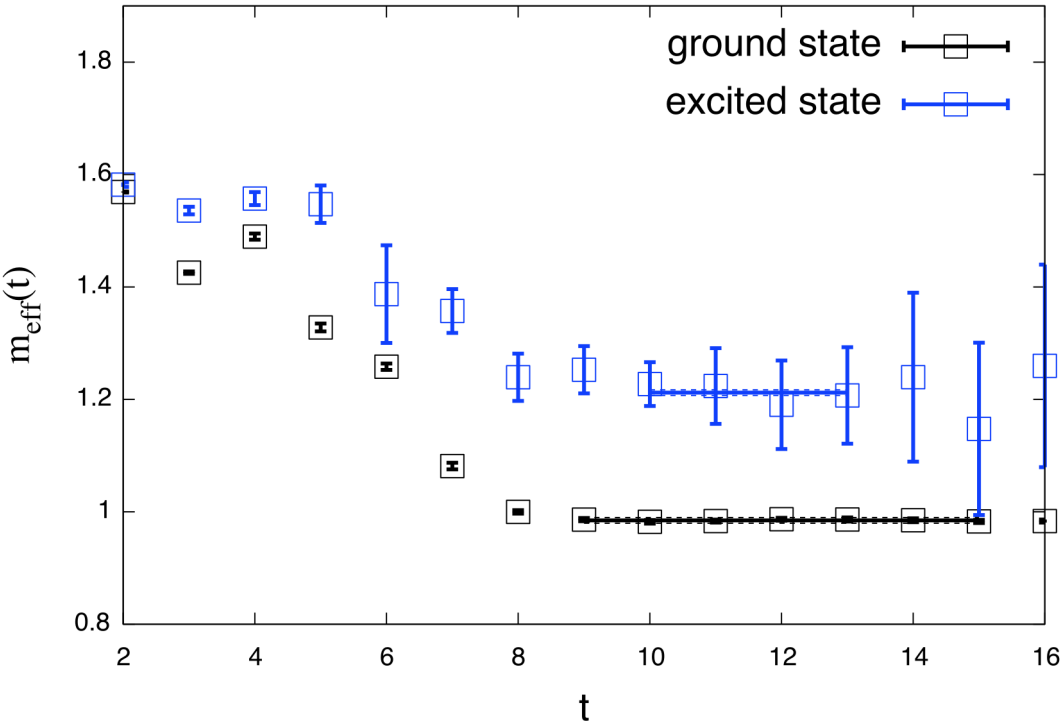

FIGURE 4.1: The effective masses of the two smallest eigenvalues from a 2×2 matrix of pseudoscalar meson correlators as a function of time. The plateau for the first excited state is clearly visible but rather shorter than the ground state plateau.

Fitting Procedure

We have discussed fits and errors in the last chapter. However, it is worth noting that the simplest fit procedure is the two parameter fit $Ae^{-m(t-t_0)}$ of the GEVP eigenvalues, where m is the mass of the observable of interest and A is a prefactor. As we already have discussed (see Section 3.7), we are using *uncorrelated fits*. This means that we perform simple two parameter fits (when we consider only the ground state) to the eigenvalues, weighing each point by its error as determined from a single-elimination jackknife procedure.

Requirements for a Good Fit

Since performing a good fit is not an easy task, we need to take into account some points:

- We should perform a stable fit in the time range of the plateau region. In particular, the fit should be stable with respect to small changes in the minimum timeslice included in the fit;

- We need to include in the fit a reasonable range in time t. This number of points will depend on the size of our lattice;
- One should aim at *reasonable* statistical errors on the fitted quantity (mass, decay constants, form factors, etc);
- The χ^2, for a good fit, is normally of order one (for *uncorrelated* data) when this quantity can be reliably determined.

4.4.1 Computational Tools

LAPACK

We have used the LAPACK library, written in Fortan 90, which provides routines for solving systems of simultaneous linear equations, least-square solutions of linear systems of equations, eigenvalue problems, and singular value problems. One of this routines is called **DGGEV**, which computes for a $N \times N$ real non-symmetric matrix A, the eigenvalues and, optionally, the left and/or right eigenvectors. For more information and examples about LAPACK and the DGGEV routine, see `http://www.netlib.org/lapack/`.

MINUIT

To perform our fits, we have used *MINUIT - Function Minimization and Error Analysis* [109]. It is a tool to find the local minimum of a multi-parameter function and analyze the shape of the function around the minimum. This tool works with χ^2 or log-likelihood functions, to compute the best values of our fit, including uncertainties. It is especially suited to handle difficult problems, including those which may require guidance in order to find the correct solution. This package acts on a multiparameter Fortran function to which we give the generic name *FCN*. The value of FCN normally depends on some variable parameters whose meaning is defined by the user (or by the intermediate program), but whose trial values are determined by Minuit according to the user purposes (usually minimize it).

4.5 Summary

In this chapter we described the methods used for excited state hadron spectroscopy and, in particular, the GEVP. We discussed also the extraction of the mass and matrix elements. Moreover, we commented on the fitting procedure and the error analysis.

Chapter 5

Charmonium on the Lattice

The interest in charmonium spectroscopy has increased in the last decade due to the experimental observations (at $B-$ factories, CLEO-c, the Tevatron and BES) of rather narrow states close to or above open-charm thresholds. An extensive review of the experimental and theoretical situation is given in [5]. We will explore charmonium physics in Section 5.1 and the setup of our study in Section 5.2 which allows to study ground states and first radial excited states. Performing a precision calculation of the masses of the lower-lying states is an important benchmark of lattice computations (some examples of recent studies are found in [110–112]). Currently, huge progress has been made using LQCD to investigate excited states (see [113–115]).

5.1 Physics of Interest

Charmonium physics is a challenging and promising topic for lattice QCD simulations, since we have accurate experimental results that can help checking the reliability of our calculations, provided that all systematic errors are under control. In this section, we will discuss the states we have been working on.

The charmonium was discovered in the 70's, when the SLAC and Brookhaven collaborations announced almost simultaneously the observation of a new narrow resonance which would be, afterwards named J/ψ [116, 117]. Shortly after, another narrow state was discovered by the SLAC group, which was called $\psi(2S)$ [118]. These two resonances were interpreted as bound states of a new quark, at that moment called charm or c quark, and its antiquark $\bar{c}$. The charmonium $(c\bar{c})$ states are a powerful tool to understand strong interactions. The mass of the quark is large ($m_c \approx 1.5$GeV), which makes it possible to attempt a phenomenological description of the dynamical properties of the charmonium system using, for example, non-relativistic potential models [119–121], where the asymptotic properties of the strong interaction are reproduced by choosing a specific functional form.

Currently, charmonium physics has been receiving attention again, because of the discovery of new states such as $\eta_c(2S)$, $X(3872)$ (discovered, respectively, by the Belle Collaboration [122] and by the BaBar Collaboration [123]), of the exploitation of the B factories as rich sources of charmonium states and of new projects like CLEO-c.

Remarks on Charmonium

Experimental charmonium breakthroughs have been done mostly at e^+e^- colliding facilities such as BES at BEPC, CLEO at CESR, BaBaR at PEP-II, Belle at KEKB, KEDR at VEPP-4M. Other collaborations have also provided data like E835 at Fermilab ($p\bar{p}$ gas-jet target) and CDF at the Tevratron $p\bar{p}$ collider. For Refs. see [124–128].

In e^+e^- experiments, annihilation occurs primarly through an intermediate virtual photon, creating the bound state $c\bar{c}$, as shown in Fig. 5.1. There are other mechanisms to produce the charmonium states including photon-photon fusion and initial state radiation. Moreover, the production of double charmonium in e^+e^- has been observed at the B factories. All this mechanisms are well described in [129] and represented in Fig. 5.1. A detailed overview on charmonium physics can be found in [113, 130–132].

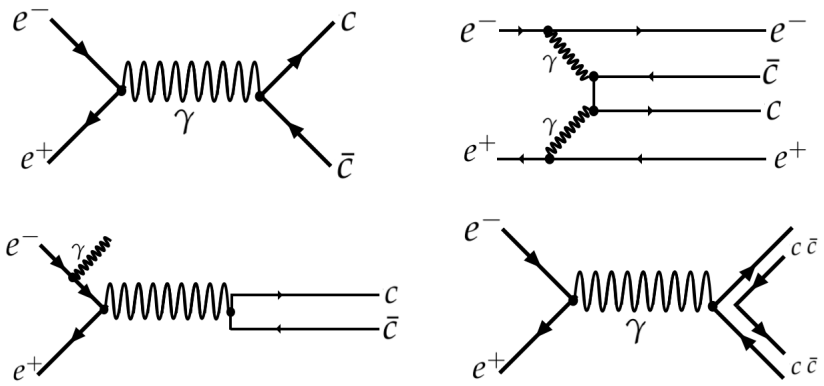

FIGURE 5.1: The Feynman diagrams of the process $e^+e^- \to c\bar{c}$ (top left hand side), $\gamma\gamma$ fusion process (top right hand side), initial state radiation production of charmonium (bottom left hand side) and double charmonium production in e^+e^- annihilation (bottom right hand side).

Radial Excitations

In this work, we shall study the first radial excitation of charmonium states (see Section 5.1.1). The radial excitations present the same spin-parity as the ground state and many radial excitations of mesons and baryons have been experimentally discovered [1].

A mesonic system can be classified as

$$|n^{2s+1}L_J\rangle \tag{5.1}$$

where n stands for the radial quantum number, s the total spin of the meson, L the orbital angular momentum and J the total angular momentum ($\vec{J} = \vec{L} + \vec{s}$). Equation (5.1) is called *spin-orbit* decomposition. For a value of $L \neq 0$, the states are orbitally excited. We are interested in $L = 0$, but with $n > 0$, which means we have radial excitations. Then, for the ground state we have $1S(n = 1, L = 0)$ and for the first excited state $2S(n = 2, L = 0)$. In this work, we consider the two singlet states (spin 0): η_c and $\eta_c(2S)$, as well as the two triplet states (spin

1): J/ψ and $\psi(2S)$. In the next section, we will address the excited states which will be the object of our study.

5.1.1 Charmonium States

We will begin by a brief description of the states we considered.

Pseudoscalar Mesons

- $\eta_c(1S)$ (ground state): quantum numbers$J^{PC} = 0^{-+}$ and mass [1]

$$m_{\eta_c(1S)} = 2983.9 \pm 0.5 \text{ MeV}$$

The first measurements of the mass and width of the low-lying charmonium state, the η_c, presented large uncertainties when compared to those of the other charmonium states [133]. In the beginning, these measurements were made through properties using J/ψ radiative transitions [134] . There is a 3.3σ inconsistency in previous η_c mass measurements from J/ψ and $\psi' \to \gamma\eta_c$ (averaging 2977.3 ± 1.3 MeV) compared to $\gamma\gamma$ or $p\bar{p}$ production (averaging 2982.6 ± 1.0 MeV) [135]. However, some modern experiments, which include photon-photon fusion and B decays, have reported a much higher mass and much wider width [136–138]. One of the advantages of performing experiments with $\gamma\gamma$ fusion is, for example, a negligible background [139]. Currently, the most accurate result was measured by BESIII, where the η_c was reconstructed through six modes: $K_S K^+\pi^-$, $K^+K^-\pi^0$, $\eta\pi^+\pi^-$, $K_S K^+\pi^+\pi^-\pi^-$, $K^+K^-\pi^+\pi^-\pi^0$, and $3(\pi^+\pi^-)$, in which the K_S is reconstructed in $\pi^+\pi^-$ mode, and the η and π^0 from $\gamma\gamma$ final states [140, 141]. Then, the results for the mass and the width of η_c [1] are, respectively,

$$m_{\eta_c(1S)} = 2984.3 \pm 0.5 \text{ MeV}$$

and

$$\Gamma = 32.0 \pm 0.8 \text{ MeV}$$

These results agree with certain recent lattice computations [142].

- $\eta_c(2S)$ (first excited state): quantum numbers $J^{PC} = 0^{-+}$ and mass [1]

$$m_{\eta_c(2S)} = 3637.6 \pm 1.2 \text{ MeV}$$

and

$$\Gamma = 11.3^{+3.2}_{-2.9} \text{ MeV}$$

It is the first radial excitation of η_c ($n = 2$). In 2002, the Crystal Ball experiment found one candidate to be the $\eta_c(2S)$ at a mass of 3596 ± 5 MeV$/c^2$ [131]. In addition, in 2002, the Belle experiment observed clear peaks in the X mass distribution in $B \to KX, X \to$

$K_S K^{\pm}\pi^{\mp}$ at the η_c, the J/ψ, and at a mass of 3654 ± 10 MeV$/c^2$ [143]. CLEO [137] and BaBaR [136] confirmed the higher mass value in $\gamma\gamma \to K_S K^{\pm}\pi^{\mp}$ with mass measurements of 3642 MeV$/c^2$ and 3633 MeV$/c^2$, respectively. Most recently, the Belle Collaboration performed new measurements for $\eta_c(1S)$ and $\eta_c(2S)$ resonant parameters in the decay of $B^{\pm} \to K^{\pm}(K_S K\pi)^0$ by considering the interface between $\eta_c(1S)/\eta_c(2S)$. At the same time, the BaBaR Collaboration also updated the analysis of $e^+e^-(\gamma\gamma), \gamma\gamma \to \eta_c(1S)/\eta_c(2S) \to (K_S K\pi)^0$ and $K^+K^-\pi^+\pi^-\pi^0$ modes [144]. The BESIII Collaboration [145, 146] searched for the transition $\psi' \to \gamma\eta_c(2S)$ through the hadronic final states $K_S K^{\pm}\pi^{\mp}$. They have measured the mass for $\eta_c(2S)$ which is $3638.5 \pm 2.3 \pm 1.0$ MeV. These investigations indicate that the $\eta_c(2S)$ parameters agree well from different production processes [133]. The higher mass value is more consistent with lattice calculations and phenomenological models [147].

Vector Mesons

- $J/\psi(1S)$ (ground state): quantum numbers $J^{PC} = 1^{--}$ and mass [1]

$$m_{J/\psi(1S)} = 3096.900 \pm 0.006 \ \text{MeV}$$

and

$$\Gamma = 92.9 \pm 2.8 \ \text{keV}$$

The J/ψ was discovered simultaneously in two different laboratories with two completely different types of machine. This detection was really important, because these two groups had found a new particle whose lifetime was about a thousand times longer than that of other particles of comparable mass. This discovery had such a huge repercussion that it became known as the *November revolution* in the physics community. However, it was only later that it was understood that this new particle was a $c\bar{c}$ bound state. Remarkably, it was shown that the $c\bar{c}$ spectrum can be well understood within the framework of non-relativistic quantum mechanics plus spin dependent corrections.

- $\psi(2S)$ (first excited state): quantum numbers $J^{PC} = 1^{--}$ and mass [1]

$$m_{\psi(2S)} = 3686.097 \pm 0.025 \ \text{MeV}$$

and

$$\Gamma = 589.188 \pm 0.028 \ \text{MeV}$$

The discovery of the meson $\psi(2S)$ occured almost at the same time as the J/ψ discovery. While the different collaborations were trying to figure out informations about J/ψ, the SPEAR group discovered three more states through radiative transitions which included the $\psi(2S)$ [148].

5.2 Charmonium Spectroscopy

In this section, we describe our setup for the extraction of the $c\bar{c}$ spectroscopy from two-point correlation functions and the GEVP method. The charmonium spectroscopy below the open charm threshold has been well measured and agrees with the theoretical expectations. However, adequate experimental information is still lacking, as well as solid theoretical inferences for those charmonium states. We will discuss more about the charmonium spectrum in the following section.

5.2.1 The Charmonium Spectrum

Figure 5.2 shows the charmonium spectrum. The spectrum consists of eight narrow states below the threshold for open charm ($\approx$ 3730 MeV) and several states above threshold, some of them wide, since they decay to $D\bar{D}$. In addition, certain states are narrow, because their decay to open charm is not allowed by conservation laws. Below threshold all states are well established. On the other hand, we do not have much information on the states above the threshold. Even though the states below the threshold have been identified, we still do not have all the necessary information about them. Therefore, in this work, we aim at providing more information about some of these states.

In 2008, a pioneering study on excited charmonium states using LQCD was published [111]. In this study the variational method, explained in the previous chapter was used. Considering the $J^{PC} = 1^{--}$ channel, where the J/ψ is the ground state and has a very clean signal, investigations have found six states, but only three of them were identified, namely J/ψ, $\psi(2S)$ and $\psi(3S)$. The lattice values found were higher than the experimental ones and the discrepancies in masses ranged from 12 to 82 MeV [112]. These results are pioneering, as we said before, but more investigation is needed; moreover open charm states were ignored. Nowadays, lattice collaborations[1] generate a large number of ensembles with different values of lattice spacings, which opens the way to further improvements in lattice calculations.

5.2.2 Variational Method

In our analysis [149, 150], we want to extract information on the charmonium ground state and the charmonium first excited state. We then need to find the best way to apply the GEVP in order to obtain reliable results.

GEVP discussion

We already presented the GEVP in Section 4.3 and in Appendix B. Here, we will apply this procedure to the charmonium states of interest.

[1] For example: MILC and ALPHA collaborations.

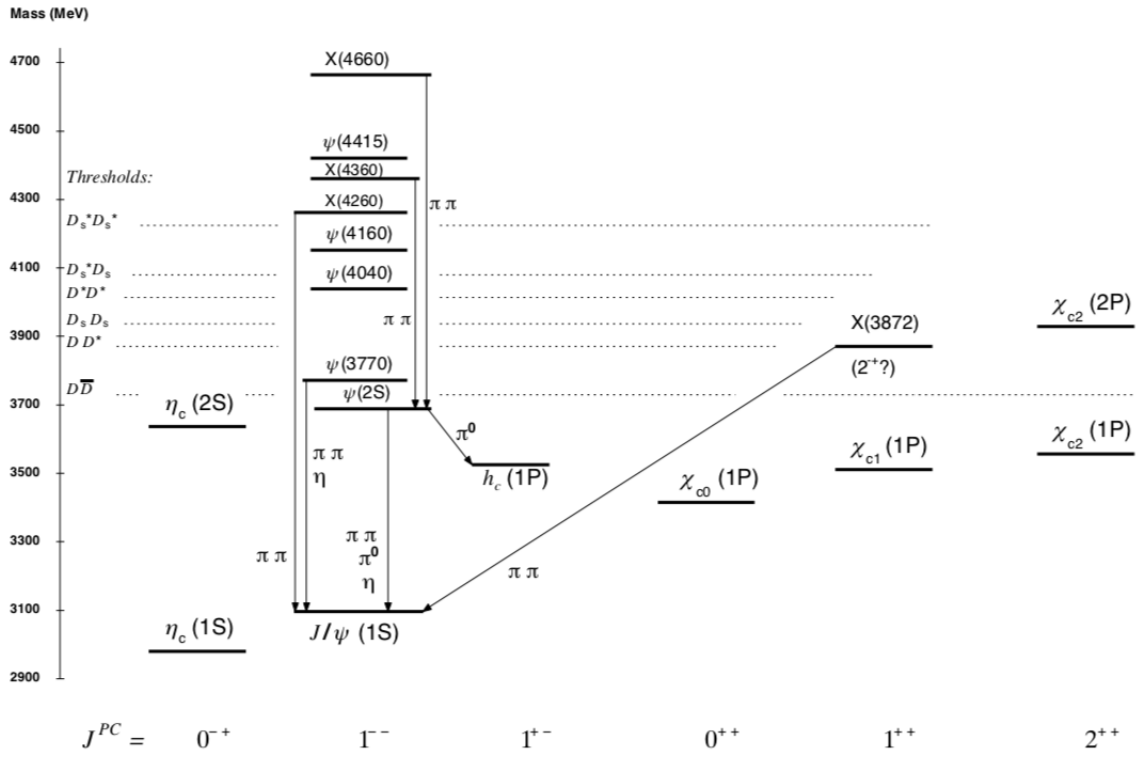

FIGURE 5.2: The level scheme of the $c\bar{c}$ states showing experimentally established states with solid lines. From [1].

The two-point correlation functions under investigation read

$$\begin{aligned} C(t) &= \sum_{\vec{x},\vec{y}} \langle \Omega | [\mathcal{O}_1](\vec{y},t)[\mathcal{O}_2^\dagger](\vec{x},0) | \Omega \rangle \\ &= \sum_{\vec{x},\vec{y}} \langle \Omega | [\bar{c}\Gamma c](\vec{y},t)[\bar{c}\gamma_0\Gamma'\gamma_0 c](\vec{x},0) | \Omega \rangle \end{aligned} \tag{5.2}$$

where $\langle \cdot \rangle$ stands for the expectation value over gauge configurations, and the interpolating fields $\mathcal{O}_{1(2)}$ can be local or non-local. As we already discussed in Section 4.3, we need to find a good basis of interpolating fields. Therefore, as a preparatory work, we have explored different possibilities to find the best operator basis, combining levels of Gaussian smearing, interpolating fields with a covariant derivative $\bar{c}\Gamma(\vec{\gamma}\cdot\vec{\nabla})c$ and operators that are odd under time parity. Solving the GEVP is a key point in this analysis. In the literature, we have noticed that some groups [151–153] tried to mix together two types of operators in a unique GEVP system: $\bar{c}\Gamma c$ and $\bar{c}\gamma_0\Gamma c$. According to our investigations, this approach raises some questions. Indeed, let us consider the example of the pseudoscalar and axial interpolating fields, respectively,

$$P = \bar{c}\gamma_5 c \tag{5.3}$$

$$A_0 = \bar{c}\gamma_0\gamma_5 c \tag{5.4}$$

The asymptotic behaviour of the two-point correlation functions defined with these interpolating fields are

$$\langle P(t)P(0)\rangle\,;\langle A_0(t)A_0(0)\rangle \xrightarrow{t\to\infty} \cosh[m_P(T/2-t)] \tag{5.5}$$

$$\langle P(t)A(0)\rangle\,;\langle A_0(t)P(0)\rangle \xrightarrow{t\to\infty} \sinh[m_P(T/2-t)] \tag{5.6}$$

In eq. (5.5) we used the symmetry of the correlation function with respect to $t \leftrightarrow T-t$ of the periodic lattice. Here, both quarks can propagate forward and backward in time due to periodic boundary conditions resulting in the hyperbolic cosine function instead of the exponential. However, in eq. (5.6) we have antisymmetrical correlators with respect to the transformation $t \leftrightarrow T-t$, which results in the hyperbolic sine (for details see Appendix B).

For the GEVP, the 2×2 matrix of correlators is then

$$C(t) = \begin{bmatrix} \langle P(t)P(0)\rangle & \langle A_0(t)P(0)\rangle \\ \langle P(t)A_0(0)\rangle & \langle A_0(t)A_0(0)\rangle \end{bmatrix} \tag{5.7}$$

where C_{ij} is the $i-j$ matrix element of $C(t)$ written as

$$C_{ij}(t) = \sum_n Z_n^i Z_n^{*j}[D_{ij}\rho_n^{(1)}(t) + (1-D_{ij})\rho_n^{(2)}(t)] \quad , \quad (D_{ij}=0 \text{ or } 1) \tag{5.8}$$

where Z_n^i is the overlap factor associated with the interpolating operator. Moreover,

$$\rho^{(1),(2)}(t) \sim e^{-m_P t}\cosh[m_P(T/2-t)] \quad \text{or} \quad e^{-m_P t}\sinh[m_P(T/2-t)] \tag{5.9}$$

where m_P is the mass of the pseudoscalar state. The choice of $\rho^{(1)}$ and $\rho^{(2)}$ will depend on the correlator we are using. In the following we will present the asymptotic behavior for the different correlators.

Let us repeat the GEVP construction (cf. Appendix B). The dual vector to Z, u_n, is defined by

$$\sum_j Z_m^{*j} u_n^j = \delta_{mn} \tag{5.10}$$

Inserting the above equation in the GEVP, we arrive at

$$\begin{aligned} \sum_j C_{ij}(t)u_n^j &= \sum_{j,m} Z_m^i Z_m^{*j} u_n^j \left[D_{ij}\rho_m^{(1)}(t) + (1-D_{ij})\rho_m^{(2)}(t)\right] \\ &= \sum_m \rho_m^{(2)}(t) Z_m^i \sum_j Z_m^{*j} u_n^j + \sum_m \left(\rho_m^{(1)}(t) - \rho_m^{(2)}(t)\right) Z_m^i \sum_j D_{ij} Z_m^{*j} u_n^j \\ &= \rho_n^{(2)}(t) Z_n^i + \sum_m \left(\rho_m^{(1)}(t) - \rho_m^{(2)}(t)\right) Z_m^i \sum_j D_{ij} Z_m^{*j} u_n^j \end{aligned} \tag{5.11}$$

If the D_{ij} do not depend on i, j, we obtain the following structure

$$C(t)u_n = \rho_n(t)Z_n \quad \text{and} \quad \lambda_n(t,t_0) = \frac{\rho_n(t)}{\rho_n(t_0)} \tag{5.12}$$

where $\lambda_n(t, t_0)$ are the eigenvalues of the GEVP.

Operator Mixing

The mixing of T-odd and T-even operators [151–153] in a single GEVP system represents an issue, since the D's depend on i and j, which means it is not possible to use eq. (5.12). For this reason, approximating every correlator by sums of exponentials forward in time, together with the assumption that the D_{ij} do not depend on i and j, is problematic. In order to understand this issue, we constructed a toy model with three states in the spectrum:

spectrum	Matrix of couplings	time behavior of C_{ij}
1.0	$\begin{bmatrix} 0.6 & 0.25 & 0.08 \\ 0.61 & 0.27 & 0.08 \\ 0.58 & 0.24 & 0.08 \end{bmatrix}$	$\begin{bmatrix} \cosh & \sinh & \cosh \\ \sinh & \cosh & \sinh \\ \cosh & \sinh & \cosh \end{bmatrix}$
1.25		
1.44		

To extract the effective mass of the toy model we have used eq. (4.26). In our numerical application, we have choosen $T = 64$, $t_0 = 3$ and compared 2×2 and 3×3 subsystems: the results can be seen in Fig. 5.3. On the left side of Fig. 5.3 we have two different values of the effective mass, the black points are the results for the lower energy value of the spectrum, while the red dots are for the second value presented in the spectrum. On the right side of Fig. 5.3, in addition to the previously presented values, we also exhibit the value for the highest energy in the spectrum (green points).

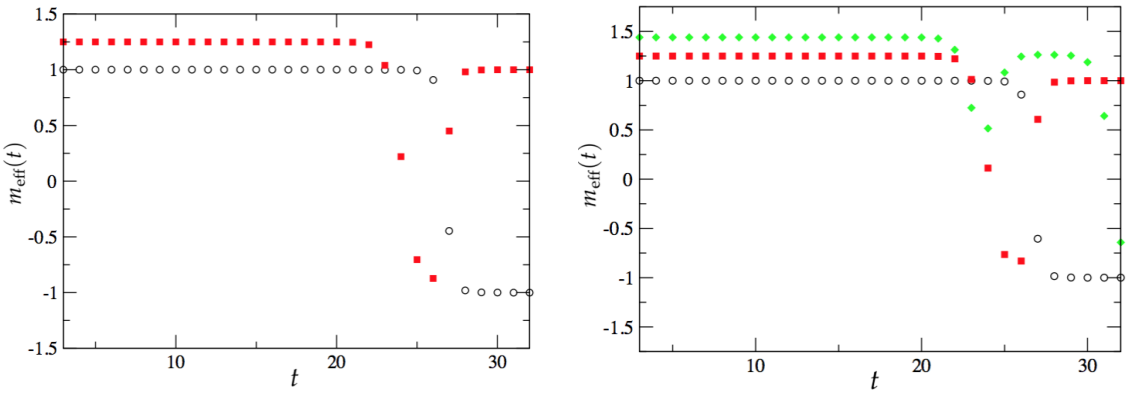

FIGURE 5.3: Effective masses obtained from the 2×2 subsystem (left panel) and the 3×3 subsystem (right panel) of our toy model, with $T = 64$ and $t_0 = 3$.

We can observe that until $t \approx T/4$, neglecting the time-backward contribution in the correlation function has no effect. Based on this study, we can affirm that the method is reliable for the ground state and the first excited state. However, one may wonder what could happen with a dense spectrum when the energy of the third or a higher excited state is extracted. For this case, there will be a competition between the contamination from higher states, which are not properly isolated by the finite GEVP system, and the omission of the backward in time contribution to the generalized eigenvalue under study [101].

Interpolating Field Basis

The construction of a basis of interpolating fields from

$$\{\bar{c}\Gamma c; \bar{c}\Gamma(\vec{\gamma}\cdot\vec{\nabla})c\} \tag{5.13}$$

where the symmetric covariant derivative has the form presented in Chapter 2,

$$\nabla_\mu\psi(x) = \frac{U_\mu(x)\psi(x+a\hat{\mu}) - U^\dagger_\mu(x-a\hat{\mu})\psi(x-a\hat{\mu})}{2a} \tag{5.14}$$

has some advantages, which have been already explored in [154, 155]. However, we have found some weak points in this choice of operators. As an example, we will take the pseudoscalar-pseudoscalar correlator defined by

$$C_{ij}(t) = \sum_{ij}\langle\Omega|[\bar{c}\gamma_5\gamma_i D_i c](t)\,[\bar{c}\gamma_5\gamma_j D_j c](0)|\Omega\rangle \tag{5.15}$$

where D_i is the derivative in the i direction. The behavior of this equation will be studied with a naïve quark model. The full discussion is found in Appendix C. By studying the operator $\bar{c}\gamma_5\gamma_i D_i c$ in eq. (5.15) we arrive at

$$\sum_i \bar{c}\gamma_5\gamma_i D_i c = 0 \tag{5.16}$$

From eq. (5.16), we can conclude that $\bar{c}\gamma_5\gamma_i D_i c$ contribution in (5.15) should be nonexistant. However, if one chooses

$$C_{ij}(t) = \sum_{ij}\langle\Omega|[\bar{c}\gamma_0\gamma_5\gamma_i D_i c](t)\,[\bar{c}\gamma_0\gamma_5\gamma_j D_j c](0)|\Omega\rangle \tag{5.17}$$

we get the following contribution from the operator $\bar{c}\gamma_0\gamma_5\gamma_i D_i c$,

$$\sum_i \bar{c}\gamma_0\gamma_5\gamma_i D_i c = -c_1^T\frac{\vec{p}^2}{m_c}\sigma_2 c_1 \quad \text{where} \quad c_1 = \begin{pmatrix} c_1^+ \\ c_1^- \end{pmatrix} \tag{5.18}$$

which is clearly a non-zero contribution. The correlator (5.17) has a very good signal, especially when compared to (5.15). We can observe that the simple fact of inserting a γ_0 matrix can change extremely the correlator behaviour.

Our Choice of Operators

In our simulations, we have considered four Gaussian smearing levels for the quark field c (including no smearing) to built our 4×4 matrix of correlators without any covariant derivative

or operator of the kind π_2 ($\gamma_0\gamma_5$) or ρ_2 ($\gamma_i\gamma_0$) [154], from which we have extracted the $\mathcal{O}(a)$ improved hadronic quantities we have investigated. By solving the GEVP for the pseudoscalar-pseudoscalar and vector-vector matrix of correlators, respectively,

$$C_{PP}(t)v_n^P(t,t_0) = \lambda_n^P(t,t_0)v_n^P(t,t_0)C_{PP}(t_0) \tag{5.19}$$

and

$$C_{VV}(t)v_n^V(t,t_0) = \lambda_n^V(t,t_0)v_n^V(t,t_0)C_{VV}(t_0) \tag{5.20}$$

we obtained the correlators which have the largest overlap with the n^{th} excited state as follows:

$$\tilde{C}^n_{A_0P}(t) = \sum_i C_{A_0^L P^{(i)}}(t)v_n^{P,i}(t,t_0) \tag{5.21}$$

$$\tilde{C}^n_{PP}(t) = \sum_i C_{P^L P^{(i)}}(t)v_n^{P,i}(t,t_0) \tag{5.22}$$

$$\tilde{C}'^n_{PP}(t) = \sum_{i,j} v_n^{P,i}(t,t_0)C_{P^{(i)}P^{(j)}}(t)v_n^{P,j}(t,t_0) \tag{5.23}$$

$$\tilde{C}^n_{VV}(t) = \frac{1}{3}\sum_{i,k} C_{V_k^L V_k^{(i)}}(t)v_n^{V,i}(t,t_0) \tag{5.24}$$

$$\tilde{C}'^n_{VV}(t) = \frac{1}{3}\sum_{i,j,k} v_1^{V,i}(t,t_0)C_{V_k^{(i)}V_k^{(j)}}(t)v_n^{V,j}(t,t_0) \tag{5.25}$$

$$\tilde{C}^n_{TV}(t) = \frac{1}{3}\sum_{i,k} C_{T_{k0}^L V_k^{(i)}}(t)v_n^{V,i}(t,t_0) \tag{5.26}$$

$$\tilde{C}^n_{\delta PP}(t) = \frac{\tilde{C}^n_{PP}(t+1) - \tilde{C}^n_{PP}(t-1)}{2a} \tag{5.27}$$

$$\tilde{C}^n_{\delta TV}(t) = \frac{\tilde{C}^n_{TV}(t+1) - \tilde{C}^n_{TV}(t-1)}{2a} \tag{5.28}$$

and their symmetric counterpart with the exchange of operators at the source and at the sink. The quark bilinears which appear in the previous equations are:

$$P = \bar{c}\gamma_5 c \tag{5.29}$$

$$A_0 = \bar{c}\gamma_0\gamma_5 c \tag{5.30}$$

$$V_k = \bar{c}\gamma_k c \tag{5.31}$$

$$T_{k0} = \bar{c}\gamma_k\gamma_0 c \tag{5.32}$$

Moreover, in these expressions, the label L stands for a local interpolating field and, in addition, we have a sum over i and j running over the four Gaussian smearing levels. The

projected correlators have the following asymptotic behaviour

$$\tilde{C}'^{n}_{PP}(t) \xrightarrow[t/a\gg 1]{} \frac{\mathcal{Z}'_{PP_n}}{am_{P_n}} e^{-m_{P_n}T/2}\cosh[m_{P_n}(T/2-t)] \tag{5.33}$$

$$\tilde{C}^{n}_{A_0P}(t) \xrightarrow[t/a\gg 1]{} -\frac{\mathcal{Z}_{AP_n}}{am_{P_n}} e^{-m_{P_n}T/2}\sinh[m_{P_n}(T/2-t)] \tag{5.34}$$

$$\tilde{C}^{n}_{PP}(t) \xrightarrow[t/a\gg 1]{} \frac{\mathcal{Z}_{PP_n}}{am_{P_n}} e^{-m_{P_n}T/2}\cosh[m_{P_n}(T/2-t)] \tag{5.35}$$

$$\tilde{C}'^{n}_{VV}(t) \xrightarrow[t/a\gg 1]{} \frac{\mathcal{Z}'_{VV_n}}{am_{V_n}} e^{-m_{V_n}T/2}\cosh[m_{V_n}(T/2-t)] \tag{5.36}$$

$$\tilde{C}^{n}_{VV}(t) \xrightarrow[t/a\gg 1]{} \frac{\mathcal{Z}_{VV_n}}{am_{V_n}} e^{-m_{V_n}T/2}\cosh[m_{V_n}(T/2-t)] \tag{5.37}$$

$$\tilde{C}^{n}_{TV}(t) \xrightarrow[t/a\gg 1]{} \frac{\mathcal{Z}_{TV_n}}{am_{V_n}} e^{-m_{V_n}T/2}\sinh[m_{V_n}(T/2-t)] \tag{5.38}$$

$$\tilde{C}^{n}_{\delta PP}(t) \xrightarrow[t/a\gg 1]{} -1/a\ \sinh(am_{P_n})\frac{\mathcal{Z}_{PP_n}}{am_{P_n}} e^{-m_{P_n}T/2}\sinh[m_{P_n}(T/2-t)] \tag{5.39}$$

$$\tilde{C}^{n}_{\delta TV}(t) \xrightarrow[t/a\gg 1]{} -1/a\ \sinh(am_{V_n})\frac{\mathcal{Z}_{TV_n}}{am_{V_n}} e^{-m_{V_n}T/2}\cosh[m_{V_n}(T/2-t)] \tag{5.40}$$

where the various $\mathcal{Z}$ stands for the meson-to-vacuum matrix elements of the operators in the respective channels, which arise in the spectral decompostions of the correlation functions.

Decay Constant Extraction

We will start by considering the $\mathcal{O}(a)$ improved operators (A_0^I and V_k^I), in order to minimize discretization effects [156],

$$A_0^I = (1+b_A Z a m_c^{\mathrm{AWI}})\left(A_0 + a c_A \frac{\partial_0+\partial_0^*}{2}P\right) \tag{5.41}$$

$$V_k^I = (1+b_V Z a m_c^{\mathrm{AWI}})\left(V_k + a c_V \frac{\partial_\nu+\partial_\nu^*}{2}T_{k\nu}\right) \tag{5.42}$$

where the coefficient Z is defined in Refs. [67, 157]. The lattice derivatives are given by

$$\partial_\nu F(x) = \frac{F(x+a\hat{\nu})-F(x)}{a} \tag{5.43}$$

$$\partial_\nu^* F(x) = \frac{F(x)-F(x-a\hat{\nu})}{a} \tag{5.44}$$

We have also used non-perturbative results and perturbative formulae from [158–160] for the improved coefficients (b_A, b_V, c_A and c_V). The non-perturbative renormalization of the axial (Z_A) and vector current (Z_V) is discussed in the next chapter. We have defined the quark mass

m_c via the axial Ward Identity (AWI)

$$m_c^{\mathrm{AWI}} = \frac{\frac{\partial_0+\partial_0^*}{2} C_{A_0^L P^L}(t) + a c_A \partial_0 \partial_0^* C_{P^L P^L}(t)}{2 C_{P^L P^L}(t)} \tag{5.45}$$

The expression (5.45) exhibits an extended plateau over the timeslices sufficiently far from the boundaries of the lattice and therefore can be accurately determined with confidence as the plateau average over central timeslices. In eq. (5.45), ∂_0 and ∂_0^* denote the forward and backward difference operators in time direction. The improvement coefficient c_A has been determined non-perturbatively [158]. The counterpart of eq. (5.45) is defined through the vector Ward Identity (VWI)

$$am_c^{\mathrm{VWI}} = \frac{1}{2}\left(\frac{1}{\kappa_c} - \frac{1}{\kappa_{\mathrm{crit}}}\right) \tag{5.46}$$

where κ_c stands for the value of the hopping parameter of the charm quark. The κ_{crit} parameter is required because Wilson fermions break chiral symmetry (see Section 2.4.3). The value of κ_{crit} is chosen to give a zero pion mass [27].

The lattice expressions for the pseudoscalar and vector matrix elements of the renormalized axial and vector current, which are proportional to the leptonic pseudoscalar and vector meson decay constant of interest, can be split into leading and $\mathcal{O}(a)$ improvement contributions as shown in the following.

Ground State

Pseudoscalar case: the f_{η_c} decay constant is extracted in the following way:

$$\begin{cases} \langle 0|A_0^R|\eta_c(\vec{p}=0)\rangle = -f_{\eta_c} m_{\eta_c} = -Z_A(1+b_A Z a m_c^{\mathrm{AWI}}) m_{\eta_c} f_{P_c}^0 (1 + f_{P_c}^1/f_{P_c}^0) \\ a f_{P_c}^0 = \dfrac{1}{a m_{\eta_c}} \dfrac{\mathcal{Z}_{AP_1}}{\sqrt{\mathcal{Z}'_{PP_1}}} \quad ; \quad a f_{P_c}^1 = \dfrac{1}{a m_{\eta_c}} c_A \sinh(a m_{\eta_c}) \dfrac{\mathcal{Z}_{PP_1}}{\sqrt{\mathcal{Z}'_{PP_1}}} \end{cases} \tag{5.47}$$

Vector case: the $f_{J/\psi}$ decay constant is obtained with

$$\begin{cases} \langle 0|V_i^R|J/\psi(\epsilon,\vec{p}=0)\rangle = \epsilon_i f_{J/\psi} m_{J/\psi} = \epsilon_i Z_V(1+b_V Z a m_c^{\mathrm{AWI}}) m_{J/\psi} f_{V_c}^0 (1 + f_{V_c}^1/f_{V_c}^0) \\ a f_{V_c}^0 = \dfrac{1}{a m_{J/\psi}} \dfrac{\mathcal{Z}_{VV_1}}{\sqrt{\mathcal{Z}'_{VV_1}}} \quad ; \quad a f_{V_c}^1 = -\dfrac{1}{a m_{J/\psi}} c_V \sinh(a m_{J/\psi}) \dfrac{\mathcal{Z}_{TV_1}}{\sqrt{\mathcal{Z}'_{VV_1}}} \end{cases} \tag{5.48}$$

In eqs. (5.47) and (5.48) the R superscript denotes the renormalized improved operators. The parameter ϵ is the vector current polarization (see Appendix A). The renormalization constants Z_A and Z_V have been non perturbatively measured in [99, 100]. We will address this topic later in Section 5.2.3. Moreover, in eq. (5.47) the index 1 in $\mathcal{Z}_{AP_1}$, $\mathcal{Z}'_{PP_1}$, $\mathcal{Z}_{PP_1}$ and $\mathcal{Z}'_{PP_1}$ stands for the ground state. The same is true for eq. (5.48). The pseudoscalar (vector) decay constants $af_{P_c}^0 (af_{V_c}^0)$ and $af_{P_c}^1 (af_{V_c}^1)$ are related, respectively, to leading (index 0) and to the $\mathcal{O}(a)$ improved (index 1) contributions.

Excited State

Pseudoscalar case: in order to extract the $f_{\eta_c(2S)}$ decay constant we do

$$\begin{cases} \langle 0|A_0^R|\eta_c(2S)(\vec{p}=0)\rangle = -f_{\eta_c(2S)}m_{\eta_c(2S)} = -Z_A(1+b_A Z a m_c^{\mathrm{AWI}})m_{\eta_c(2S)}f^0_{P_c'}(1+f^1_{P_c'}/f^0_{P_c'}) \\ af^0_{P_c'} = \dfrac{1}{am_{\eta_c(2S)}}\dfrac{\mathcal{Z}_{AP_2}}{\sqrt{\mathcal{Z}'_{PP_2}}} \quad ; \quad af^1_{P_c'} = \dfrac{1}{am_{\eta_c(2S)}}c_A\sinh(am_{\eta_c(2S)})\dfrac{\mathcal{Z}_{PP_2}}{\sqrt{\mathcal{Z}'_{PP_2}}} \end{cases} \tag{5.49}$$

Vector case: the $f_{\psi(2S)}$ decay constant is is obtained through

$$\begin{cases} \langle 0|V_i^R|\psi(2S)(\epsilon,\vec{p}=0)\rangle = \epsilon_i f_{\psi(2S)}m_{\psi(2S)} = \epsilon_i Z_V(1+b_V Z a m_c^{\mathrm{AWI}})m_{\psi(2S)}f^0_{V_c'}(1+f^1_{V_c'}/f^0_{V_c'}) \\ af^0_{V_c'} = \dfrac{1}{am_{\psi(2S)}}\dfrac{\mathcal{Z}_{VV_2}}{\sqrt{\mathcal{Z}'_{VV_2}}} \quad ; \quad af^1_{V_c'} = -\dfrac{1}{am_{\psi(2S)}}c_V\sinh(am_{\psi(2S)})\dfrac{\mathcal{Z}_{TV_2}}{\sqrt{\mathcal{Z}'_{VV_2}}} \end{cases} \tag{5.50}$$

Here we are following the same ideas as for the ground state.

5.2.3 Non–perturbative renormalization: Z_A and Z_V

We would like to focus on the non-perturbative renormalization of the axial (Z_A) and vector (Z_V) current. In this work, we use the renormalization values obtained by the ALPHA collaboration [99], where they were computed non-perturbatively in the Schrödinger functional scheme [67]. In a first investigation, they calculated the values of Z_V and Z_A, derived from the Partially Conserved Axial Current (PCAC)[2] relation with non-vanishing quark mass. This condition is expected to reduce mass effects in the chiral extrapolation of the results for the normalization factors Z_V and Z_A. The ALPHA Collaboration computed $Z_A(g_0^2)$ as well as the vector current normalization factor $Z_V(g_0^2)$ for $\beta = 6/g_0^2 \geq 5.2$. The full study can be found in [100] and the values proposed by this collaboration are

$$Z_A(g_0^2) = \frac{1-0.918g_0^2+0.062g_0^4+0.020g_0^6}{1-0.8015g_0^2} \tag{5.51}$$

$$Z_V(g_0^2) = \frac{1-0.6715g_0^2+0.0388g_0^4}{1-0.5421g_0^2} \tag{5.52}$$

where they have found for Z_V an absolute error of 0.005, whereas for Z_A the absolute error decreases from 0.01 at $\beta = 5.2$ to 0.005 at $\beta = 5.7$.

In a new investigation, the ALPHA collaboration revisited their first values of Z_A and Z_V: they have discussed kinematical enhancements of cutoff effects at short and intermediate distances, having computed a new value for the normalization factor Z_A [99].

- New determination of Z_A

$$Z_A(g_0^2) = 1-0.116g_0^2+0.011g_0^4-0.072g_0^6 \tag{5.53}$$

[2] PCAC is related to the fact that the isovector axial current is conserved for a chiral theory where $m = 0$ [26].

where the coefficent of the linear term in g_0^2 is fixed by 1-loop perturbation theory and the last two coefficients are the result of a fit [99].

- Renormalization of the vector current

The ALPHA collaboration has also recalculated the renormalization constant Z_V of the vector current, but the change was less than 2% compared to the first work at the largest lattice spacing, so they kept the result presented in eq. (5.52).

Remarks on Z_A

Z_A is the finite renormalization constant of a flavor non-singlet axial bilinear of quarks. However in our work we have considered flavor-singlet operators, which should require a different renormalization constant Z'_A because of the chiral anomaly. Nevertheless, the c quark is insensitive to the chiral anomaly. Therefore, our choice of Z_A is completely acceptable.

5.3 Summary

In this chapter, we addressed the progress in theoretical and experimental physics of charmonium systems. We also presented the implementation of the GEVP method to study the spectroscopy of the charmonium states. Finally, we explored the procedure to extract the decay constants of the observables of interest as well as the non-perturbative renormalization of the axial and vector currents.

Chapter 6

Analysis and Results

In this chapter we report the results for our charmonium studies using the observables discussed in Chapter 5. We will discuss the parameters we use in lattice simulations as well as the procedure for connecting our results with the physical world. In the sequence we will compare our results with the results currently avalaible in the literature, highlighting the positives and negatives of our work. We will also present possible applications of our research in the search for New Physics.

The results discussed in this chapter are the object of [150].

6.1 Lattice Setup

This study has been performed using a subset of the CLS ensembles. These ensembles were generated with $N_f = 2$ nonperturbatively $O(a)$-improved Wilson-Clover fermions [35, 161] and the Wilson plaquette action [15] for gluon fields, by using either the DD-HMC algorithm [162–164] or the MP-HMC algorithm [165].

Numerical Implementation

In this work, we use two different ways to precondition the Hybrid Monte Carlo (HMC) for improved Wilson fermions. The first one is the domain decomposition in the DD-HMC algorithm introduced by Lüsher [162–164] and the second one is the Hasenbusch's mass preconditioning (MP) [165]. Both methods can give an acceleration of the algorithm. It is not an easy task to choose which approach is better. The performance of these methods is determined by the (auto)correlation times of the observables of interest, whose measurements require runs with high statistics. Moreover, the optimal values of the parameters and the relative performance of the algorithms could depend also on the implementation and the computer that this simulation is run on. Some comparative studies were done in [166].

Lattice Ensemble

We collect in Table 6.1 our simulation parameters. Two lattice spacings are considered:

$$a_{\beta=5.5} = 0.04831(38)\ \text{fm} \quad \text{and} \quad a_{\beta=5.3} = 0.06531(60)\ \text{fm}$$

id	β	$(L/a)^3 \times (T/a)$	κ_{sea}	a (fm)	m_π (MeV)	Lm_π	# cfgs	κ_c
E5	5.3	$32^3 \times 64$	0.13625	0.065	440	4.7	200	0.12724
F6		$48^3 \times 96$	0.13635		310	5	120	0.12713
F7		$48^3 \times 96$	0.13638		270	4.3	200	0.12713
G8		$64^3 \times 128$	0.13642		190	4.1	176	0.12710
N6	5.5	$48^3 \times 96$	0.13667	0.048	340	4	192	0.13026
O7		$64^3 \times 128$	0.13671		270	4.2	160	0.13022

TABLE 6.1: Parameters of the ensemble used: ensemble label, size of the lattice in lattice units, bare coupling $\beta = 6/g_0^2$, lattice spacing a, hopping parameter κ_{sea}, the mass of the sea pion, number of configurations employed and the charm quark hopping parameter κ_c.

The full discussion about the determination of the lattice spacings is done in Section 3.6. The sea quark masses span a range corresponding to pion masses ($190 \leq m_\pi \leq 440$) MeV, while the strange valence quark is fixed to its physical value and we scan a range of charm valence quark masses around the physical charm quark mass.

The lattice spacings a, pion masses m_π, pion decay constants f_π and values of the strange quark's hopping parameter κ_s are computed in [67], where the scale is set by computing f_K at the physical point defined by $m_\pi^{\text{phys.}} = 134.8$ MeV, $m_K^{\text{phys.}} = 494.2$ MeV and $f_K^{\text{phys.}} = 155$ MeV with QED effects removed.

The hopping parameter of the charm quark (κ_c) is fixed by requiring the D_s-meson mass to acquire its physical value, $m_{D_s} = m_{D_s}^{\text{phys.}} = 1968$ MeV, irrespective of the sea quark mass. Then, a few values in the vicinity of this meson are used and $(am_{D_s})^2$ is interpolated linearly in $1/\kappa_c$ to $(am_{D_s}^{\text{phys.}})^2$.

The data is from different Monte Carlo simulations with six different hopping parameters κ_{sea} which indicate six different pion masses (see Table 6.1). The statistical error on raw data is estimated using the jackknife procedure: two successive measurements are sufficiently separated in trajectories along the Monte-Carlo history to neglect autocorrelation effects (see Section 3.7). Inspired by the bootstrap prescription, the statistical errors on quantities extrapolated at the physical point are computed as follows. We create a large set of N_{event} fits of vectors of data whose dimension is the number of CLS ensembles used in our analysis (i.e. $n = 6$) and where each component i ($i = 1, \ldots 6$) of those vectors is filled with an element randomly chosen among the $N_{\text{bins}}(i)$ binned data per ensemble. The variance over the distribution of those N_{event} fit results, obtained with such random inputs, is then an estimator of the final statistical error. This procedure combines a blocking method to ensure that our data are not correlated with a bootstrap-inspired method. If we used the simple jackknife we could not guarantee that the data are uncorrelated. Moreover, the randomly chosen samples are large enough to determine the errors for our fitted quantities. Finally, we have computed quark propagators through two-point correlation functions using stochastic sources which are different from zero in a single timeslice that changes randomly for each measurement. We have also applied spin dilution and the one-end trick to reduce the stochastic noise (see Section 4.1) [95, 167].

6.2 Analysis

We have collected in Table D.1 of the Appendix D the raw data we have obtained in our analysis. In this section, we present the discussion made during the analysis of our data. We also present the relation used to extrapolate the values extracted from the lattice to its physical result.

Ground States

Since the fluctuations in time are large, we have decided to study the generalized eigenvectors $v_1^{P(V)}(t,t_0)$ at a fixed time $t = t_{\text{fix}}$ and at a non-fixed time $t = t_{\text{run}}$. We want to analyze and compare the behavior of the effective mass in those two situations. For the fixed time, in practice we chose $t_{\text{fix}}/a = t_0/a + 1$. In Fig. 6.1 we display our plot for $\eta_c(1S)$, where we used the eigenvectors $v_1^{P(V)}(t,t_0)$ to project correlators $C(t)$ in order to obtain the effective mass. The black points represent the effective mass varying in the range $1 \leq t_{\text{run}} \leq 48$. Due to fluctuations in the correlator, we present in the plot a reduced interval for t_{run}. The blue points stands for $t_{\text{fix}} = 4a$. We can observe that for both t_{run} and t_{fix} the effective mass remains constant taking into account the error bars. Due to the invariance in the results, we conclude that the ground state does not depend on t_{fix}.

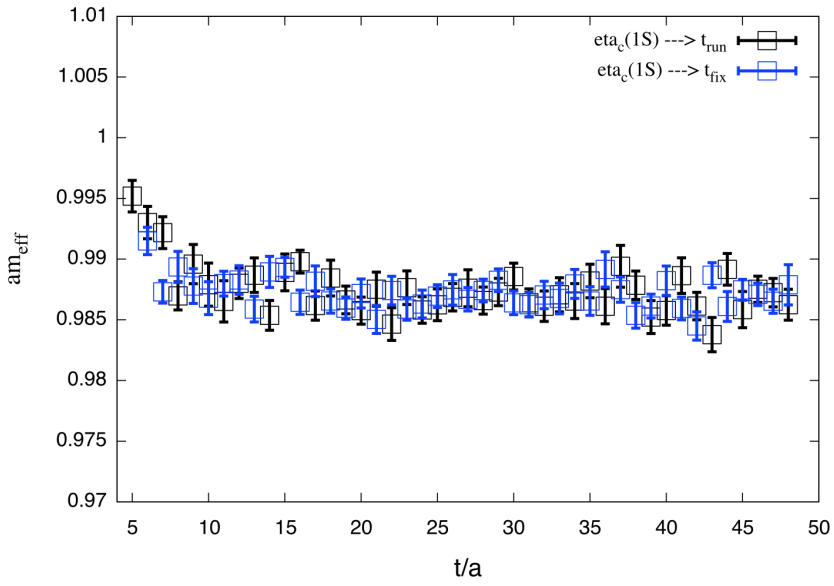

FIGURE 6.1: The $\eta_c(1S)$ effective mass for a $t_{\text{fix}} = 4a$ and for a t_{run}.

Excited States

For the excited states, the situation is different from that of the ground states. Although the fluctuations are even larger than for the ground states, the correlators $\tilde{C}^2_{A_0P}$ (5.21) and $\tilde{C}^2_{VV}$ (5.24) are qualitatively well fitted by a single contribution. We also studied the generalized eigenvector $v_2^{P(V)}(t,t_0)$ for $t = t_{\text{fix}}$ and $t = t_{\text{run}}$. The computation was done in the same way than for the ground states. In Fig. 6.2 the plot on the top stands for the projection of $v_2^P(t,t_0)$

on the correlator $\tilde{C}^2_{A_0P}$ for $\eta_c(2S)$, while the plot on the bottom stands for the projection of $v_2^V(t,t_0)$ on the correlator $\tilde{C}^2_{VV}$ for $\psi(2S)$. On both cases the dark points are for a non-fixed t and the blue lines are for a fixed t. Unlike the case for the ground state, for the excited state, in this case, the effective masses do depend on t_{fix} as we can see in Fig. 6.2.

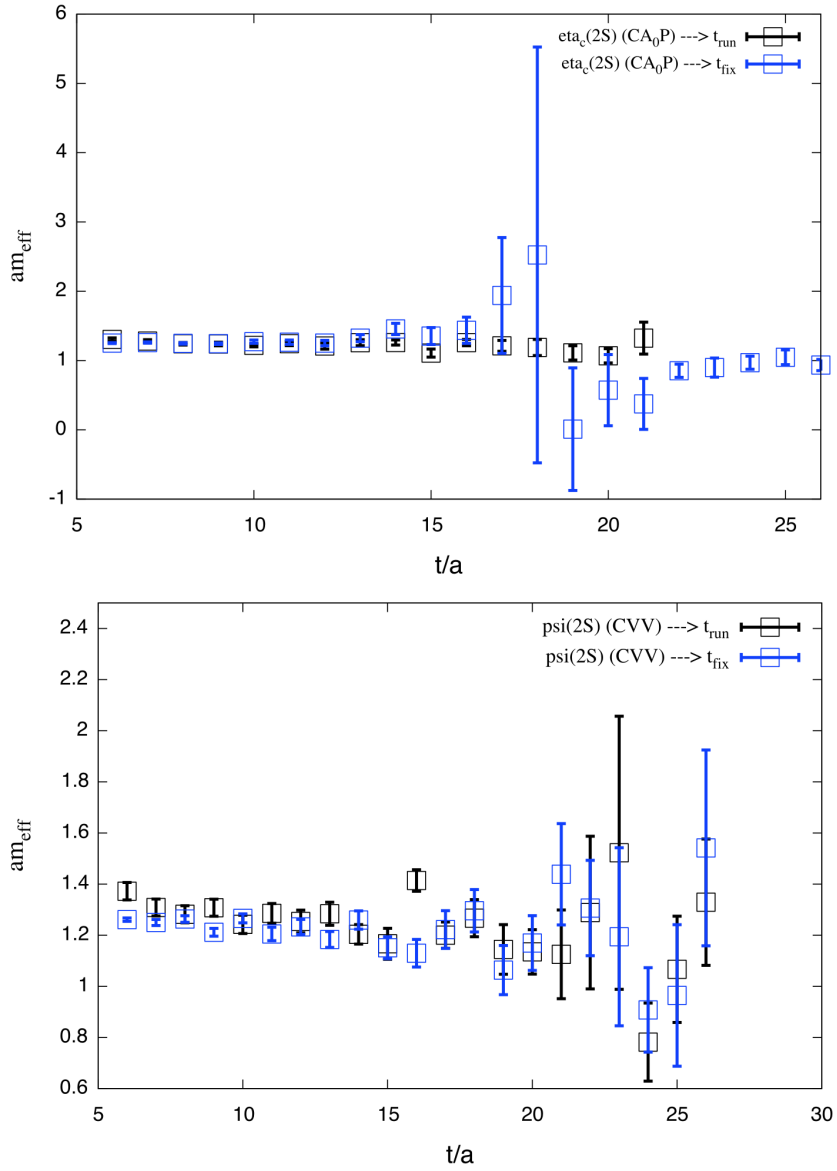

FIGURE 6.2: The $\eta_c(2S)$ (top) and $\psi(2S)$ effective masses for a $t_{\text{fix}} = 4a$ and for a t_{run}.

Time Range

For the ground states, the time range $[t_{\text{min}}, t_{\text{max}}]$ used to fit the projected correlators is set so that the statistical error on the effective mass $\delta m^{\text{stat}}(t_{\text{min}})$ is larger than the systematic error $\Delta m^{\text{sys}}(t_{\text{min}}) \equiv \exp[-\Delta t_{\text{min}}]$ with $\Delta = E_4 - E_1 \sim 2$ GeV. This choice is done to try to reduce the statistical uncertainty in our computation. The parameters E_4 and E_1 respectively stand for the energy of the third excited state and the ground state. That guesstimate is based on

our 4×4 GEVP analysis. Therefore, we cannot claim that we were able to control the energy level of the third excited state. Actually, we have considered $\delta m^{\text{stat}}(t_{\text{min}}) > 4\Delta m^{\text{sys}}(t_{\text{min}})$. The upper bound t_{max} of the particular fit interval per ensemble was fixed after an individual visual inspection of the quality of the effective mass plateau. The final numbers are normally invariant, as long as one stays within the plateau region. The choice of $\Delta^{(P)} \sim \Delta^{(V)}$ holds to a good approximation for the mass gaps in the pseudoscalar and vector channels at fixed lattice spacing and pion mass, thus identical fit intervals were chosen for pseudoscalar and vector meson states. For the first excited states, the time range has been set by looking at effective masses and where the plateau starts and ends, including statistical uncertainties.

Finally, we have investigated the influence of t_0 in our computation. We have chosen $t_0 = 3a$ at $\beta = 5.3$ and $t_0 = 5a$ at $\beta = 5.5$, but the results were invariant under different values of t_0.

Extrapolation to the Physical Point

We have extrapolated the measured quantities to the physical point by assuming a linear dependence on the squared (sea) pion mass (m_π^2), then our fit ansatz is written as

$$X(a, m_\pi) = X_0 + X_1 m_\pi^2 + X_2 (a/a_{\beta=5.3})^2 \tag{6.1}$$

where X is the observable extracted from the lattice, X_1 stands for the dependence on the sea quarks and X_2 stands for the dependence on the lattice spacing. In our case, we use the Wilson-Clover action, then we have a dependence on a^2. We recall that κ_c has been tuned at every κ_{sea} so that $m_{D_s}(\kappa_s, \kappa_c, \kappa_{\text{sea}}) = m_{D_s}^{\text{phys}}$. The parameters κ_{sea}, κ_{c} and κ_{s} stand for the value of the hopping parameter of the sea, charm and the strange quark respectively. It was necessary to tune the strange quark mass κ_s, though it is not a relevant quantity for the study discussed here (see Section 3.6). This tuning is done in the heavy quark hopping parameter κ in order to obtain the correct mass for the D_s meson.

6.3 Results

6.3.1 Charmonium Mass

The effective masses for the ground state (η_c and J/ψ) are obtained through eq. (6.2), while those of the first excited states ($\eta_c(2S)$ and $J/\psi(2S)$) were derived through eq. (6.3).

$$\begin{cases} am_{\eta_c}^{\text{eff}}(t) &= \text{arccosh}\left(\dfrac{\lambda_1^P(t+a,t_0) + \lambda_1^P(t-a,t_0)}{2\lambda_1^P(t,t_0)}\right) \\ am_{J/\psi}^{\text{eff}}(t) &= \text{arccosh}\left(\dfrac{\lambda_1^V(t+a,t_0) + \lambda_1^V(t-a,t_0)}{2\lambda_1^V(t,t_0)}\right) \end{cases} \tag{6.2}$$

$$\begin{cases} am^{\text{eff}}_{\eta_c(2S)}(t) &= \text{arccosh}\left(\dfrac{\lambda_2^P(t+a,t_0)+\lambda_2^P(t-a,t_0)}{2\lambda_1^P(t,t_0)}\right) \\ am^{\text{eff}}_{\psi(2S)}(t) &= \text{arccosh}\left(\dfrac{\lambda_2^V(t+a,t_0)+\lambda_2^V(t-a,t_0)}{2\lambda_1^V(t,t_0)}\right) \end{cases} \tag{6.3}$$

The signal values for the effective masses of $\eta_c(1S)$ and $\eta_c(2S)$ are illustrated in Fig. 6.3 and for $J/\psi(1S)$ and $\psi(2S)$ in Fig. 6.4. The solid lines correspond to our plateaus for the fitted masses. Both plots present similarities as they were produced using the same ensambles. In the plateau region, each effective mass $m^{\text{eff}}(t)$ is then fitted to a constant mass m. We checked that the results for the first radial excitation remain stable when we change the size of the matrix of correlators. We also checked that the choice of t_0 in the GEVP (4.21) does not have any impact on the results presented here. The fitting intervals to extract the masses for the lowest lying states are

$$\begin{aligned} t/a \in [11,29] \ , \ t/a \in [11,46] \\ t/a \in [11,45] \ , \ t/a \in [12,55] \\ t/a \in [13,46] \ , \ t/a \in [16,55] \end{aligned}$$

while for the radially excited states the following fit intervals have been chosen,

$$t/a \in [6,13] \ , \ t/a \in [8,15]$$

In Fig. 6.3 and Fig. 6.4, the ground state (dark lines) shows a longer plateau when compared to the excited states (red lines). This is related to the fact that the data for the ground states are more stable than those for the excited ones. We can also observe an increase in fluctuations as time increases for the excited states. This fact is perhaps due to our choice of interpolating fields to our correlation matrix in the GEVP. Moreover, we have not used t_{fix} (see Section 6.2) to extract the first excited states, because it could have caused a contamination in $\tilde{C}^2_{A_0P}$ and $\tilde{C}^2_{VV}$ from states other than those we are interested in. We are still investigating the origins of this behavior.

We show in Fig. 6.5 and Fig. 6.6, respectively, the extrapolation to the physical point of m_{η_c} and $m_{J/\psi}$. The errors in the continuum limit in both plots are coming from our fit using the MINUIT (see Section 4.4.1). The dark and red lines are the lattice values from our work, while the green and blue lines are, respectively, the physical value found by us and the value obtained from experiments. The color code is the same for the following plots. The dependence on m_π^2 and a^2 is mild, with cut-off effects which are almost negligible. However, the contribution to the meson masses besides the mass term $2m_c$ is difficult to quantify. At the physical point, our results for m_{η_c} and $m_{J/\psi}$ are compatible with the experimental values

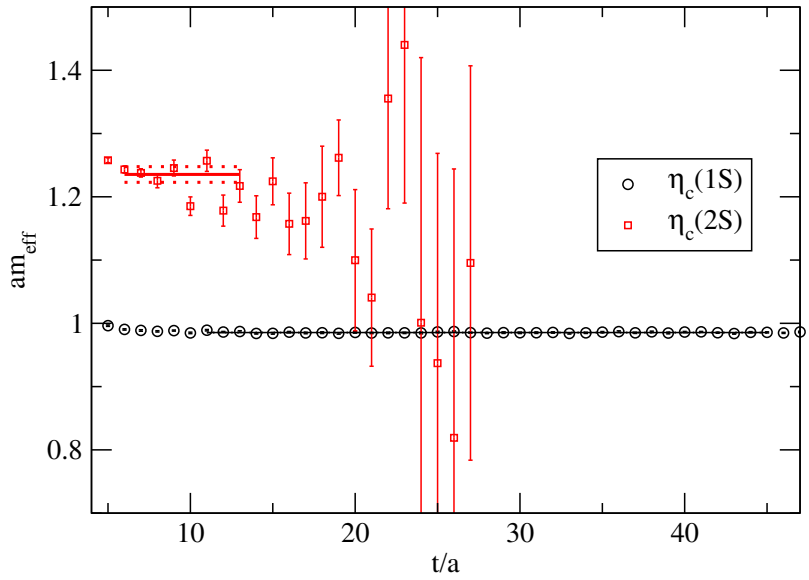

FIGURE 6.3: Effective masses am_{η_c} and $am_{\eta_c(2S)}$ extracted from a 4×4 GEVP for the lattice ensemble F7; we also plot the plateaus obtained in the chosen fit interval.

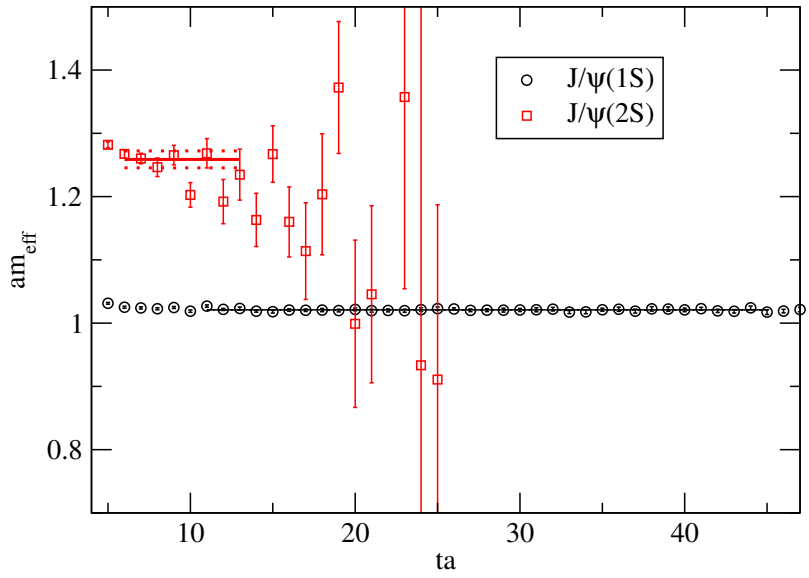

FIGURE 6.4: Effective masses $am_{J/\psi}$ and $am_{\psi(2S)}$ extracted from a 4×4 GEVP for the lattice ensemble F7; we also plot the plateaus obtained in the chosen fit interval.

2.983 GeV and 3.097 GeV [1]:

$$\boxed{m_{\eta_c} = 2.982(1)(19)\,\text{GeV}} \tag{6.4}$$

and

$$\boxed{m_{J/\psi} = 3.085(2)(20)\,\text{GeV}} \tag{6.5}$$

where the first error is statistical and the second error accounts for the systematic uncertainty

on the lattice spacing. The latter clearly dominates and hides a possible mismatch between our extrapolated results at the physical point and experiment. The systematic uncertainty could come, in particular, from the mistuning of κ_c due to the mistuning of κ_s.

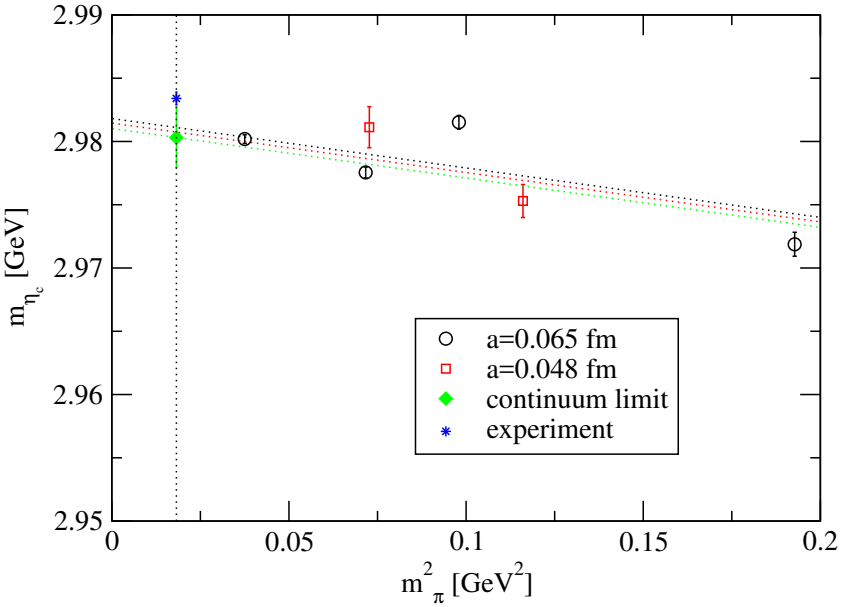

FIGURE 6.5: Extrapolation to the physical point of m_{η_c} by expressions linear in m_π^2 and a^2.

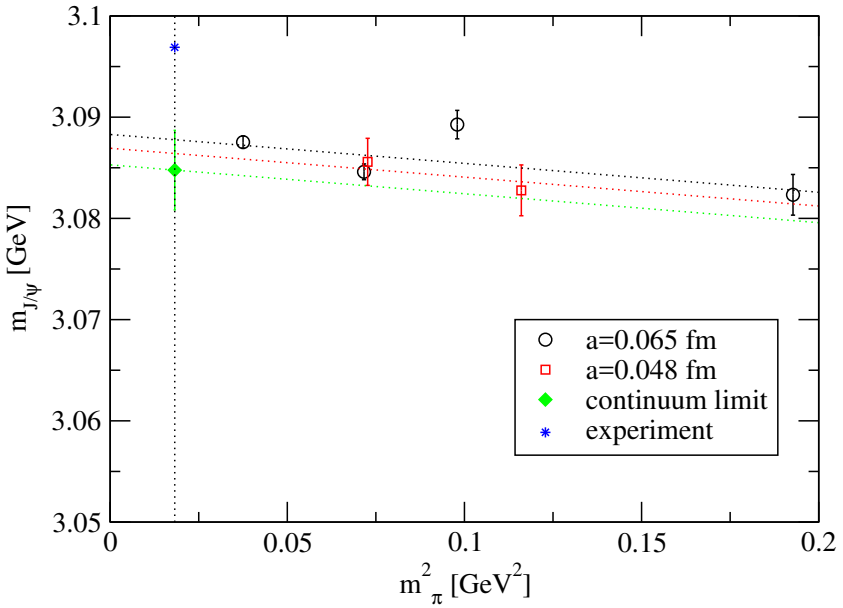

FIGURE 6.6: Extrapolation to the physical point of $m_{J/\psi}$ by expressions linear in m_π^2 and a^2.

6.3.2 Charmonium Decay Constants

We display in Figure 6.7 and in Figure 6.8 the extrapolations to the physical point of f_{η_c} and $f_{J/\psi}$, respectively. There are mild cut-off effects on f_{η_c} of the order of 4% at $\beta = 5.3$, while for

Fit	X_0[MeV]	X_1[MeV^{-1}]	X_2[MeV]	X_3[MeV^{-1}]	χ^2/dof	f_{η_c}
LO	386(3)	0.00005(1)	-16.7(2.7)	-	1.99	387(3)
NLO	391(6)	0.0006(7)	-17.1(2.7)	0.00006(6)	2.62	389(4)

Fit	X_0[MeV]	X_1[MeV^{-1}]	X_2[MeV]	X_3[MeV^{-1}]	χ^2/dof	$f_{J/\psi}$
LO	397(4)	0.00010(2)	37.2(3.8)	-	0.98	399(4)
NLO	401(7)	-0.0003(9)	36.4(4.2)	0.00003(7)	1.41	401(8)

TABLE 6.2: LO and NLO fit parameters and results for f_{η_c} and $f_{J/\psi}$, with their respective χ^2 per number of degrees of freedom.

$f_{J/\psi}$ they are stronger by about 10%.

In addition, we have tried to extrapolate our lattice observables to the physical point by using a fit form inspired by partially quenched heavy meson chiral perturbation theory, where the charm quark is treated as heavy. In this fit we adopt again a fit ansatz linear in m_π^2 (and a^2), but now we have a chiral logarithm-term $m_\pi^2 \ln(m_\pi^2)$,

$$f_{\eta_c} = X'_{\eta_c 0} + X'_{\eta_c 1} m_\pi^2 + X'_{\eta_c 2}(a/a_{\beta=5.3})^2 + X'_{\eta_c 3} m_\pi^2 \ln(m_\pi^2), \tag{6.6}$$

$$f_{J/\psi} = X'_{J/\psi 0} + X'_{J/\psi 1} m_\pi^2 + X'_{J/\psi 2}(a/a_{\beta=5.3})^2 + X'_{J/\psi 3} m_\pi^2 \ln(m_\pi^2). \tag{6.7}$$

We have called this fit structure NLO and we have collected in Table 6.2 all our fit results (LO and NLO), together with fit parameters and χ^2 per degree of freedom. We have found that χ^2(NLO) is worse than χ^2(LO). Furthemore, the fit parameters X'_1 and X'_3 are compatible with zero, while X_1 is different from zero. So, we have decided to consider the LO result as our prefered one and not to include the discrepancy between LO and NLO in the systematic errors on f_{η_c} and $f_{J/\psi}$. We do not have enough data points to be confident in NLO fits on quantities whose chiral dependence is, in any case, small. Moreover we do not see any evidence for the significance of the chiral logarithmic-term in eqs. (6.6) and (6.7). We have used the same time intervals presented in Section 6.3.1 to perform the fit.

We obtain at the physical point

$$\boxed{f_{\eta_c} = 387(3)(3)\,\text{MeV}} \tag{6.8}$$

and

$$\boxed{f_{J/\psi} = 399(4)(2)\,\text{MeV}} \tag{6.9}$$

where the systematic error comes from the uncertainty on the lattice spacings.

6.3.3 Comparing our Results to Experimental Data

Masses

We have compared the results of the ground state charmonium masses with the results provided by the PDG (see Table 6.3) and we can observe that our results reproduce very well the

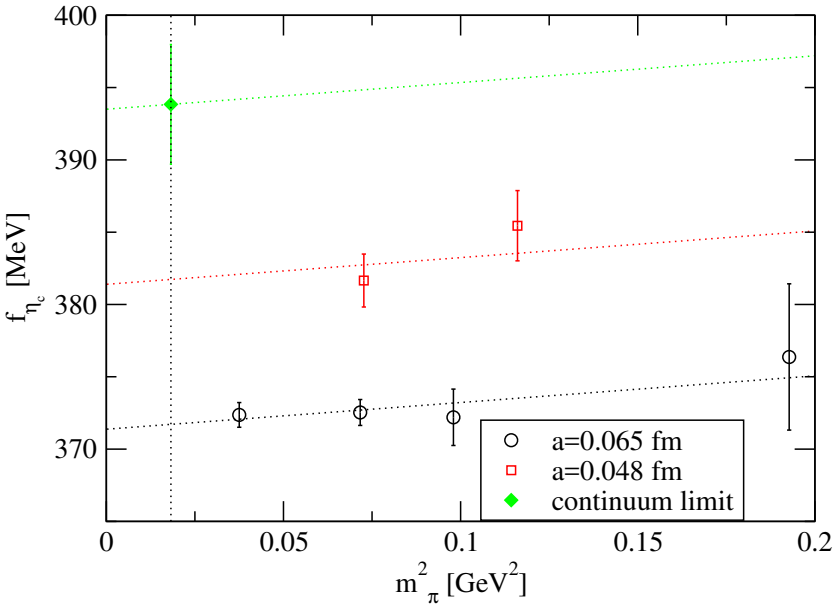

FIGURE 6.7: Extrapolation to the physical point of f_{η_c} by expressions linear in m_π^2 and a^2.

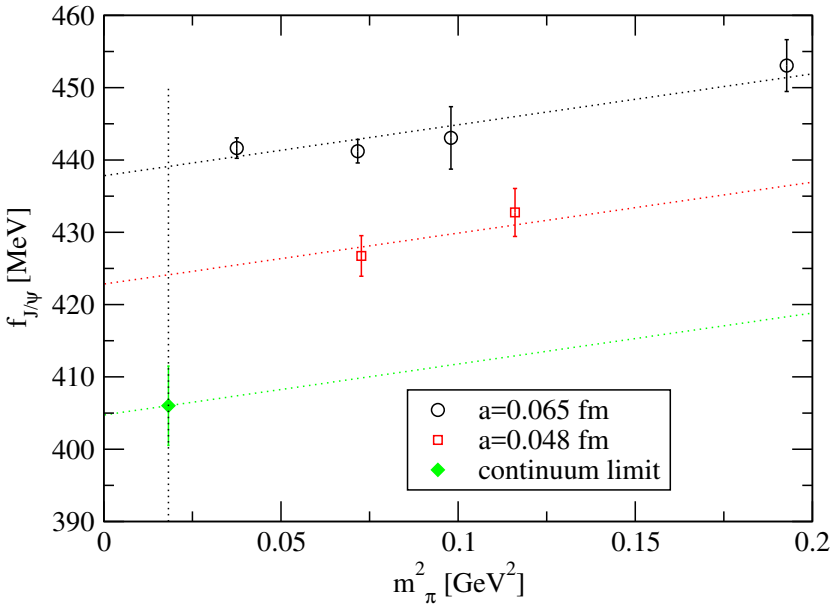

FIGURE 6.8: Extrapolation to the physical point of $f_{J/\psi}$ by expressions linear in m_π^2 and a^2.

experimental values of both η_c and J/ψ meson masses.

Decay Constants

We display in Fig. 6.9 the comparison between our results for f_{η_c}, named "This work $N_f = 2$", with those available in the literature. In the same way, Fig. 6.10 compares the results present in the literature to the result of this work for $f_{J/\psi}$.

	m_{η_c}	$m_{J/\psi}$
Our Results	2.982(1)(19) GeV	3.085(2)(20) GeV
PDG [1]	2.983 GeV	3.097 GeV

TABLE 6.3: Our results to the charmonium ground states, comparing with the PDG values.

Vector case: $f_{J/\psi}$

In Fig. 6.10 we added a phenomenological estimate of $f_{J/\psi}$. This result is derived from the decay width expression [153]

$$\Gamma(J/\psi \to e^+e^-) = \frac{4\pi}{3}\frac{4}{9}\alpha^2(m_c^2)\frac{f_{J/\psi}^2}{m_{J/\psi}} \tag{6.10}$$

together with the experimental determination of the J/ψ mass and width, and setting $\alpha_{\rm em}(m_c^2) = 1/134$ [168]. In the end, one gets

$$f_{J/\psi}^{\text{“pheno”}} = 407(6)\,\text{MeV} \tag{6.11}$$

We have compared the above result with the one extracted by us (6.9) and they are compatible (see Fig. 6.10). Moreover, we can use this computation to check the reliability of our method. Our result presented in eq. (6.9) agrees with the one obtained in (6.11).

Pseudoscalar Case: f_{η_c}

Unlike $f_{J/\psi}$, we cannot compute a phenomenological estimate for f_{η_c}. We find in Ref. [153] a relation similar to that proposed in the case of J/ψ (6.10)

$$\Gamma(\eta_c \to \gamma\gamma) = \frac{64\pi\alpha^2}{81 m_{\eta_c}}\frac{f_{\eta_c}^2}{(1+\delta)^2} \tag{6.12}$$

where δ is an unknown term. In Ref. [153] some studies are carried out to estimate a value for this term. However, a final conclusion was not obtained. Therefore, in this work we do not present phenomenological estimates for the decay constant f_{η_c}. However, this observable is relevant for several physical phenomena. For example, f_{η_c} is crucial for the theoretical descriptions of the $\gamma^*\gamma^* \to \eta_c$ form factor [169–172]. In addition, phenomenological studies of the small-x gluon distribution function from the inclusive production of η_c requires knowledge of f_{η_c} [12].

Collection of Results

In Fig. 6.9 and Fig. 6.10 we compare our results with those presented by the HPQCD[1] [110] and ETM [153] collaborations. In the following we will discuss the different results obtained by ETM and HPQCD Collaborations.

[1] http://www.physics.gla.ac.uk/HPQCD/

- ETMC: We begin with $N_f = 2$ calculations. The ETMC performs its calculations in the chiral regime, with pion masses down to about 270 MeV. Moreover, the continuum extrapolation is done with three lattice spacings: $a = 0.054$ fm, $a = 0.067$ fm and $a = 0.098$ fm. In their study, they have used twisted quark masses.

- HPQCD'10 [173, 174] and HPQCD'12 [175, 176]: They performed a $N_f = 2 + 1$ calculation, where HPQCD used highly improved staggered quarks[2]. The HPQCD'12 computation improves on the one of HPQCD'10 in a number of ways. The new computation was performed with $a = 0.144$ fm, but with pion masses down to $171(1)$ MeV, and valence pion masses down to $143(1)$ MeV in a volume of $(4.6 \text{ fm})^3$ compared to 290 MeV, 225 MeV and $(2.7 \text{ fm})^3$ in HPQCD'10. The only drawback of the HPQCD calculation comes from the fact that two of their three latice spacings ($a \approx 0.15$ fm, $a \approx 0.12$ fm and $a \approx 0.08$ fm) are larger than 0.1 fm, while the finest is only 0.085 fm.

Our procedure is not the same as the one performed by the groups mentioned above. However we can observe similarities in the results. In Fig. 6.9 we can confirm that our result is compatible with the one presented by ETMC given the error estimations. However, we are not in agreement with the results obtained by HPQCD'10. We could explain the arbitrariness in the results by the fact that we have performed a $N_f = 2$ simulation, while HPQCD'10 has performed a $N_f = 2 + 1$. Moreover, they have considered lattice spacings and values of the pion mass larger than ours (see Table 6.1).

In Fig. 6.10 there is a clear improvement of the results obtained by HPQCD'12. This improvement can be due to the fact that they performed new simulations with a smaller pion mass and in a larger lattice volume. Moreover, the lattice artefacts are of order a, while for staggered fermions the lattice corrections start at order a^2 [178]. In the calculation for $f_{J/\psi}$ our results differ slightly from those extracted by ETMC. A possible reason for explaining this difference is due to the fact that ETMC has used twisted quark masses (and we have used Wilson-Clover fermions) and considered three lattice spacings while we have considered two. However, our value can still be compatible with ETMC estimations, given their error values.

Knowing that the lattice actions are very different, the fact that these results agree quite well is a good indication of the robustness of the lattice QCD predictions. Still, our results appear to be compatible with the two previous lattice estimations available so far in the literature.

6.3.4 Ratios of Masses and Decay Constants for Excited States

In this section, we will explore the charmonium excited states through the ratios of their masses and decay constants. We have used the same time intervals presented in Section 6.3.1 to perform a fit. The study of these ratios allows us to avoid systematic errors related to the lattice spacing.

[2] *Staggered fermions* are a formulation where the 16-fold degeneracy of the naïve discretization is reduced to only four quarks, while at the same time a remnant chiral symmetry is maintained. This is achieved by a transformation which mixes spinor and space-time indices, distributing the quark degrees of freedom on the hypercubes [26, 110, 177].

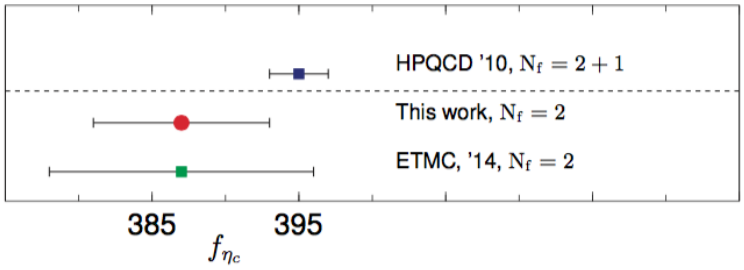

FIGURE 6.9: Collection of lattice results for f_{η_c}.

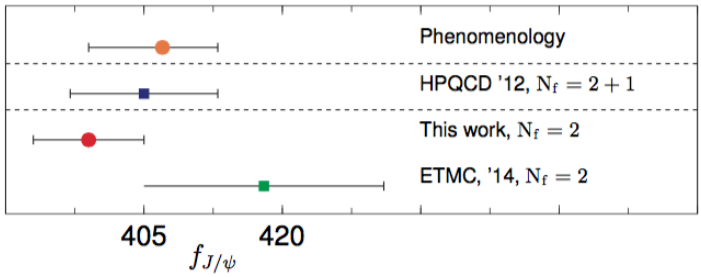

FIGURE 6.10: Collection of lattice results for $f_{J/\psi}$.

Masses

The situation for the excited states is less favorable than the one presented in the previous sections. We present in Fig. 6.11 and in Fig. 6.12 the extrapolation to the continuum limit of the ratios $m_{\eta_c(2S)}/m_{\eta_c}$ and $m_{\psi(2S)}/m_{J/\psi}$, compared to the experimental values [1]. Since the cut-off effects are small, of the order of 5%, it is very unlikely to have points in the continuum limit significantly lower than our lattice data.

We find

$$\boxed{\frac{m_{\eta_c(2S)}}{m_{\eta_c}} = 1.281(7) > \left(\frac{m_{\eta_c(2S)}}{m_{\eta_c}}\right)^{\text{exp}} = 1.220} \tag{6.13}$$

and

$$\boxed{\frac{m_{\psi(2S)}}{m_{J/\psi}} = 1.271(7) > \left(\frac{m_{\psi(2S)}}{m_{J/\psi}}\right)^{\text{exp}} = 1.190} \tag{6.14}$$

In [179], lattice results were much closer to the experimental ones but the slope in a^2 was probably overestimated from the coarsest lattice point: points at lattice spacings similar to those used in our work are compatible with our data.

Decay Constants

Our investigation for the first radially excited charmonium decay constants exhibits a behavior that motivates further studies, as can be seen from the results for the ratios of the decay

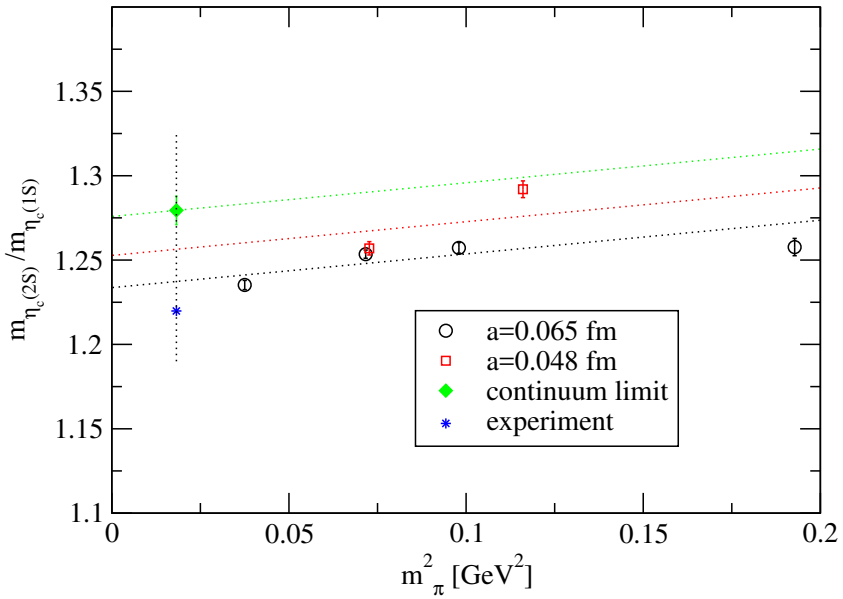

FIGURE 6.11: Extrapolation to the physical point of $m_{\eta_c(2S)}/m_{\eta_c}$ by linear expressions in m_π^2 and a^2.

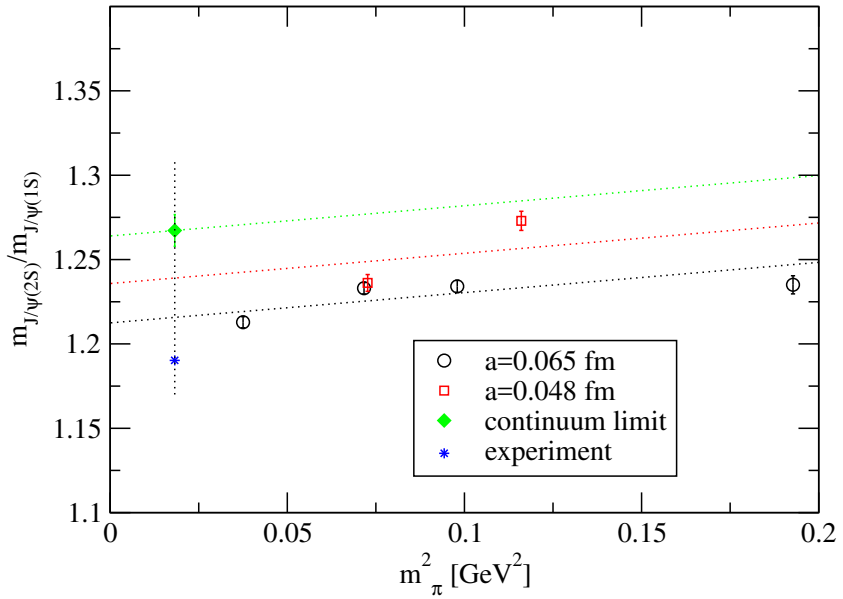

FIGURE 6.12: Extrapolation to the physical point of $m_{\psi(2S)}/m_{J/\psi}$ by linear expressions in m_π^2 and a^2.

constants which are presented in Fig. 6.13 and Fig. 6.14.

The results of this work are

$$\boxed{\frac{f_{\eta_c(2S)}}{f_{\eta_c}} = 0.81(8) < 1} \tag{6.15}$$

and

$$\boxed{\frac{f_{\psi(2S)}}{f_{J/\psi}} = 1.18(9) > 1} \tag{6.16}$$

This is a very puzzling result and, at the moment, we are yet to understand the reason of this large spin breaking (since the vector meson has spin 1) effect:

1. Projected correlators $\tilde{C}^2$ in the pseudoscalar and the vector sector show the same quality fit with similar fluctuations.

2. We performed a global fit of individual correlators $C_{V^{(i)}V^{(j)}}(t)$ by a series of 3 exponential contributions:

$$\begin{aligned} C_{V^{(i)}V^{(j)}}(t) &= Z_1^i Z_1^{*j} e^{-m_{V_1} T/2} \cosh[m_{V_1}(T/2-t)] + Z_2^i Z_2^{*j} e^{-m_{V_2} T/2} \cosh[m_{V_2}(T/2-t)] \\ &+ Z_3^{ij} e^{-m_3^{ij} T/2} \cosh[m_3^{ij}(T/2-t)] \end{aligned} \tag{6.17}$$

   where the "*effective*" remaining mass m_3, resumming any contributions but the ground state and the first excited state, can be different for every correlator.

3. The decay constants of J/ψ and $\psi(2S)$ are proportional to

$$\frac{Z_1^0}{\sqrt{m_{V_1}}} \quad \text{and} \quad \frac{Z_2^0}{\sqrt{m_{V_2}}} \tag{6.18}$$

   respectively, where the local-local vector two-point correlator corresponds to $i = j = 0$ and we find the hierarchy

$$\frac{Z_2^0}{\sqrt{m_{V_2}}} \gtrsim \frac{Z_1^0}{\sqrt{m_{V_1}}} \tag{6.19}$$

   in our data. It thus appears very unlikely to get, in the continuum limit, $f_{\psi(2S)}/f_{J/\psi} < 1$ using this procedure either.

4. Neglecting disconnected diagrams could be a source for the problem.

5. Increasing the number of dynamical quarks could help reducing the spin breaking effects (this has been observed on quantities like $f_{D_s^*}/f_{D_s}$ [180–183]).

6. The width $\Gamma(\psi(2S) \to e^+e^-)$ is smaller than its ground state counterpart $\Gamma(J/\psi \to e^+e^-)$, that is 2.34 keV versus 5.56 keV [1]. Written in terms of the decay constant $f_{\psi(2S)}$ and the mass $m_{\psi(2S)}$, this is a serious clue that $f_{\psi(2S)}/f_{J/\psi} < 1$ (a possible caveat with this approach is that QED effects might be quite large, making, as is done in our work, the encoding in $f_{\psi(2S)}$ as purely QCD contributions not so straightforward).

7. A lattice study, performed in the framework of Non-Relativistic QCD (NRQCD), leads to the upsilon (Y) decay constant ratios $f_{\Upsilon'}/f_{\Upsilon} < 1$ (in the bottomium sector) [184].

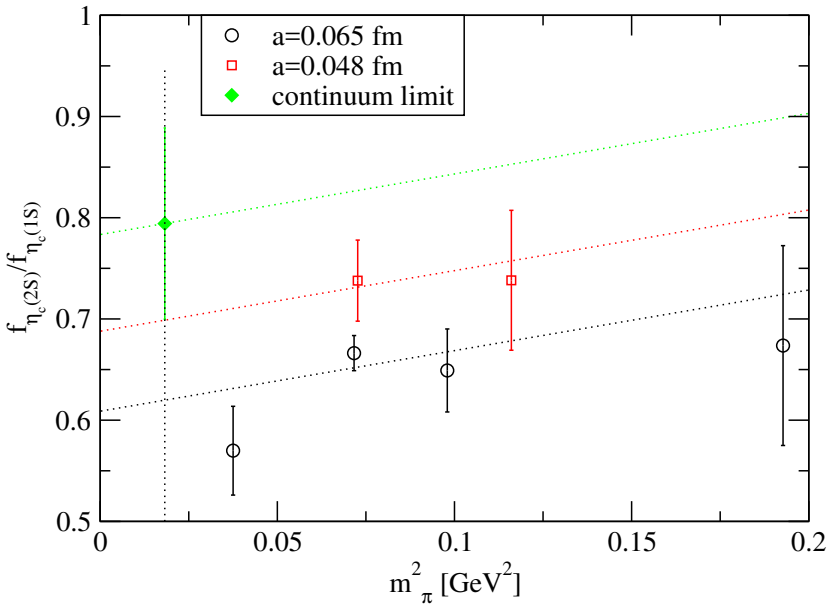

FIGURE 6.13: Extrapolation to the physical point of $f_{\eta_c(2S)}/f_{\eta_c}$ by linear expressions in m_π^2 and a^2.

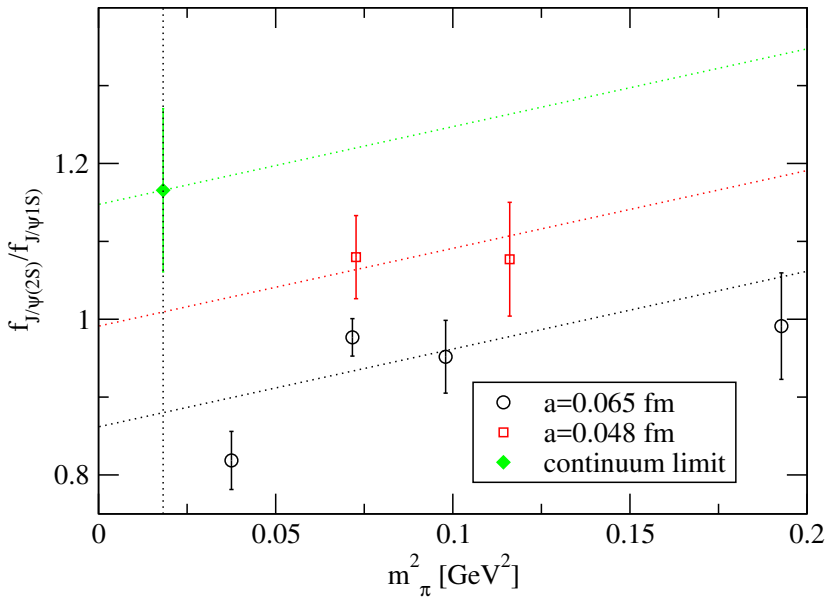

FIGURE 6.14: Extrapolation to the physical point of $f_{\psi(2S)}/f_{J/\psi}$ by linear expressions in m_π^2 and a^2.

6.4 Possible Applications of Our Results

The discovery at LHC of the Higgs boson with a mass of 125.09(24) GeV [16] has been a major milestone in the history of the Standard Model: the spontaneous breaking of electroweak symmetry generates the masses of the charged leptons, quarks and weak bosons. We can point out a well-known issue with the SM Higgs: the quartic term in the Higgs Lagrangian induces a quadratic divergence in the Higgs boson mass with the hard scale of the theory, which is related to the so-called hierarchy problem.

Several scenarios beyond the SM are proposed to fix that theoretical caveat. Some of the

minimal extensions of the Higgs sector contain two complex scalar isodoublets $\Phi_{1,2}$ which, after the spontaneous breaking of the electroweak symmetry, lead to 2 charged particles $H^{\pm}$, 2 CP-even particles h (SM-like Higgs boson) and H, and 1 CP-odd particle A. In that class of scenarios, quarks are coupled to the CP-odd particle through a pseudoscalar current [185–190]. Those extensions of the Higgs sector (called 2HDM) have interesting phenomenological implications, especially as far as pseudoscalar quarkonia are concerned. For example, their leptonic decay is highly suppressed in the SM because it occurs via quantum loops but it can be reinforced by the new tree-level contribution involving the CP-odd Higgs boson, in particular in the region of the parameter space where the new boson is light ($10\,\text{GeV} \lesssim m_A \lesssim 100\,\text{GeV}$) [186, 191]. Any enhanced observation with respect to the SM expectation would be indeed a clear signal of New Physics. Let us finally note that the hadronic inputs, which constrain the CP-odd Higgs coupling to heavy quarks through processes involving quarkonia, are the decay constants f_{η_c} and f_{η_b}.

6.5 Partial Conclusions

In this work we investigated a $N_f = 2$ lattice QCD study on some aspects of quarkonia physics. The decay constants f_{η_c} and $f_{J/\psi}$ are in the same ballpark as the previous lattice estimations so far available in the literature, and present cut-off effects which seem to be limited to 10%. These are very good results, meaning our estimations are reliable. However, for the excited states, we encountered issues which are difficult to circumvent.

As a first solution, we have proposed to enlarge a basis of operators in the GEVP analysis by including interpolating fields with covariant derivatives or operators of the π_2 and ρ_2 kind. However they suffer from large statistical fluctuations caused by numerical cancellations among various contributions, or from the more serious conceptual problem that, in GEVP, mixing T-even and T-odd operators has no real sense. Furthemore, we have observed that $m_{\eta_c(2S)}/m_{\eta_c}$ and $m_{\psi(2S)}/m_{J/\psi}$ are not significantly affected by cut-off effects, being only 5% larger than the experimental ratios.

The information about the decay constants $f_{\eta_c(2s)}/f_{\eta_c} \sim 0.8$ is interesting, as these quantities are hadronic inputs that govern the transitions $\eta_c \to l^+l^-$, $h \to \eta_c l^+l^-$, $\eta_c(2S) \to l^+l^-$ and $h \to \eta_c(2S)l^+l^-$ with a light CP-odd Higgs boson as an intermediate state[3].

Unfortunately our result $f_{\psi(2S)}/f_{J/\psi} > 1$ renders the picture less bright, unless one admits that there are large spin breaking effects. This clearly motivates future investigation.

[3] In the cases $h \to \eta_c l^+l^-$ and $h \to \eta_c(2S)l^+l^-$, the other hadronic quantities which enter the process are the distribution amplitudes of the charmonia.

Chapter 7

Conclusions and Outlook

The LQCD formulation provides a non-perturbative framework to compute relations between Standard Model parameters and experimental quantities. In this work, we have presented the results of our study on charmonium systems from lattice QCD with two dynamical quarks. We have presented the method used to extract the observables of interest from the lattice. All results were extrapolated to the continuum and chiral limits analyzing a subset of the CLS lattice ensembles, and since physical volumes are large, $Lm_\pi > 4$, volume effects are expected to be negligible.

Charmonium spectroscopy plays an important role in understanding the strong interaction, described by QCD. Therefore in Chapter 3, we have explained the procedure to extract the masses and decay constants from the ground states by using two-point correlation functions. After the study of the ground state, we focused on the first excited states. In order to extract the spectrum of the excited states, we could have performed a multi-exponential fit in the correlators, but that approach is unstable and hence we decided to use the GEVP method. This method involves all-to-all propagators and it is a helpful tool to reduce systematic errors. We need to remember that the quality and usefulness of a result normally depends on the size of its error bars. Therefore, we try to use methods that reduce lattice errors as much as possible.

Another key point of our work is the study of excited states. Thus we dedicated Chapter 4 to the hadron spectroscopy of excited states by using the GEVP, with a suitable basis of interpolating fields for the states of interest. In addition, we explored the procedure to extract the mass and the decay constants by using only the GEVP elements (eigenvalues and eigenvectors). The variational techniques such as the GEVP are computationally costly, because additional quark propagators have to be computed, if the basis functions are smeared. The amount of computer time will depend also on the number of basis states. Moreover, the efficiency of a basis state is not clear until the calculation is done. Despite this drawback, these techniques are robust and efficient for extraction of excited states. Therefore, we use them together with computational methods that increase computational speed such as the DD-HMC package [162–164]. We also presented the computational tools we used in this first step of our work which are crucial to get good correlators. Finally, to compute the eigenvalues and eigenvectors from our matrix of correlators, we used the LAPACK library and to fit our data MINUIT. The errors were estimated using the jackknife procedure. Although there are several methods to investigate errors, we can emphasize that jackknife method is a useful one for

large samples.

This work is devoted to the study of the charmonium on the Lattice. So in Chapter 5 we present the discussion about the mesons we are interested in:

- Pseudoscalar Mesons: $\eta_c(1S)$ (ground state) and $\eta_c(2S)$ (first excited state).
- Vector Mesons: $J/\psi(1S)$ (ground state) and $\psi(2S)$ (first excited state).

Moreover, we explained our choice of operators as well as the correlators we have computed. We also noted that the construction of interpolating fields from the basis

$$\{\bar{c}\Gamma c \;\; ; \;\; \bar{c}\Gamma(\vec{\gamma}\cdot\vec{\nabla})c\} \tag{7.1}$$

can be problematic since the operator with a covariant derivative $\bar{c}\Gamma(\vec{\gamma}\cdot\vec{\nabla})c$ gives a contribution equal to zero, hence a correlator with a very noisy signal. As a consequence of this finding, we have decided not to use in our computation correlators with covariant derivatives.

During our work we discussed the importance of isolating states of interest so that there would be no contamination from other states. One of the techniques to accomplish this is the smearing technique. Some studies [192] indicate that that by using an improved sink-source smearing technique, one can have a much better control over excited state contributions when compared to results without smearing. Therefore, in our simulations we have considered four Gaussian smearing levels for the quark field c, including no smearing, to built our 4×4 matrix of correlators without any covariant derivative or operator of the kind π_2 or ρ_2, from which we have extracted the $\mathcal{O}(a)$ improved hadronic quantities we have investigated. Next, we presented the implementation of the GEVP method to study the spectroscopy of the charmonium states. Finally, we explored the procedure to extract the decay constants and the observables of interest as well as the non-perturbative renormalization of the axial and vector currents. This second study was important to understand the behavior of the GEVP method as well as how to extract the observables. In addition, in the literature there is a vast amount of material available on this method (including material published by members of our collaboration), which helped us to identify and check the basic steps of our work.

In Chapter 6 we focus on our results, which we will briefly summarize . The results below are for ground state mesons. In this case, we have observed that the ground state shows a long plateau and a stable data. Next, we perform fits at different time intervals and, at the end, we extract the desired values. As a final step we perform an extrapolation to the physical point, were we assumed a linear dependence in m_π^2 and in a^2.

Masses

$$\boxed{m_{\eta_c} = 2.982(1)(19)\,\text{GeV}} \quad \text{and} \quad \boxed{m_{J/\psi} = 3.085(2)(20)\,\text{GeV}}$$

We have compared the results of the ground state charmonium masses with the results provided by the PDG [1] and we can conclude that they are compatible.

Decay Constants

$$\boxed{f_{\eta_c} = 387(3)(3)\,\text{MeV}} \quad \text{and} \quad \boxed{f_{J/\psi} = 399(4)(2)\,\text{MeV}}$$

We compared our results with those presented by the HPQCD [110] and ETMC [193] collaborations. Although the procedure of these groups is different from this work, our results appear to be compatible with the two previous lattice estimations available so far in the literature.

In the following, we present the result of this work for the first radially excited state. The ground state showed a longer plateau when compared to the excited states. This is related to the fact that the data for the ground states are more stable than those of the excited ones. We could also observe an increase in fluctuations as time increases for excited states. This fact is perhaps due to our choice of interpolating fields or our correlation matrix in the GEVP. We are still investigating the origins of this behavior.

Masses

$$\boxed{\frac{m_{\eta_c(2S)}}{m_{\eta_c}} = 1.281(7) > \left(\frac{m_{\eta_c(2S)}}{m_{\eta_c}}\right)^{\text{exp}} = 1.220}$$

and

$$\boxed{\frac{m_{\psi(2S)}}{m_{J/\psi}} = 1.271(7) > \left(\frac{m_{\psi(2S)}}{m_{J/\psi}}\right)^{\text{exp}} = 1.190}$$

In [179], lattice results were much closer to the experimental ones but the slope in a^2 was probably overestimated from the coarsest lattice point: points at lattice spacings similar to those used in our work are compatible with our data.

Decay Constants

$$\boxed{\frac{f_{\eta_c(2S)}}{f_{\eta_c}} = 0.81(8) < 1}$$

and

$$\boxed{\frac{f_{\psi(2S)}}{f_{J/\psi}} = 1.18(9) > 1}$$

We have found the ratio $f_{\psi(2S)}/f_{J/\psi}$ to the decay constants higher than 1. There are several reasons to believe that this raises some difficulties. We discussed the issue and proposed possible solutions.

Our results for both the ground state and the excited states are in agreement with those currently available in the literature. This is important because it shows that the method chosen

in this work is reliable. However, for the excited states, the situation is less bright as we were faced with the inherent difficulties of dealing with excitations.

Perspectives

We would like to perform new investigations in order to circumvent excited states difficulties. Furthemore, we believe that our work is a good starting point for new studies involving η_c and J/ψ charmonium states. As we discussed in Chapter 6, the information about the decay constants $f_{\eta_c(2s)}/f_{\eta_c} \sim 0.8$ is relevant for new researches. However, our result $f_{\psi(2S)}/f_{J/\psi} > 1$ motivates us to continue our work in order to find solutions to this result. Some possible solution for our issue could be increasing the number of dynamical quarks[1] in order to try to reduce the spin breaking effects. Another possible solution is to include QED effects in the computation of $f_{\psi(2S)}$. Finally, a natural extension of this work would be to study the bottomonium ($b\bar{b}$ states) sector. We can use step scaling in masses in order to extrapolate our results to the bottom region, notably in the measurement of f_{η_b}, which is relevant in models with a light CP-odd Higgs.

[1] In literature we can find lattice results with $N_f = 2+1$ [194] and $N_f = 2+1+1$ [195].

Appendix A

Details about Two-Point Correlation Functions

A.1 Two-Point Correlation Functions on the Lattice

This paragraph addresses in detail two-point correlations functions on the lattice, as well as the physical quantities that can be extracted from them.

A.1.1 Construction of the two-point correlation functions

We present in the following the derivation of two-point correlation functions in momentum space, that is for a state of momentum $\vec{p}$.

Starting point

Our starting point will be, in the *euclidean* formulation, the space-time two-point correlation function

$$C_{12}(t,\vec{x}) \overset{def}{=} \langle \Omega | \mathcal{O}_1(t,\vec{x})\, \mathcal{O}_2^\dagger(0,\vec{0}) \rangle \, |\Omega > \tag{A.1}$$

When transported back to minkowski space, this expression reads

$$\langle \Omega | T \left[\mathcal{O}_1(x) \mathcal{O}_2^\dagger(0) \right] |\Omega \rangle$$

which can be interpreted as the green function which describes the probability amplitude to create a state with the quantum numbers of $\mathcal{O}_2$ at the space time point $x = (t, \vec{x}) = (0, \vec{0})$ which propagates to the space time point $x = (t, \vec{x})$ where it is annihilated because of $\mathcal{O}_1(x)$.

Fourier transform

Since we are interested in describing systems with a certain momentum $\vec{p}$ at a certain time t, we need to Fourier transform the space dependency in the correlator (A.1)

$$C_{12}(t,\vec{x}) \overset{FT}{\rightsquigarrow} \tilde{C}_{12}(t,\vec{p})$$

with

$$\tilde{C}_{12}(t,\vec{p}) = \sum_{\vec{x}} \langle \Omega | \mathcal{O}_1(t,\vec{x}) \mathcal{O}_2^\dagger(0,\vec{0}) | \Omega \rangle \, e^{i\vec{p}\cdot\vec{x}}$$

where we have used the discretized Fourier transform on the lattice. There is still an i in the exponential because only the time which is Wick-rotated in the euclidean (not the space).

Insertion of a complete set of states

Let us introduce now a complete set of normalized energy eigenstates E_n with momentum $\vec{p}_n$ and rest-mass m_n (so that $E_n = \sqrt{m_n^2 + \vec{p}_n^2}$) and distinguish two cases

1. *non-polarized states*: denoting the states by $|n;\, \vec{p}_n\rangle$, we have

$$\begin{cases} \langle n;\, \vec{p}_n | m;\, \vec{p}_m \rangle = (2\pi)^3\, 2E_n\, \delta_{n,m} \qquad \text{(relativistic normalization)} \\ \displaystyle\sum_{n,\,\vec{p}_n} \frac{|n;\, \vec{p}_n\rangle\, \langle n;\, \vec{p}_n|}{(2\pi)^3\, 2E_n} = \mathbf{1} \qquad \text{(closure relation)} \end{cases}$$

2. *polarized states*: if the states are polarized, we need to add an extra polarization index λ_n so that

$$\begin{cases} \langle n;\, \lambda_n;\, \vec{p}_n | m;\, \lambda_m;\, \vec{p}_m \rangle = (2\pi)^3\, 2E_n\, \delta_{n,m} \\ \displaystyle\sum_{n,\vec{p}_n,\lambda_n} \frac{|n;\, \lambda_n;\, \vec{p}_n\rangle\, \langle n;\, \lambda_n;\, \vec{p}_n|}{(2\pi)^3\, 2E_n} = \mathbf{1} \end{cases}$$

Then, we obtain for non-polarized states

$$\tilde{C}_{12}(t,\, \vec{p}) = \sum_{\vec{x}} \sum_{n,\vec{p}_n} \frac{e^{i\vec{p}\cdot\vec{x}}}{(2\pi)^3 2E_n}\, \langle \Omega | \mathcal{O}_1(t, \vec{x}) | n; \vec{p}_n \rangle\, \langle n; \vec{p}_n | \mathcal{O}_2^\dagger(0, \vec{0}) | \Omega \rangle \tag{A.2}$$

Space-time translational invariance on the lattice

This invariance means that we can compute an operator at a particular space-time point from the knowledge of this operator at another space-time point and the generators of the space-time translation of the Poincaré group $\{H;\, \vec{P}\}$. Explicitely, we have

$$\mathcal{O}_1(t,\, \vec{x}) \;=\; e^{H\,t + i\,\vec{x}\cdot\vec{P}}\, \mathcal{O}_1(0,\, \vec{0})\, e^{-H\,t - i\,\vec{x}\cdot\vec{P}}$$

There is no i in front of the time part because of the Wick rotation to the euclidean.

Action on the vacuum and on the $|n;\, \vec{p}_n\rangle$ states

Since $|\Omega\rangle$ is the vacuum state whose energy is *assumed* to be equal to 0, we have

$$H\,|\Omega\rangle = 0 \quad \text{and} \quad \vec{P}\,|\Omega\rangle = \vec{0} \qquad \Longrightarrow \qquad \langle \Omega |\; e^{H\,t + i\,\vec{x}\cdot\vec{P}} \;=\; \langle \Omega |\; e^{0\,t + i\,\vec{x}\cdot\vec{0}} \;=\; \langle \Omega |$$

In the same manner, we have for the $|n;\, \vec{p}_n\rangle$ states

$$H\,|n;\, \vec{p}_n\rangle = E_n\; |n;\, \vec{p}_n\rangle \qquad \text{and} \qquad \vec{P}\,|n;\, \vec{p}_n\rangle = \vec{p}_n\; |n;\, \vec{p}_n\rangle$$

$$\Longrightarrow \qquad e^{-H\,t - i\,\vec{x}\cdot\vec{P}}\; |n;\, \vec{p}_n\rangle \;=\; e^{-E_n\,t - i\,\vec{x}\cdot\vec{p}_n}\; |n;\, \vec{p}_n\rangle$$

Return to the two-point correlation function

Using the space-time translational invariance on (A.2), we get

$$\tilde{C}_{12}(t,\vec{p}) = \sum_{\vec{x}}\sum_{n,\vec{p}_n} \frac{e^{i\vec{p}\cdot\vec{x}}}{(2\pi)^3\,(2E_n)}\,\langle\Omega|e^{Ht+i\vec{x}\cdot\hat{\vec{P}}}\,\mathcal{O}_1(0,\vec{0})\,e^{-Ht-i\vec{x}\cdot\hat{\vec{P}}}|n;\,\vec{p}_n\rangle\,\langle n;\,\vec{p}_n|\mathcal{O}_2^\dagger(0,\vec{0})|\Omega\rangle$$

Then the exponential operators act on the states so that

$$\begin{aligned}\tilde{C}_{12}(t,\,\vec{p}) &= \sum_{\vec{x}}\sum_{n,\vec{p}_n} \frac{e^{i\vec{p}\cdot\vec{x}}}{(2\pi)^3\,(2E_n)} e^{-E_n t - i\vec{x}\cdot\vec{p}_n}\,\langle\Omega|\mathcal{O}_1(0,\vec{0})|n;\,\vec{p}_n\rangle\,\langle n;\,\vec{p}_n|\mathcal{O}_2^\dagger(0,\vec{0})|\Omega\rangle \\ &= \sum_{n,\vec{p}_n} \frac{e^{-E_n t}}{(2\pi)^3\,(2E_n)}\,\langle\Omega|\mathcal{O}_1(0)|n;\,\vec{p}_n\rangle\,\langle n;\,\vec{p}_n|\mathcal{O}_2^\dagger(0)|\Omega\rangle\,\sum_{\vec{x}} e^{i(\vec{p}-\vec{p}_n)\cdot\vec{x}}\end{aligned}$$

The sum over $\vec{x}$ can now be done using

$$\sum_{\vec{x}} e^{i(\vec{p}-\vec{q})\cdot\vec{x}} = (2\pi)^3\,\delta_{\vec{p},\vec{q}}$$

which is the lattice definition of the Dirac function. Hence, our two-point correlation function reads

$$\tilde{C}_{12}(t,\,\vec{p}) = \sum_{n,\vec{p}_n} \frac{e^{-E_n t}}{(2\pi)^3\,(2E_n)}\,\langle\Omega|\mathcal{O}_1(0)|n;\,\vec{p}_n\rangle\,\langle n;\,\vec{p}_n|\mathcal{O}_2^\dagger(0)|\Omega\rangle\;(2\pi^3)\,\delta_{\vec{p},\vec{p}_n}$$

Finally, the sum over the momenta $\vec{p}_n$ can be computed and we arrive at

$$\boxed{\tilde{C}_{12}(t,\vec{p}) = \sum_n \frac{e^{-E_n t}}{2E_n}\,\langle\Omega|\mathcal{O}_1(0)|n;\vec{p}\rangle\,\langle n;\vec{p}|\mathcal{O}_2^\dagger(0)|\Omega\rangle} \quad \text{with} \quad \boxed{E_n = \sqrt{m_n^2+\vec{p}^{\,2}}}$$

For polarized states, we need to add the extra polarization index

$$\boxed{\tilde{C}_{12}(t,\,\vec{p}) = \sum_{n,\lambda_n} \frac{e^{-E_n t}}{2E_n}\,\langle\Omega|\mathcal{O}_1(0)|n;\,\lambda_n;\,\vec{p}\rangle\,\langle n;\,\lambda_n;\,\vec{p}|\mathcal{O}_2^\dagger(0)|\Omega\rangle} \quad \text{with} \quad \boxed{E_n = \sqrt{m_n^2+\vec{p}^{\,2}}}$$

Large time limit

In this limit, only the $n=0$ ground state survives

$$\boxed{\tilde{C}_{12}(t,\,\vec{p}) \xrightarrow{\text{large } t} \frac{e^{-E_0 t}}{2E_0}\,\langle\Omega|\mathcal{O}_1(0)|M(\vec{p})\rangle\,\langle M(\vec{p})|\mathcal{O}_2^\dagger(0)|\Omega\rangle} \tag{A.3}$$

where $|0;\vec{p}\rangle \equiv |M(\vec{p})\rangle$ denotes the ground state M of momentum $\vec{p}$.
When there is a polarization involved, the relation is

$$\boxed{\tilde{C}_{12}(t,\,\vec{p}) \xrightarrow{\text{large } t} \frac{e^{-E_0 t}}{2E_0}\sum_{\lambda}\langle\Omega|\mathcal{O}_1(0)|M(\lambda,\,\vec{p})\rangle\,\langle M(\lambda,\,\vec{p})|\mathcal{O}_2(0)^\dagger|\Omega\rangle} \tag{A.4}$$

where we have used the notation $|0;\, \lambda_0;\, \vec{p}\rangle \equiv |M(\lambda,\, \vec{p})\rangle$ for the ground state M of momentum $\vec{p}$ and polarization λ.

A.2 Energy extraction

Let us assume here that

$$\mathcal{O}_1(0) \;=\; \mathcal{O}_2(0) \;\equiv\; \mathcal{O}$$

Then, equation (A.3) becomes

$$\tilde{C}(t,\, \vec{p}) \;\xrightarrow{\text{large } t}\; \mathcal{Z}(\vec{p})\, e^{-E_0 t} \qquad \text{where} \qquad 2E_0\, \mathcal{Z}(\vec{p}) = |\, \langle \Omega|\mathcal{O}|M(\vec{p})\rangle\, |^2$$

which is the starting point for extracting the mass of the ground state having the quantum numbers of the operator $\mathcal{O}$ (by doing proper fits of $\tilde{C}(t,\, \vec{p} = \vec{0})$).
Similar expressions can be found with (A.4).

A.3 Decay constant for the vector case

Using two-point correlation functions, we can also extract decay constants. In the following, we will consider the case of the decay constant f_V of a vector meson M_V.

A.3.1 Definition and ingredients

By definition, the decay constant of a vector meson M_V is given by

$$\langle \Omega|V_\mu|M_V(\lambda,\, \vec{p})\rangle = \epsilon_\mu^{(\lambda)}(p)\, f_V\, m_V$$

where $p = (E_p, \vec{p})$ and $\epsilon_\mu^{(\lambda)}(p)$ is the polarization tensor which fullfills

$$\sum_\lambda \epsilon_\mu^{(\lambda)}(p)\, \epsilon_\nu^{*(\lambda)}(p) = \eta_{\mu\nu} - \frac{p_\mu p_\nu}{m^2} \qquad \text{(in minkowski space)}$$

From now on, we will work in the rest frame of the vector meson, which means that

$$E_0 = m_V \qquad \text{and} \qquad \vec{p} = \vec{0} \quad (i.e.\ p_i = 0)$$

and, for the space components of the polarization tensor

$$\begin{aligned} \sum_\lambda \epsilon_i^{(\lambda)}(\vec{0})\, \epsilon_j^{*(\lambda)}(\vec{0}) \;&=\; \eta_{ij} \qquad \text{(Minkowski Space)} \\ &=\; \delta_{ij} \qquad \text{(euclidean Space)} \end{aligned}$$

A.3.2 Decay constant extraction

Let us choose the operators

$$\mathcal{O}_1 \;=\; V_i \quad \text{and} \quad \mathcal{O}_2 \;=\; V_j \qquad (i \text{ and } j \text{ are spatial indices})$$

Then, in the rest frame of the vector meson, eq. (A.4) reads

$$\tilde{C}_{ij}(t,\vec{0}) \xrightarrow{\text{large } t} \frac{e^{-m_V t}}{2m_V} \sum_{\lambda} \langle \Omega | V_i(0) | M_V(\lambda,\vec{0}) \rangle \, \langle M_V(\lambda,\vec{0}) | V_j^{\dagger}(0) | \Omega \rangle$$

Substituting the definition of the decay constant, we get

$$\tilde{C}_{ij}(t,\vec{0}) \xrightarrow{\text{large } t} \frac{e^{-m_V t}}{2m_V} f_V^2 \, m_V^2 \underbrace{\sum_{\lambda} \epsilon_i^{(\lambda)}(\vec{0}) \, \epsilon_j^{*(\lambda)}(\vec{0})}_{\delta_{ij}}$$

Hence, if we compute the correlator $\tilde{C}_{ii}(t,\vec{0})$, we have the two following equivalent expressions

$$\begin{cases} \tilde{C}_{ii}(t,\vec{0}) \xrightarrow{\text{large } t} \dfrac{e^{-m_V t}}{2m_V} f_V^2 \, m_V^2 \\ \tilde{C}_{ii}(t,\vec{0}) \xrightarrow{\text{large } t} \dfrac{e^{-m_V t}}{2m_V} \displaystyle\sum_{\lambda} | \, \langle \Omega | V_i(0) | M_V(\lambda, \vec{p}=\vec{0}) \rangle \, |^2 \end{cases}$$

So we can extract the decay constant f_V through

$$\boxed{f_V \;=\; \frac{\sqrt{\mathcal{Z}_V}}{m_V}} \qquad \text{where} \qquad \boxed{\mathcal{Z}_V \;=\; \sum_{\lambda} | \, \langle \Omega | V_i(0) | M_V(\lambda, \vec{p}=\vec{0}) \rangle \, |^2}$$

The coefficient $\mathcal{Z}_V$ is obtained by fitting $\tilde{C}_{ii}(t,\vec{0})$ and the mass m_V by using the procedure described in the preceding paragraph.

A.4 Computing two-point correlation functions on the lattice

In this paragraph we describe how the pseudoscalar-pseudoscalar two-point correlation function $C_{PP}(t, \vec{p}=\vec{0})$ can be computed on the lattice using Dirac propagators.

A.4.1 Some useful relations

Here we gather the relations that will be used in our computation :

- *in the euclidean formalism*:

$$\bar{\psi} \;=\; \psi^{\dagger} \gamma_4 \qquad ; \qquad \gamma_5^{\dagger} \;=\; \gamma_5 \qquad ; \qquad \gamma_4^{\dagger} \;=\; \gamma_4 \qquad ; \qquad \{\gamma_5, \gamma_4\} \;=\; 0$$

- *Wick's theorem for Grassmann fermionic variables* : denoting by $G = D^{-1}$ the Dirac propagator (inverse of the Dirac operator), the theorem states

$$\begin{aligned} < \bar{\psi}_{i_1}\psi_{j_1}\cdots\bar{\psi}_{i_n}\psi_{j_n} > &= (-)^n < \psi_{j_1}\bar{\psi}_{i_1}\cdots\psi_{j_n}\bar{\psi}_{i_n} > \\ &= (-)^n \sum_{p\in\mathcal{P}(1,\ldots,n)} \varepsilon_p \, (G)_{j_{p_1}i_1} \, (G)_{j_{p_2}i_2} \cdots (G)_{j_{p_n}i_n} \end{aligned}$$

  where $\mathcal{P}(1,\ldots,n)$ is the set of permutations of $\{1,2,\ldots,n\}$, ε_p the signature of the permutation p and p_k the integer given by the application of the permutation p on the integer k.

  In practice, the index $i(j)$ represents the set (x,μ,a), that is (space-time position, Lorentz index, color index) respectively.

  As a simple consequence, we can notice that (for $n = 1$)

$$G^{ab}_{\mu\nu}(y;x) \; = < \psi^a_\mu(y)\,\bar{\psi}^b_\nu(x) > \qquad \text{(propagator from } x \text{ to } y\text{)}$$

- *factorization with respect to flavour* : in general, a quark field depends on the following indices

$$\psi^{a(f)}_\mu(x) \qquad \text{where} \qquad \begin{cases} \mu \; : \text{ Lorentz index} \\ a \; : \text{ color index} \\ f \; : \text{ flavor index} \\ x \; : \text{ space-time point} \end{cases}$$

  We then have the following property (flavor factorization)

$$\underbrace{< \cdots\cdots\cdots\cdots >}_{\text{contains } \psi^{(f_1)},\, \psi^{(f_2)} \text{ etc}} = \underbrace{< \cdots >}_{\psi^{(f_1)} \text{ only}} \underbrace{< \cdots >}_{\psi^{(f_2)} \text{ only}} \cdots$$

A.4.2 Description of the method

We are interested in the following two-point correlation function

$$\tilde{C}_{PP}(t,\vec{p}=0) = \sum_{\vec{x}} \langle\Omega|\mathcal{O}_1(t,\vec{x})\mathcal{O}_2^\dagger(0,\vec{0})|\Omega\rangle \tag{A.5}$$

with

$$\mathcal{O}_1(t,\vec{x}) = \mathcal{O}_2(t,\vec{x}) = \left(\bar{\psi}^{(1)}\gamma^5\psi^{(2)}\right)(t,\vec{x})$$

where (1) and (2) denote the flavor indices only.

Expression for $\mathcal{O}_2^\dagger$

We can compute $\mathcal{O}_2^\dagger$ directly from the expression of $\mathcal{O}_2$

$$\begin{aligned}
\mathcal{O}_2^\dagger &= \left[\bar{\psi}^{(1)}\gamma_5\psi^{(2)}\right] \qquad \text{(by definition)} \\
&= -\psi^{(2)\dagger}(\gamma_5)^\dagger(\bar{\psi}^{(1)})^\dagger \qquad \text{(exchange of 2 Grassmann variables)} \\
&= -\psi^{(2)\dagger}\gamma_5\gamma_4^\dagger\left(\left(\psi^{(1)^\dagger}\right)\right)^\dagger \qquad \text{(definition of } \bar{\psi}\text{)} \\
&= -\psi^{(2)\dagger}\gamma_5\gamma_4\gamma^{(1)} = +\psi^{(2)\dagger}\gamma_4\gamma_5\psi^{(1)} \qquad (\gamma \text{ algebra}) \\
&= \bar{\psi}^{(2)}\gamma_5\psi^{(1)} \qquad \text{(definition of } \bar{\psi} \text{ again)}
\end{aligned}$$

Treatment of $\tilde{C}_{PP}$

We can rewrite the equation (A.5) using the preceding expressions for $\mathcal{O}_1$ and $\mathcal{O}_2^\dagger$

$$\begin{aligned}
\tilde{C}_{PP}(t,\ \vec{p}=\vec{0}) &= \sum_{\vec{x}}\langle\Omega|\bar{\psi}^{(1)}(t,\vec{x})\gamma_5\psi^{(2)}(t,\vec{x})\bar{\psi}^{(2)}(0,\vec{0})\gamma_5\psi^{(1)}(0,\vec{0})|\Omega\rangle \\
&= \sum_{\vec{x}}\sum_{\mu,\nu,\rho,\sigma}\sum_{a,b}\langle\Omega|\bar{\psi}^{(1)}_{\mu,a}(t,\vec{x})(\gamma_5)_{\mu\nu}\bar{\psi}^{(2)}_{\nu a}(t,\vec{x})\bar{\psi}^{(2)}_{\rho b}(0,\vec{0})(\gamma_5)_{\rho\sigma}\psi^{(1)}_{\sigma b}(0,\vec{0})|\Omega\rangle \\
&\qquad\qquad \text{(with explicit indices)} \\
&= \sum_{\vec{x}}\sum_{\mu,\nu,\rho,\sigma}\sum_{a,b}(\gamma_5)_{\mu\nu}(\gamma_5)_{\rho\sigma}\,\langle\Omega|\bar{\psi}^{(1)}_{\mu a}(t,\vec{x})\psi^{(2)}_{\nu a}(t,\vec{x})\bar{\psi}^{(2)}_{\rho b}(0,\vec{0})\psi^{(1)}_{\sigma b}(0,\vec{0}|\Omega\rangle \\
&\qquad\qquad \text{(the } (\gamma_5)_{\mu\nu} \text{ are numbers now)} \\
&= -\sum_{\vec{x}}\sum_{\mu,\nu,\rho,\sigma}\sum_{a,b}(\gamma_5)_{\mu\nu}(\gamma_5)_{\rho\sigma}\,\langle\Omega|\psi^{(1)}_{\sigma b}(0,\vec{0})\bar{\psi}^{(1)}_{\mu a}(t,\vec{x})\psi^{(2)}_{\nu a}(t,\vec{x})\bar{\psi}^{(2)}_{\rho b}(0,\vec{0})|\Omega\rangle \\
&\qquad\qquad \text{(reordering of the anticommuting fields)} \\
&= -\sum_{\vec{x}}\sum_{\mu,\nu,\rho,\sigma}\sum_{a,b}(\gamma_5)_{\mu\nu}(\gamma_5)_{\rho\sigma}\,\langle\Omega|\psi^{(1)}_{\sigma b}(0,\vec{0})\bar{\psi}^{(1)}_{\mu a}(t,\vec{x})|\Omega\rangle\,\langle\Omega|\psi^{(2)}_{\nu a}(t,\vec{x})\bar{\psi}^{(2)}_{\rho b}(0,\vec{0})|\Omega\rangle \\
&\qquad\qquad \text{(flavor factorization)} \\
&= -\sum_{\vec{x}}\sum_{\mu,\nu,\rho,\sigma}\sum_{a,b}(\gamma_5)_{\mu\nu}(\gamma_5)_{\rho\sigma}G^{ba(1)}_{\sigma\mu}(0,\vec{0};t,\vec{x})G^{ab(2)}_{\nu\rho}(t,\vec{x};0,\vec{0}) \\
&\qquad\qquad \text{(definition of the Dirac propagator)} \\
&= -\sum_{\vec{x}}\sum_{\mu,\nu,\rho,\sigma}\sum_{a,b}G^{ab(2)}_{\nu\rho}(t,\vec{x};0,\vec{0})(\gamma_5)_{\rho\sigma}G^{ba(1)}_{\sigma\mu}(0,\vec{0};t,\vec{x})(\gamma_5)_{\mu\nu} \\
&\qquad\qquad \text{(final reordering)}
\end{aligned}$$

We can now recognize traces which run over color and Lorentz indices in the above sums

$$\boxed{\tilde{C}_{PP}(t,\vec{p}=\vec{0}) = -\sum_{\vec{x}} Tr\left[G^{(2)}(t,\vec{x};0,\vec{0})\gamma_5 G^{(1)}(0,\vec{0};t,\vec{x})\gamma_5\right]}$$

Comments

We need to know two types of Dirac propagators

$$\begin{cases} G^{(1)}(0,\vec{0};t,\vec{x}) & : \text{ any point on the lattice } \longrightarrow \ (0,\vec{0}) \\ G^{(2)}(t,\vec{x};0,\vec{0}) & : \ (0,\vec{0}) \ \longrightarrow \text{ any point on the lattice} \end{cases}$$

Apart from the flavor index, one propagator is the backward propagator of the other.
It is possible to avoid the computation on the lattice of a backward propagator if we already know the same propagator in the opposite direction. We have indeed something like the following

$$"\gamma_5 \, G \, \gamma_5 \ = \ G^{\dagger}"$$

i.e. with explicit indices

$$(\gamma_5)_{\mu\nu} \, G^{ab}_{\nu\rho}(y;x) \, (\gamma_5)_{\rho\sigma} \ = \ G^{*ba}_{\sigma\mu}(x;y)$$

Appendix B

Generalized Eigenvalue Problem

In this appendix, we will describe in greater detail the GEVP; in particular, we will focus on the "simple" GEVP, meaning that we are assuming that the contribution of the eigenstates $\{|n\rangle\}$ of the hamiltonian $\hat{H}$ having $n > N$ (where N is the dimension of the interpolating field basis we will use) can be neglected.

B.1 Unbounded time domain

In this section, the time variable is never bounded.

B.1.1 Hypotheses

In the following assume that

1. the eigenstates $\{|n\rangle\}$ of the hamiltonian $\hat{H}$ fullfill the following properties (definition, relativistic normalization and closure relation)

$$\hat{H}\,|n\rangle = E_n\,|n\rangle \qquad \left(E_n = \frac{\langle n|\hat{H}|n\rangle}{\langle n|n\rangle}\right)$$

as well as

$$\langle n|m\rangle = 2E_n\,\delta_{n,m} \qquad \text{and} \qquad \sum_n \frac{|n\rangle\,\langle n|}{2E_n} = \mathbb{1}$$

2. the relationship between the Schrödinger and the Heisenberg pictures reads

$$\mathcal{O}(t) = e^{\hat{H}t}\,\mathcal{O}(0)\,e^{-\hat{H}t} = e^{\hat{H}t}\,\hat{\mathcal{O}}\,e^{-\hat{H}t} \qquad \text{in the euclidean}$$

B.1.2 Nature of the correlation functions

Since the time coordinate is not bounded, we are going to work with correlators of the form

$$C_{ij}(t) = \sum_{n=1}^{N} \langle\Omega|\hat{\mathcal{O}}_i|n\rangle\,\langle n|\hat{\mathcal{O}}_j^\dagger|\Omega\rangle\,\frac{e^{-E_n t}}{2E_n} \qquad \text{with} \qquad 1 \leqslant i,j \leqslant N \tag{B.1}$$

where, as always, $|\Omega\rangle$ stands for the vacuum (zero energy). This equation is written in the rest frame of the system ($\vec{p} = \vec{0}$) and it has already been discussed in the Appendix A.

Changing the notation, we can write

$$\boxed{C_{ij}(t) = \sum_{n=1}^{N} (Z_n)_i \, (Z_n)_j^* \, \rho_n(t)} \tag{B.2}$$

where

$$\boxed{\rho_n(t) = e^{-E_n t}} \quad \text{as well as} \quad \boxed{(Z_n)_i = \frac{\langle \Omega | \hat{\mathcal{O}}_i | n \rangle}{\sqrt{2E_n}}} \quad \text{and} \quad \boxed{(Z_n)_j^* = \frac{\langle n | \hat{\mathcal{O}}_j^\dagger | \Omega \rangle}{\sqrt{2E_n}}}$$

B.1.3 Philosophy of the "simple" GEVP

Our goal is to solve

$$\boldsymbol{C}(t) \, \boldsymbol{v_n}(t, t_o) = \lambda_n(t, t_o) \, \boldsymbol{C}(t_o) \, \boldsymbol{v_n}(t, t_o) \tag{B.3}$$

where $\boldsymbol{C}$ is the $N \times N$ C_{ij} correlator square matrix and $\boldsymbol{v_n}$ the $N \times 1$ eigenstate column matrix.

(Z_n) dual basis

Let us introduce the set of *constant* vectors $\boldsymbol{u_n}$ which satisfy the following orthogonality property

$$(\boldsymbol{u_n}, \boldsymbol{Z_m}) = \delta_{nm} \qquad \text{where} \qquad (\boldsymbol{a}, \boldsymbol{b}) \stackrel{\text{def}}{=} \sum_i a_i^* b_i$$

About the scalar product

In the presence of an operator, this scalar product implies

$$\begin{cases} \hat{\mathcal{A}} = (\boldsymbol{u}, \hat{\boldsymbol{\mathcal{O}}}) = \sum_i u_i^* \hat{\mathcal{O}}_i \\ \hat{\mathcal{A}}^\dagger = (\boldsymbol{u}, \hat{\boldsymbol{\mathcal{O}}})^\dagger = \sum_i u_i \hat{\mathcal{O}}_i^\dagger \end{cases}$$

Solving the GEVP

Using eqs. (B.2) and (B.3), we get

$$\sum_{j=1}^{N} C_{ij}(t)(u_n)_j = \sum_{j,m=1}^{N} (Z_m)_i \, (Z_m)_j^* \, \rho_m(t)(u_n)_j = \sum_{m=1}^{N} \rho_m(t)(Z_m)_i \underbrace{\sum_{j=1}^{N} (Z_m)_j^* (u_n)_j}_{(\boldsymbol{Z_m}, \boldsymbol{u_n}) = \delta_{nm}} = \rho_n(t)(Z_n)_i$$

that is, in matrix notation $\boldsymbol{C}(t) \, \boldsymbol{u_n} = \rho_n(t) \boldsymbol{Z_n}$

Then,

$$\left.\begin{aligned} \boldsymbol{C}(t) \, \boldsymbol{u_n} &= \rho_n(t) \boldsymbol{Z_n} \\ \boldsymbol{C}(t_0) \, \boldsymbol{u_n} &= \rho_n(t_0) \boldsymbol{Z_n} \end{aligned}\right\} \quad \Longrightarrow \quad \boldsymbol{C}(t) \, \boldsymbol{u_n} = \frac{\rho_n(t)}{\rho_n(t_0)} \boldsymbol{C}(t_0) \, \boldsymbol{u_n}$$

The GEVP is solved if one chooses

$$\boxed{\lambda_n(t,t_0) = \frac{\rho_n(t)}{\rho_n(t_0)}} \qquad \text{as well as} \qquad \boxed{\boldsymbol{v_n}(t,t_0) = \alpha_n(t,t_0)\,\boldsymbol{u_n}} \qquad \text{since} \qquad \boldsymbol{v_n}(t,t_0) \propto \boldsymbol{u_n}$$

B.1.4 Consequences

Energy extraction

According to the relation giving $\rho_n(t)$, the eigenvalues $\lambda_n(t,t_0)$ are

$$\boxed{\lambda_n(t,t_o) = e^{-E_n(t-t_o)}}$$

The traditional way of extracting the energy E_n is to consider

$$E_n^{\text{eff}}(t,t_0) = -\frac{\partial \log \lambda_n(t,t_0)}{\partial t} = \log \frac{\lambda_n(t,t_0)}{\lambda_n(t+1,t_0)} \xrightarrow{\text{large } t} E_n$$

Orthogonality relations

In terms of the $\boldsymbol{u_n}$

$$(\boldsymbol{u_n},\boldsymbol{Z_m}) = \delta_{nm} \quad \text{and} \quad \boldsymbol{Z_n} = \frac{1}{\rho_n(t)}\boldsymbol{C}(t)\,\boldsymbol{u_n} \quad \Longrightarrow \quad \boxed{(\boldsymbol{u_n},\boldsymbol{C}(t)\,\boldsymbol{u_m}) = \rho_n(t)\,\delta_{nm}}$$

In terms of the $\boldsymbol{v_n}$, this gives

$$\boxed{(\boldsymbol{v_n}(t,t_0),\boldsymbol{C}(t)\,\boldsymbol{v_m}(t,t_0)) \;=\; |\alpha_n(t,t_0)|^2\,\rho_n(t)\,\delta_{nm}} \tag{B.4}$$

We also have

$$\left.\begin{aligned}(\boldsymbol{u_n},\boldsymbol{Z_m}) &= \delta_{nm}\\ \boldsymbol{v_n}(t,t_0) &= \alpha_n(t,t_0)\,\boldsymbol{u_n}\end{aligned}\right\} \quad \Longrightarrow \quad \boxed{\alpha_n(t,t_0) = (\boldsymbol{v_n}(t,t_0),\boldsymbol{Z_n})}$$

B.1.5 Creation operator $\hat{\mathcal{A}}_n^\dagger$ for the $|n\rangle$ eigenstate

Definition

If we define the following operator

$$\boxed{\hat{\mathcal{A}}_n = (\boldsymbol{u_n},\hat{\boldsymbol{\mathcal{O}}}) = \sum_{i=1}^{N}(u_n)_i^*\hat{\mathcal{O}}_i} \qquad \text{and then} \qquad \boxed{\hat{\mathcal{A}}_n^\dagger = (\boldsymbol{u_n},\hat{\boldsymbol{\mathcal{O}}})^\dagger = \sum_{i=1}^{N}(u_n)_i\hat{\mathcal{O}}_i^\dagger}$$

we have the following

$$\hat{\mathcal{A}}_n^\dagger |\Omega\rangle = \sum_{i=1}^{N} (u_n)_i \, \hat{\mathcal{O}}_i^\dagger |\Omega\rangle = \sum_{i=1}^{N}\sum_{m=1}^{N} (u_n)_i \frac{1}{2E_m} |m\rangle \underbrace{\langle m|\hat{\mathcal{O}}_i^\dagger|\Omega\rangle}_{\sqrt{2E_m}(Z_m)_i^*} = \sum_{m=1}^{N} \frac{1}{\sqrt{2E_m}} \underbrace{\left(\sum_{i=1}^{N}(u_n)_i \, (Z_m)_i^*\right)}_{\delta_{nm}} |m\rangle$$

$$\implies \quad \boxed{\hat{\mathcal{A}}_n^\dagger |\Omega\rangle = \frac{1}{\sqrt{2E_n}} |n\rangle}$$

which shows that $\hat{\mathcal{A}}_n^\dagger$ creates the energy eigenstate $|n\rangle$.

Consequences

We derive here a series of relations that will be usefull for the extraction of matrix elements on the lattice.

1. *First identity* :

$$\langle\Omega|\mathcal{A}_n(t)\,\mathcal{A}_n^\dagger(0)|\Omega\rangle = \underbrace{\langle\Omega|\, e^{Ht}}_{\langle\Omega|}\hat{\mathcal{A}}_n e^{-Ht}\,\hat{\mathcal{A}}_n^\dagger\,|\Omega\rangle = \left(\frac{1}{\sqrt{2E_n}}\right)^2\langle n|e^{-Ht}|n\rangle = e^{-E_n t}\frac{\langle n|n\rangle}{2E_n} = e^{-E_n t}$$

$$\implies \quad \boxed{\langle\Omega|\mathcal{A}_n(t)\,\mathcal{A}_n^\dagger(0)|\Omega\rangle = \rho_n(t)}$$

2. *Second identity* :

   Let us introduce an operator $\mathcal{P}(t)$ (which can be, or not, one of the operators $\mathcal{O}_i$). Then

$$\langle\Omega|\mathcal{P}(t)\,\mathcal{A}_n^\dagger(0)|\Omega\rangle = \frac{1}{\sqrt{2E_n}}\langle\Omega|\mathcal{P}(t)|n\rangle = \frac{1}{\sqrt{2E_n}}\langle\Omega|e^{Ht}\hat{\mathcal{P}}e^{-Ht}|n\rangle = \frac{1}{\sqrt{2E_n}}\langle\Omega|\hat{\mathcal{P}}e^{-Ht}|n\rangle$$

$$= \frac{e^{-E_n t}}{\sqrt{2E_n}}\langle\Omega|\hat{\mathcal{P}}|n\rangle = \frac{\rho_n(t)}{\sqrt{2E_n}}\langle\Omega|\hat{\mathcal{P}}|n\rangle \qquad \implies \qquad \boxed{\langle\Omega|\hat{\mathcal{P}}|n\rangle^{\text{eff}}(t) = \frac{\sqrt{2E_n}}{\rho_n(t)}\langle\Omega|\mathcal{P}(t)\,\mathcal{A}_n^\dagger(0)|\Omega\rangle}$$

   The effective matrix element $\langle\Omega|\hat{\mathcal{P}}|n\rangle^{\text{eff}}(t)$ tends to $\langle\Omega|\hat{\mathcal{P}}|n\rangle$ at large time.

3. *Master identities* :

   Combining both preceding identities, we arrive at

$$\boxed{\langle\Omega|\hat{\mathcal{P}}|n\rangle^{\text{eff}}(t) = \sqrt{\frac{2E_n}{\rho_n(t)}}\,\frac{\langle\Omega|\mathcal{P}(t)\,\mathcal{A}_n^\dagger(0)|\Omega\rangle}{\sqrt{\langle\Omega|\mathcal{A}_n(t)\,\mathcal{A}_n^\dagger(0)|\Omega\rangle}}}$$

   as well as $\quad \boxed{\langle\Omega|\hat{\mathcal{P}}|n\rangle^{\text{eff}}(t) = \sqrt{2E_n}\,\frac{\langle\Omega|\mathcal{P}(t)\,\mathcal{A}_n^\dagger(0)|\Omega\rangle}{\langle\Omega|\mathcal{A}_n(t)\,\mathcal{A}_n^\dagger(0)|\Omega\rangle}}$

B.1.6 Using the eigenvectors $v_n(t, t_0)$

Preliminary calculation

Some matrix elements of the operator $\mathcal{A}_n(t)$ can be rewritten in terms of the eigenstates $\boldsymbol{v_n}(t, t_0)$.
Firstly, we have

$$\langle\Omega|\mathcal{P}(t)\,\mathcal{A}_n^\dagger(0)|\Omega\rangle = \langle\Omega|\mathcal{P}(t)\,\hat{\mathcal{A}}_n^\dagger|\Omega\rangle = \langle\Omega|\mathcal{P}(t)\left(\sum_{i=1}^{N}(u_n)_i\hat{\mathcal{O}}_i^\dagger\right)|\Omega\rangle = \langle\Omega|\mathcal{P}(t)\left(\sum_{i=1}^{N}(u_n)_i\mathcal{O}_i^\dagger(0)\right)|\Omega\rangle$$

which means that

$$\langle\Omega|\mathcal{P}(t)\,\mathcal{A}_n^\dagger(0)|\Omega\rangle = \sum_{i=1}^{N}\langle\Omega|\mathcal{P}(t)\,\mathcal{O}_i^\dagger(0)|\Omega\rangle\;(u_n)_i = \frac{1}{\alpha_n(t,t_o)}\sum_{i=1}^{N}\langle\Omega|\mathcal{P}(t)\,\mathcal{O}_i^\dagger(0)|\Omega\rangle\;\big(v_n(t,t_o)\big)_i$$

where the last equality comes from the relation between $\boldsymbol{u_n}$ and $\boldsymbol{v_n}(t, t_o)$.
Then, combining the first identity with equation (B.4), we obtain[1]

$$\left.\begin{aligned}\langle\Omega|\mathcal{A}_n(t)\,\mathcal{A}_n^\dagger(0)|\Omega\rangle &= \rho_n(t)\\ (\boldsymbol{v_n}(t,t_0),\boldsymbol{C}(t)\,\boldsymbol{v_n}(t,t_0)) &= |\alpha_n(t,t_0)|^2\,\rho_n(t)\end{aligned}\right\}$$

$$\Longrightarrow\quad \langle\Omega|\mathcal{A}_n(t)\,\mathcal{A}_n^\dagger(0)|\Omega\rangle = \frac{1}{|\alpha_n(t,t_0)|^2}\,(\boldsymbol{v_n}(t,t_0),\boldsymbol{C}(t)\,\boldsymbol{v_n}(t,t_0)) \quad \text{(B.5)}$$

Determination of a matrix element $\langle\Omega|\hat{\mathcal{P}}|n\rangle$

Substituting equation (B.5) into the first of the master identities, we find

$$\langle\Omega|\hat{\mathcal{P}}|n\rangle^{\text{eff}}(t) = \sqrt{\frac{2E_n}{\rho_n(t)}}\,\frac{\sum_{i=1}^{N}\langle\Omega|\mathcal{P}(t)\,\mathcal{O}_i^\dagger(0)|\Omega\rangle\;\big(v_n(t,t_0)\big)_i}{\sqrt{(\boldsymbol{v_n}(t,t_0),\boldsymbol{C}(t)\,\boldsymbol{v_n}(t,t_0))}}$$

Then, with the particular expression of $\rho_n(t)$, we can express the prefactor in terms of the eigenvalues $\lambda_n(t, t_0)$. A possible choice is

$$\frac{1}{\sqrt{\rho_n(t)}} = e^{E_n t/2} = \sqrt{\frac{\lambda_n(t,t_o)}{\lambda_n(2t,t_o)}}$$

However, because of the distant times (t and $2t$), the signal deteriorates at large time. It is more clever to choose, for instance, another parameterization such as

$$\frac{1}{\sqrt{\rho_n(t)}} = e^{E_n t/2} = \left(\frac{\lambda_n(t,t_o)}{\lambda_n(t+1,t_o)}\right)^{t/2}$$

which uses neighboring times.

[1] A global phase for $\alpha_n(t, t_o)$ is still unknown…

Finally, we arrive at a possible expression for a matrix element of the type $\langle\Omega|\hat{\mathcal{P}}|n\rangle$ using only the eigensystem of the GEVP for the initial correlators $\boldsymbol{C}(t)$ and two-point correlations functions $\langle\Omega|\mathcal{P}(t)\,\mathcal{O}_i^\dagger(0)|\Omega\rangle$ according to

$$\boxed{\langle\Omega|\hat{\mathcal{P}}|n\rangle^{\text{eff}}(t) = \sqrt{2E_n}\left(\frac{\lambda_n(t,t_0)}{\lambda_n(t+1,t_0)}\right)^{t/2}\frac{\sum_{i=1}^{N}\langle\Omega|\mathcal{P}(t)\,\mathcal{O}_i^\dagger(0)|\Omega\rangle\,\big(v_n(t,t_0)\big)_i}{\sqrt{(\boldsymbol{v_n}(t,t_0),\boldsymbol{C}(t)\,\boldsymbol{v_n}(t,t_0))}}} \xrightarrow{\text{large } t} \langle\Omega|\hat{\mathcal{P}}|n\rangle$$

Note : the operators $\mathcal{O}_i$ are the ones used in the correlation matrix $\boldsymbol{C}(t)$.

B.2 Bounded time domain with $t \leftrightarrow T - t$ symmetry

We will consider here the effect of a time symmetry (not antisymmetry) $t \leftrightarrow T - t$.

B.2.1 A new temporal evolution of the operators

Because of the symmetry $t \leftrightarrow T - t$, the time evolution of the operators becomes

$$\mathcal{O}(t) = e^{\hat{H}t}\,\mathcal{O}(0)\,e^{-\hat{H}t} + e^{\hat{H}(T-t)}\,\mathcal{O}(0)\,e^{-\hat{H}(T-t)}$$

$$\implies \qquad \boxed{\mathcal{O}(t) = e^{\hat{H}t}\,\hat{\mathcal{O}}\,e^{-\hat{H}t} + e^{\hat{H}(T-t)}\,\hat{\mathcal{O}}\,e^{-\hat{H}(T-t)}} \tag{B.6}$$

B.2.2 Initial correlation functions

The correlators $C_{ij}(t)$ have to exhibit this symmetry so they have the following structure

$$C_{ij}(t) = \sum_{n=1}^{N}\langle\Omega|\hat{\mathcal{O}}_i|n\rangle\,\langle n|\hat{\mathcal{O}}_j^\dagger|\Omega\rangle\,\frac{2e^{-E_nT/2}}{2E_n}\cosh\left[E_n\left(\frac{T}{2}-t\right)\right] \qquad \text{with} \qquad 1 \leqslant i,j \leqslant N$$

We will then use the same notations as in the first section. The only difference will be the expression of $\rho_n(t)$ which is now

$$\boxed{\rho_n(t) = 2\,e^{-E_nT/2}\cosh\left[E_n\left(\frac{T}{2}-t\right)\right]}$$

B.2.3 GEVP and energy extraction

The GEVP is solved in the same manner as in the preceding case and the relation which gives the eigenvalues does not change. Hence

$$\lambda_n(t,t_o) = \frac{\rho_n(t)}{\rho_n(t_o)} \qquad \implies \qquad \boxed{\lambda_n(t,t_o) = \frac{\cosh\left[E_n\left(\frac{T}{2}-t\right)\right]}{\cosh\left[E_n\left(\frac{T}{2}-t_o\right)\right]}}$$

In order to extract the energy levels, we can consider

$$\boxed{E_n^{\text{eff}}(t,t_0) = \operatorname{arccosh}\left[\frac{\lambda_n(t+1,t_0)+\lambda_n(t-1,t_0)}{2\,\lambda_n(t,t_0)}\right]} \qquad \xrightarrow{\text{large } t} \; E_n$$

The eigenvectors v_n are also given by the same relations as in the first section.

B.2.4 Creation operator $\hat{\mathcal{A}}_n^\dagger$

The definition of $\hat{\mathcal{A}}_n^\dagger$ as well as its action on the vacuum $|\Omega\rangle$ are identical to those present in the first section.
The three identities which have been shown remain valid here, owing to the new relation (B.6) which gives the temporal evolution of the operator $\hat{\mathcal{A}}_n(t)$, provided we use the new expression of $\rho_n(t)$.
For instance, we have

$$\begin{aligned}
\langle\Omega|\mathcal{A}_n(t)\,\mathcal{A}_n^\dagger(0)|\Omega\rangle &= \underbrace{\langle\Omega|\,e^{Ht}}_{\langle\Omega|}\,\hat{\mathcal{A}}_n e^{-Ht}\,\hat{\mathcal{A}}_n^\dagger\,|\Omega\rangle + \underbrace{\langle\Omega|\,e^{H(T-t)}}_{\langle\Omega|}\,\hat{\mathcal{A}}_n e^{-H(T-t)}\,\hat{\mathcal{A}}_n^\dagger\,|\Omega\rangle \\
&= \left(\frac{1}{\sqrt{2E_n}}\right)^2 \times \left[\langle n|e^{-Ht}|n\rangle + \langle n|e^{-H(T-t)}|n\rangle\right] \\
&= (e^{-E_n t} + e^{-E_n(T-t)})\frac{\langle n|n\rangle}{2E_n} \quad \Longrightarrow \quad \boxed{\langle\Omega|\mathcal{A}_n(t)\,\mathcal{A}_n^\dagger(0)|\Omega\rangle = \rho_n(t)}
\end{aligned}$$

B.2.5 Using the eigenvectors $v_n(t,t_o)$

Our goal is to compute a matrix element of the type $\langle\Omega|\hat{\mathcal{P}}|n\rangle$.

First method

Owing to the transformation law (B.6), we still have

$$\langle\Omega|\hat{\mathcal{P}}|n\rangle^{\text{eff}}(t) = \sqrt{\frac{2E_n}{\rho_n(t)}}\,\frac{\sum_{i=1}^{N}\langle\Omega|\mathcal{P}(t)\,\mathcal{O}_i^\dagger(0)|\Omega\rangle\;\big(v_n(t,t_0)\big)_i}{\sqrt{(\boldsymbol{v_n}(t,t_0),\boldsymbol{C}(t)\,\boldsymbol{v_n}(t,t_0))}}$$

The difficult part is to obtain $\rho_n(t)$ from the results of the GEVP.
▶ A first possibility could be the following

1. cosh *factor of* $\rho_n(t)$:

$$\lambda_n(T/2,t_0) = \frac{1}{\cosh\left[E_n\left(\frac{T}{2}-t_0\right)\right]} \qquad \Longrightarrow \qquad \cosh\left[E_n\left(\frac{T}{2}-t\right)\right] = \frac{\lambda_n(t,t_0)}{\lambda_n(T/2,t_0)}$$

2. *$e^{-E_nT/2}$ term of $\rho_n(t)$* : with the help of the usual formulae, we write

$$\frac{\lambda_n(t+1,t_0)-\lambda_n(t-1,t_0)}{2\lambda_n(T/2,t_0)} = -\sinh(E_n)\,\sin\left[E_n\left(\frac{T}{2}-t\right)\right]$$

Hence

$$\begin{aligned} e^{-E_n(T/2-t)} &= \cosh\left[E_n\left(\frac{T}{2}-t\right)\right] - \sinh\left[E_n\left(\frac{T}{2}-t\right)\right] \\ &= \frac{\lambda_n(t,t_0)}{\lambda_n(T/2,t_0)} - \frac{1}{\sinh(E_n)}\,\frac{\lambda_n(t+1,t_0)-\lambda_n(t-1,t_o)}{2\lambda_n(T/2,t_0)} \end{aligned}$$

The $\sinh(E_n)$ term is accessible by using the relation which gives $E_n^{\text{eff}}(t,t_0)$ since

$$\sinh[\operatorname{arccosh}(x)] = \sqrt{x^2-1} \qquad \Longrightarrow \qquad \sinh(E_n) = \sqrt{\left[\frac{\lambda_n(t+1,t_0)+\lambda_n(t-1,t_0)}{2\,\lambda_n(t,t_0)}\right]^2 - 1}$$

which leads finally to

$$e^{-E_n(T/2-t)} = \frac{\lambda_n(t,t_0)}{\lambda_n(T/2,t_0)} - \frac{1}{\sqrt{\left[\frac{\lambda_n(t+1,t_0)+\lambda_n(t-1,t_0)}{2\,\lambda_n(t,t_0)}\right]^2 - 1}}\,\frac{\lambda_n(t+1,t_0)-\lambda_n(t-1,t_0)}{2\lambda_n(T/2,t_0)}$$

As a consequence, we would have at $t=0$

$$e^{-E_nT/2} = \frac{\lambda_n(0,t_0)}{\lambda_n(T/2,t_0)} - \frac{1}{\sqrt{\left[\frac{\lambda_n(1,t_0)+\lambda_n(-1,t_0)}{2\,\lambda_n(0,t_0)}\right]^2 - 1}}\,\frac{\lambda_n(1,t_0)-\lambda_n(-1,t_0)}{2\lambda_n(T/2,t_0)}$$

and the $t=-1$ point would not be absurd because of the symmetry of $\lambda_n(t,t_0)$ around $T/2$.

3. *Final expression* : gathering everything, one finds

$$\rho_n(t) = 2\left[\frac{\lambda_n(0,t_0)}{\lambda_n(T/2,t_0)} - \frac{1}{\sqrt{\left[\frac{\lambda_n(1,t_0)+\lambda_n(-1,t_0)}{2\,\lambda_n(0,t_0)}\right]^2 - 1}}\,\frac{\lambda_n(1,t_0)-\lambda_n(-1,t_0)}{2\lambda_n(T/2,t_0)}\right]\frac{\lambda_n(t,t_0)}{\lambda_n(T/2,t_0)}$$

However, numerically, this method might not be as practical as expected because there appears to be a problem with $\lambda_n(T/2,t_0)$ as $T/2$ is a singularity, coming from the symmetry $t \leftrightarrow T-t$, which renders this eigenvalue very noisy.

► A second possibility, which avoids the problem mentioned above, could be

1. start from the asymptotic value of E_n obtained from the λ_n method;
2. this E_n is then used in the original, non transformed expression of $\rho_n(t)$;
3. $\langle\Omega|\hat{\mathcal{P}}|n\rangle^{\text{eff}}(t)$ is finally deduced from the corresponding initial relation.

Second method

Another idea would be to substitute, in the second of the master identities, the expressions of the matrix elements written in terms of the eigenvalues

$$\langle\Omega|\hat{\mathcal{P}}|n\rangle^{\text{eff}}(t) \;=\; \sqrt{2E_n}\,\frac{\langle\Omega|\mathcal{P}(t)\,\mathcal{A}_n^\dagger(0)|\Omega\rangle}{\langle\Omega|\mathcal{A}_n(t)\,\mathcal{A}_n^\dagger(0)|\Omega\rangle} \;=\; \alpha_n(t,t_0)\,\sqrt{2E_n}\,\frac{\sum_{i=1}^{N}\langle\Omega|\mathcal{P}(t)\,\mathcal{O}_i^\dagger(0)|\Omega\rangle\;\big(v_n(t,t_0)\big)_i}{(\boldsymbol{v_n}(t,t_0),\boldsymbol{C}(t)\,\boldsymbol{v_n}(t,t_0))}$$

The factor $\alpha_n(t,t_0o)$ can be obtained in the following way

1. We know that the double projected correlator is

$$(\boldsymbol{v_n}(t,t_0),\boldsymbol{C}(t)\,\boldsymbol{v_n}(t,t_0)) = |\alpha_n(t,t_0)|^2\,\rho_n(t) \qquad \text{with} \qquad \rho_n(t) = 2\,e^{-E_nT/2}\cosh\left[E_n\left(\frac{T}{2}-t\right)\right]$$

2. We use the large time energy E_n computed from the eigenvalues.

3. We study the ratio

$$R_n(t,t_0) = \frac{(\boldsymbol{v_n}(t,t_0),\boldsymbol{C}(t)\,\boldsymbol{v_n}(t,t_0))}{2\,e^{-E_nT/2}\cosh\left[E_n\left(\frac{T}{2}-t\right)\right]}$$

   If $R_n(t,t_0)$ is roughly constant, then α_n will not depend on the time, and, apart from a phase factor, $\alpha_n = \sqrt{R_n}$.

   If not, we need to extract $\alpha_n(t,t_0)$ for each value of t.

Comments on $(\boldsymbol{v_n}(t,t_o),\boldsymbol{C}(t)\,\boldsymbol{v_n}(t,t_o))$

The coefficients $\alpha_n(t,t_0)$ are used to characterize the normalisation of the eigenvectors $\boldsymbol{v_n}(t,t_0)$. So one choose to normalize them to 1

$$(\boldsymbol{v_n}(t,t_o),\boldsymbol{C}(t_0)\,\boldsymbol{v_n}(t,t_o)) = 1$$

Hence, we obtain

$$(\boldsymbol{v_n}(t,t_0),\boldsymbol{C}(t_0)\,\boldsymbol{v_n}(t,t_0)) = |\alpha_n(t_0,t_0)|^2\,\rho_n(t_0) = 1 \qquad\Longrightarrow\qquad |\alpha_n(t_0,t_0)|^2 = \frac{1}{\rho_n(t_0)} \tag{B.7}$$

If the coefficients $\alpha_n(t,t_0)$ do not depend on t, then we can write

$$(\boldsymbol{v_n}(t,t_0),\boldsymbol{C}(t)\,\boldsymbol{v_n}(t,t_0)) = \underbrace{|\alpha_n(t,t_o)|^2}_{|\alpha_n(t_0,t_0)|^2}\,\rho_n(t) = \frac{\rho_n(t)}{\rho_n(t_0)} \qquad\Longrightarrow\qquad \boxed{(\boldsymbol{v_n}(t,t_0),\boldsymbol{C}(t)\,\boldsymbol{v_n}(t,t_0)) = \lambda_n(t,t_0)}$$

which would greatly simplify the numerical implementation.
Notice also that, assuming again the time independance of the $\alpha_n(t,t_0)$, eq. (B.7) provides an alternative expression for $\alpha_n(t,t_0)$.

B.2.6 A word of caution

When the operator $\mathcal{P}(t)$ does not belong to the operator basis $\mathcal{O}_i(t)$ used to solve the GEVP, it can happen that the correlators of the type $\langle\Omega|\mathcal{P}(t)\,\mathcal{O}_i^\dagger(0)|\Omega\rangle$ are antisymmetrical with respect to the transformation $t \leftrightarrow T-t$. As a consequence, they exhibit a sinh temporal dependency and the extraction of the matrix element $\langle\Omega|\hat{\mathcal{P}}|n\rangle$ is slightly different.

1. The antisymmetry brings a new time evolution to the operators

$$\mathcal{O}(t) = e^{\hat{H}t}\,\mathcal{O}(0)\,e^{-\hat{H}t} - e^{\hat{H}(T-t)}\,\mathcal{O}(0)\,e^{-\hat{H}(T-t)}$$

$$\Longrightarrow \qquad \boxed{\mathcal{O}(t) = e^{\hat{H}t}\,\hat{\mathcal{O}}\,e^{-\hat{H}t} - e^{\hat{H}(T-t)}\,\hat{\mathcal{O}}\,e^{-\hat{H}(T-t)}}$$

2. We can then write

$$\begin{aligned}\langle\Omega|\mathcal{P}(t)\,\mathcal{A}_n^\dagger(0)|\Omega\rangle &= \frac{1}{\sqrt{2E_n}}\,\langle\Omega|\mathcal{P}(t)|n\rangle = \frac{1}{\sqrt{2E_n}}\,\langle\Omega|e^{Ht}\hat{\mathcal{P}}e^{-Ht} - e^{\hat{H}(T-t)}\,\hat{\mathcal{P}}\,e^{-\hat{H}(T-t)}|n\rangle \\ &= \frac{1}{\sqrt{2E_n}}\,\langle\Omega|\hat{\mathcal{P}}e^{-Ht}|n\rangle - \frac{1}{\sqrt{2E_n}}\,\langle\Omega|\hat{\mathcal{P}}e^{-H(T-t)}|n\rangle \\ &= \frac{e^{-E_nt} - e^{-E_n(T-t)}}{\sqrt{2E_n}}\,\langle\Omega|\hat{\mathcal{P}}|n\rangle \equiv \frac{\sigma_n(t)}{\sqrt{2E_n}}\,\langle\Omega|\hat{\mathcal{P}}|n\rangle\end{aligned}$$

$$\Longrightarrow \qquad \langle\Omega|\hat{\mathcal{P}}|n\rangle^{\text{eff}}(t) = \frac{\sqrt{2E_n}}{\sigma_n(t)}\,\langle\Omega|\mathcal{P}(t)\,\mathcal{A}_n^\dagger(0)|\Omega\rangle$$

$$\text{with} \qquad \boxed{\sigma_n(t) = 2\,e^{-E_nT/2}\sinh\left[E_n\left(\frac{T}{2}-t\right)\right]}$$

3. With this dependency, the starting expressions of the first and the second method of the preceding paragraph now read

$$\boxed{\langle\Omega|\hat{\mathcal{P}}|n\rangle^{\text{eff}}(t) = \sqrt{2E_n}\,\frac{\sqrt{\rho_n(t)}}{\sigma_n(t)}\,\frac{\sum_{i=1}^{N}\langle\Omega|\mathcal{P}(t)\,\mathcal{O}_i^\dagger(0)|\Omega\rangle\,\left(v_n(t,t_o)\right)_i}{\sqrt{(\boldsymbol{v_n}(t,t_o),\boldsymbol{C}(t)\,\boldsymbol{v_n}(t,t_o))}}}$$

as well as

$$\boxed{\langle\Omega|\hat{\mathcal{P}}|n\rangle^{\text{eff}}(t) = \alpha_n(t,t_o)\,\sqrt{2E_n}\,\frac{\rho_n(t)}{\sigma_n(t)}\,\frac{\sum_{i=1}^{N}\langle\Omega|\mathcal{P}(t)\,\mathcal{O}_i^\dagger(0)|\Omega\rangle\,\left(v_n(t,t_o)\right)_i}{(\boldsymbol{v_n}(t,t_o),\boldsymbol{C}(t)\,\boldsymbol{v_n}(t,t_o))}}$$

4. Finally, the treatment of these relations is identical to the one encountered with the correlators $\langle\Omega|\mathcal{P}(t)\,\mathcal{O}_i^\dagger(0)|\Omega\rangle$ symmetrical with respect to $t \leftrightarrow T-t$.

Appendix C

Pedestrian Quark Model Treatment

In this chapter, we discuss the behaviour of some specific operators used in the GEVP. We have noticed that, in the literature the extraction of the mass of a η_c state relies on correlators of the type

$$C_{ij}(t) = \sum_{ij} \langle [\bar{c}\gamma_5\gamma_i D_i c](t)\, [\bar{c}\gamma_5\gamma_j D_j c](0)\rangle \qquad \text{with } D_i \text{ the derivative in the } i \text{ direction}$$

which produces a very noisy correlator (very small numbers whose signs even change from time to time). However, if one chooses

$$C_{ij}(t) = \sum_{ij} \langle [\bar{c}\gamma_0\gamma_5\gamma_i D_i c](t)\, [\bar{c}\gamma_0\gamma_5\gamma_j D_j c](0)\rangle$$

then we obtain a very good signal. Since the only difference is the insertion of a γ_0 matrix (γ_4 in the euclidean), we would like to understand why this happens, and if this is a systematic behavior. In order to do so, we will use a naïve quark model framework and study the effect of the γ_0 insertion for 2 different operators.

C.1 The Quark Model

We are dealing with a $c\bar{c}$ charmonium state. So, the c quark will be described by a Dirac spinor of type u (which will be denoted by the same letter c later on) while the $\bar{c}$ antiquark by a Dirac spinor of type $\bar{v}$ (which will be also denoted by $\bar{c}$). Hence, we first need to express $\bar{v}$ ($\bar{c}$) in terms of u (c).
The spinor v can be interpreted as the charge conjugate of u so we have

$$v = \mathcal{C}(\bar{u})^T$$

where $\mathcal{C}$ is the charge conjugation matrix. In the Dirac representation, this matrix is written

$$\mathcal{C} = i\gamma^2\gamma^0 = -i\gamma^0\gamma^2$$

with

$$\gamma^0 = \begin{pmatrix} I & 0 \\ 0 & -I \end{pmatrix}, \qquad \text{and} \qquad \gamma^2 = \begin{pmatrix} 0 & \sigma_2 \\ -\sigma_2 & 0 \end{pmatrix}$$

where σ_2 is one of the Pauli matrices.
Explicitely we obtain

$$v = i\gamma^2\gamma^0(u^\dagger\gamma^0)^T = i\gamma^2\gamma^0(\gamma^0)^T(u^\dagger)^T = i\gamma^2\gamma^0\gamma^0u^* \quad \Longrightarrow \quad v = i\gamma^2u^*$$

which leads to

$$\bar{v} = v^\dagger\gamma^0 = -i(u^*)^\dagger(\gamma^2)^\dagger\gamma^0 = -i(u^*)^\dagger(\gamma^0\gamma^2\gamma^0)\gamma^0 \quad \Longrightarrow \quad \bar{v} = -i(u^*)^\dagger\gamma^0\gamma^2$$

We can now turn to the calculation of $\bar{c}(\vec{p}_{\bar{c}})$ where $\vec{p}_{\bar{c}}$ is the $\bar{c}$ momentum.
Working in a quark model, we decompose the $c(\vec{p})$ spinor into the small and large components at first order according to

$$c(\vec{p}) = \begin{pmatrix} c_1 \\ c_2 = \left(\dfrac{\vec{\sigma}\cdot\vec{p}}{2m}\right)c_1 \end{pmatrix}$$

Then, we have

$$\begin{aligned}
\bar{c}(\vec{p}_{\bar{c}}) &= -i(c^*)^\dagger\gamma^0\gamma^2 \\
&= -i\begin{pmatrix}(c_1^*)^\dagger & (c_1^*)^\dagger\dfrac{(\vec{\sigma}^*)^\dagger\cdot\vec{p}_{\bar{c}}}{2m_c}\end{pmatrix}\begin{pmatrix}I & 0\\ 0 & -I\end{pmatrix}\begin{pmatrix}0 & \sigma_2\\ -\sigma_2 & 0\end{pmatrix} \\
&= -i\begin{pmatrix}(c_1^*)^\dagger\dfrac{\vec{\sigma}^T\cdot\vec{p}_{\bar{c}}}{2m_c}\sigma_2 & (c_1^*)^\dagger\sigma_2\end{pmatrix}
\end{aligned}$$

Finally, let us note that

$$\begin{cases} \vec{\sigma}\cdot\vec{p} = \sigma_1p_1 + \sigma_2p_2 + \sigma_3p_3 \\ \vec{\sigma}^T\cdot\vec{p} = \sigma_1p_1 - \sigma_2p_2 + \sigma_3p_3 = \vec{\sigma}\cdot\vec{p} - 2\sigma_2p_2 \end{cases} \tag{C.1}$$

C.2 Contribution of the chosen different operators

C.2.1 Operator $\bar{c}\gamma_5 c$

Let us assume from now on that the charmonium is at rest. Then $\vec{p}_c = -\vec{p}_{\bar{c}} \equiv \vec{p}$ so that

$$\begin{aligned}
\bar{c}\gamma_5 c &= -i\begin{pmatrix}-(c_1^*)^\dagger\dfrac{\vec{\sigma}^T\cdot\vec{p}}{2m_c}\sigma_2 & (c_1^*)^\dagger\sigma_2\end{pmatrix}\begin{pmatrix}0 & I\\ I & 0\end{pmatrix}\begin{pmatrix}c_1\\ \dfrac{\vec{\sigma}\cdot\vec{p}}{2m_c}c_1\end{pmatrix} \\
&= -ic_1^T\sigma_2c_1 + ic_1^T\frac{\vec{\sigma}^T\cdot\vec{p}}{2m_c}\sigma_2\frac{\vec{\sigma}\cdot\vec{p}}{2m_c}c_1
\end{aligned}$$

Using (C.1), we are led to

$$\begin{aligned}(\vec{\sigma}^T\cdot\vec{p})\sigma_2(\vec{\sigma}\cdot\vec{p}) &= (\vec{\sigma}\cdot\vec{p})\sigma_2(\vec{\sigma}\cdot\vec{p}) - 2p_2(\vec{\sigma}\cdot\vec{p})\\ &= (\vec{\sigma}\cdot\vec{p})[-(\vec{\sigma}\cdot\vec{p})\sigma_2 + 2p_2] - 2p_2(\vec{\sigma}\cdot\vec{p})\\ &= -(\vec{\sigma}\cdot\vec{p})^2\sigma_2 = -\vec{p}^2\sigma_2\end{aligned}$$

because $\sigma_2^2 = I$ and $\sigma_2\sigma_i = -\sigma_i\sigma_2 + 2\delta_{i,2}I$.
Finally,

$$\boxed{\bar{c}\gamma_5 c = -ic_1^T\left(1+\frac{\vec{p}^2}{4m_c^2}\right)\sigma_2 c_1} \tag{C.2}$$

C.2.2 Operator $\bar{c}\gamma_5\gamma_0 c$

With the same assumptions as before, we have

$$\bar{c}\gamma_5\gamma_0 c = -i\begin{pmatrix}-(c_1^*)^\dagger\dfrac{\vec{\sigma}^T\cdot\vec{p}}{2m_c} & (c_1^*)^\dagger\sigma_2\end{pmatrix}\begin{pmatrix}0 & I\\ I & 0\end{pmatrix}\begin{pmatrix}I & 0\\ 0 & -I\end{pmatrix}\begin{pmatrix}c_1\\ \dfrac{\vec{\sigma}\cdot\vec{p}}{2m_c}c_1\end{pmatrix}$$

$$= -ic_1^T\sigma_2 c_1 - ic_1^T\left(1-\frac{\vec{p}^2}{2m_c^2}\right)\sigma_2 c_1$$

That is

$$\boxed{\bar{c}\gamma_5\gamma_0 c = -ic_1^T\left(1-\frac{\vec{p}^2}{4m_c^2}\right)\sigma_2 c_1} \tag{C.3}$$

C.2.3 Operator $\bar{c}\gamma_5\gamma_i D_i c$

In the Dirac representation

$$\gamma_5\gamma_i = \begin{pmatrix}0 & I\\ I & 0\end{pmatrix}\begin{pmatrix}0 & \sigma_i\\ -\sigma_i & 0\end{pmatrix} = \begin{pmatrix}-\sigma_i & 0\\ 0 & \sigma_i\end{pmatrix}$$

Hence, once again with the same assumptions

$$\bar{c}\gamma_5\gamma_i D_i c = -i\begin{pmatrix}-(c_1^*)^\dagger\dfrac{\vec{\sigma}^T\cdot\vec{p}}{2m_c}\sigma_2 & (c_1^*)^\dagger\sigma_2\end{pmatrix}\begin{pmatrix}-\sigma_i & 0\\ 0 & \sigma_i\end{pmatrix}D_i\begin{pmatrix}c_1\\ \dfrac{\vec{\sigma}\cdot\vec{p}}{2m_c}c_1\end{pmatrix} \qquad \text{where } D_i \rightsquigarrow ip_i$$

$$= \begin{pmatrix}-(c_1^*)^T\dfrac{\vec{\sigma}^T\cdot\vec{p}}{2m_c}\sigma_2 & (c_1^*)^\dagger\sigma_2\end{pmatrix}\begin{pmatrix}-\sigma_i c_1\\ \sigma_i\dfrac{\vec{\sigma}\cdot\vec{p}}{2m_c}c_1\end{pmatrix}p_i$$

$$= c_1^T\left(\frac{\vec{\sigma}^T\cdot\vec{p}}{2m_c}\sigma_2\sigma_i + \sigma_2\sigma_i\frac{\vec{\sigma}\cdot\vec{p}}{2m_c}\right)c_1 p_i$$

However

$$\begin{cases} (\vec{\sigma}^T \cdot \vec{p})\sigma_2\sigma_i = [(\vec{\sigma} \cdot \vec{p}) - 2\sigma_2 p_2]\sigma_2\sigma_i = (\vec{\sigma} \cdot \vec{p})\sigma_2\sigma_i - 2p_2\sigma_i \\ \sigma_i(\vec{\sigma} \cdot \vec{p}) = \sigma_i\sigma_j p_j = (\sigma_j\sigma_i + 2\delta_{ij})p_j = -(\vec{\sigma} \cdot \vec{p})\sigma_i + 2p_i \\ (\vec{\sigma} \cdot \vec{p})\sigma_2(\vec{\sigma} \cdot \vec{p}) = -\vec{p}^2\sigma_2 + 2p_2(\vec{\sigma} \cdot \vec{p}) \end{cases}$$

which leads to

$$(\vec{\sigma}^T \cdot \vec{p})\sigma_2\sigma_i + \sigma_2\sigma_i(\vec{\sigma} \cdot \vec{p}) = 2(\vec{\sigma} \cdot \vec{p})\sigma_2\sigma_i + 2p_i\sigma_2 - 4p_2\sigma_i$$

So we can compute the following contraction

$$\begin{aligned} \sum_i [(\vec{\sigma}^T \cdot \vec{p})\sigma_2\sigma_i + \sigma_2\sigma_i(\vec{\sigma} \cdot \vec{p})]p_i &= 2(\vec{\sigma} \cdot \vec{p})\sigma_2(\vec{\sigma} \cdot \vec{p}) + 2\vec{p}^2\sigma_2 - 4p_2(\vec{\sigma} \cdot \vec{p}) \\ &= 2[-\vec{p}^2\sigma_2 + 2p_2(\vec{\sigma} \cdot \vec{p})] + 2\vec{p}^2\sigma_2 - 4p_2(\vec{\sigma} \cdot \vec{p}) \\ &= 0 \end{aligned}$$

and we arrive at

$$\boxed{\sum_i \bar{c}\gamma_5\gamma_i D_i c = 0}$$

For each value of i, the corresponding component is explicitely

$$\begin{cases} \bar{c}\gamma_5\gamma_1 D_1 c &= c_1^T \dfrac{-ip_1p_3 - p_1p_2\sigma_1}{m_c} c_1 \\ \bar{c}\gamma_5\gamma_2 D_2 c &= c_1^T \dfrac{p_1p_2\sigma_1 + p_2p_3\sigma_3}{m_c} c_1 \\ \bar{c}\gamma_5\gamma_3 D_3 c &= c_1^T \dfrac{ip_1p_3 - p_2p_3\sigma_3}{m_c} c_1 \end{cases} \tag{C.4}$$

C.2.4 Operator $\bar{c}\gamma_0\gamma_5\gamma_i D_i c$

In this case, and still in the Dirac representation

$$\gamma_0\gamma_5\gamma_i = \begin{pmatrix} I & 0 \\ 0 & -I \end{pmatrix}\begin{pmatrix} 0 & I \\ I & 0 \end{pmatrix}\begin{pmatrix} 0 & \sigma_i \\ -\sigma_i & 0 \end{pmatrix} = \begin{pmatrix} -\sigma_i & 0 \\ 0 & -\sigma_i \end{pmatrix}$$

The operator then reads

$$\begin{aligned} \bar{c}\gamma_0\gamma_5\gamma_i D_i c &= -i\left(-(c_1^*)^\dagger \frac{\vec{\sigma} \cdot \vec{p}}{2m_c}\sigma_2 \;\; (c_1^*)^\dagger\sigma_2\right)\begin{pmatrix} -\sigma_i & 0 \\ 0 & -\sigma_i \end{pmatrix} D_i \begin{pmatrix} c_1 \\ \dfrac{\vec{\sigma} \cdot \vec{p}}{2m_c} c_1 \end{pmatrix} \\ &= \left(-(c_1^*)^\dagger \frac{\vec{\sigma} \cdot \vec{p}}{2m_c}\sigma_2 \;\; (c_1^*)^\dagger\sigma_2\right)\begin{pmatrix} -\sigma_i c_1 \\ -\sigma_i \dfrac{\vec{\sigma} \cdot \vec{p}}{2m_c} c_1 \end{pmatrix} p_i \qquad (D_i \rightsquigarrow ip_i) \\ &= c_1^T\left(\frac{\vec{\sigma} \cdot \vec{p}}{2m_c}\sigma_2\sigma_i - \sigma_2\sigma_i\frac{\vec{\sigma} \cdot \vec{p}}{2m_c}\right) c_1 p_i \end{aligned}$$

Using some previous intermediary steps, we have

$$(\vec{\sigma}^T\cdot\vec{p})\sigma_2\sigma_i-\sigma_2\sigma_i(\vec{\sigma}\cdot\vec{p})=-2p_i\sigma_2 \qquad\Longrightarrow\qquad \sum_i[(\vec{\sigma}^T\cdot\vec{p})\sigma_2\sigma_i-\sigma_2\sigma_i(\vec{\sigma}\cdot\vec{p})]p_i=-2\vec{p}^2\sigma_2$$

leading finally to

$$\boxed{\sum_i \bar{c}\gamma_0\gamma_5\gamma_i D_i c=-c_1^T\frac{\vec{p}^2}{m_c}\sigma_2 c_1} \tag{C.5}$$

C.3 Comments

C.3.1 The $\bar{c}\gamma_5 c$ vs $\bar{c}\gamma_5\gamma_0 c$ case

Let us consider the correlator

$$\langle\Omega|\bar{c}(0)\gamma_5\begin{pmatrix}1\\ \gamma_0\end{pmatrix}c(0)\,\bar{c}(t)\gamma_5\begin{pmatrix}1\\ \gamma_0\end{pmatrix}c(t)|\Omega\rangle$$

and add some further assumptions in our treatment

1. the charmonium is a η_c ground state whose wave function has the form $\psi(\vec{p}^2)\otimes\chi^0(s)$ and possesses the right integrability properties;
2. $\psi(\vec{p}^2)$ is supposed to be real;
3. the spin part can be written according to

$$\chi^0(s)\;=\;\frac{-{c_1^+}^\dagger c_1^- + {c_1^-}^\dagger c_1^+}{\sqrt{2}}\;=\;\frac{-i\,c_1^\dagger\sigma_2\,c_1}{\sqrt{2}}\qquad\text{where}\qquad c_1=\begin{pmatrix}c_1^+\\ c_1^-\end{pmatrix}$$

4. the creation operators produce η_c excitations which are suppressed in time.

By using the relations (C.2) and (C.3), we can then deduce

$$\langle\Omega|\bar{c}(0)\gamma_5\begin{pmatrix}1\\ \gamma_0\end{pmatrix}c(0)|\eta_c\rangle\;=\;\sqrt{2}\int \mathrm{d}^3p\,\psi(\vec{p}^2)\Big[1\pm\frac{\vec{p}^2}{4m_c^2}\Big]$$

and

$$\langle\Omega|\bar{c}(0)\gamma_5\begin{pmatrix}1\\ \gamma_0\end{pmatrix}c(0)\bar{c}(t)\gamma_5\begin{pmatrix}1\\ \gamma_0\end{pmatrix}c(t)|\Omega\rangle\;=\;2\left\{\int \mathrm{d}^3p\,\psi(\vec{p}^2)\Big[1\pm\frac{\vec{p}^2}{4m_c^2}\Big]\right\}^2\exp(-m_{\eta_c}t)$$

This last equation can be cast into the following form

$$\frac{\langle\Omega|\bar{c}(0)\gamma_5\gamma_0 c(0)\,\bar{c}(t)\gamma_5\gamma_0 c(t)|\Omega\rangle}{\langle\Omega|\bar{c}(0)\gamma_5 c(0)\,\bar{c}(t)\gamma_5 c(t)|\Omega\rangle}\;=\;\left[\frac{1-\langle p_c^2\rangle/(4\,m_c^2)}{1+\langle p_c^2\rangle/(4\,m_c^2)}\right]^2\qquad\text{where}\qquad\langle p_c^2\rangle\;=\;\frac{\int \mathrm{d}^3p\,\vec{p}^{\,2}\,\psi(\vec{p}^2)}{\int \mathrm{d}^3p\,\psi(\vec{p}^2)}$$

In order to quantify these contributions, let us use equation (4.152) of [196].

$$\psi_0(\vec{p}^{\,2}) \;=\; N_0 \,\exp\left(-\frac{1}{8}\,R^2\,\vec{p}^{\,2}\right) \qquad \text{with} \qquad \vec{p} = \vec{p}_q - \vec{p}_{\bar{q}}$$

A typical value of the meson radius R^2 of $12\,\text{GeV}^{-2}$ is given for light quarks but we can assume that the size of a $c\bar{c}$ meson is not too different from the one of a light meson, if not larger.
Since we use here $\vec{p}_c = -\vec{p}_{\bar{c}}$, we have

$$\psi_0(\vec{p}_c^{\,2}) \;=\; N_0 \,\exp\left(-\frac{1}{2}\,R^2\,\vec{p}_c^{\,2}\right) \quad\Longrightarrow\quad \langle p_c^2\rangle \;=\; \frac{\int \mathrm{d}^3p\,\vec{p}^{\,2}\,\psi_0(\vec{p}^{\,2})}{\int \mathrm{d}^3p\,\psi_0(\vec{p}^{\,2})} \;=\; \frac{3}{R^2}$$

Thus, numerically

$$\left.\begin{array}{rcl} R^2 \;=\; 12\,\text{GeV}^{-2} & \Longrightarrow & \langle p_c^2\rangle \;\simeq\; 0.25\,\text{GeV}^2 \\ m_{\eta_c} \;\simeq\; 3\,\text{GeV} & \Longrightarrow & m_c \;\simeq\; \dfrac{m_{\eta_c}}{2} \;\simeq\; 1.5\,\text{GeV} \end{array}\right\} \quad\Longrightarrow\quad \frac{\langle p_c^2\rangle}{4\,m_c^2} \;\simeq\; \frac{1}{32}$$

We can see that the insertion of a γ_0 inside a $\bar{c}\gamma_5 c$ correlator creates a very small effect. Notice finally that if we increase the meson radius R^2, then $\langle p_c^2\rangle$ decreases and the effect becomes even more smaller.
To conclude, the insertion a γ_0 matrix has no effect in this case.

C.3.2 The $\bar{c}\gamma_5\gamma_i D_i c$ vs $\bar{c}\gamma_0\gamma_5\gamma_i D_i c$ case

Considering (C.4) and since $\langle p_i\,p_j\rangle \;=\; 0$ for $i \neq j$, the contribution of $\bar{c}\gamma_5\gamma_i D_i c$ should be non-existent.
On the other hand, for the $\bar{c}\gamma_0\gamma_5\gamma_i D_i c$ operator, if we take

$$\langle p_{c_i}^2\rangle \;=\; \frac{1}{3}\,\langle p_c^2\rangle \qquad \text{(isotropy of the lattice)}$$

then we can infer roughly from (C.5) that

$$\bar{c}\gamma_0\gamma_5\gamma_i D_i c \;\rightsquigarrow\; -c_1^T\sigma_2 c_1\,\frac{\langle \vec{p}_{c_i}^{\,2}\rangle}{m_c} \;\simeq\; -c_1^T\sigma_2 c_1 \times \frac{0.25}{3\times 1.5} \;\sim\; 0.055\,\text{GeV}$$

If we translate this value in lattice units with $a \;=\; 0.1\,\text{fm} \;=\; 0.5\,\text{GeV}^{-1}$, we arrive at a factor of 0.11 (to be multiplied by 3 if we consider all the directions) which is clearly non-zero.
Comparing both situations, we can see that, for this correlator containing a derivative, inserting a γ_0 matrix changes drastically its behaviour.

Appendix D

Charmonium on the Lattice: Raw Data

Raw Data: Mass and Decay Constants

We collect in Table D.1 the values of η_c and J/ψ masses and decay constants extracted at each ensemble of the analysis, as well as the ratios of masses and decay constants $m_{\eta_c(2S)}/m_{\eta_c}$, $m_{\psi(2S)}/m_{J/\psi}$, $f_{\eta_c(2S)}/f_{\eta_c}$ and $f_{\psi(2S)}/f_{J/\psi}$.

id	$[t_{\text{min}}, t_{\text{max}}](P)$	am_{η_c}	af_{η_c}	$[t_{\text{min}}, t_{\text{max}}](V)$	$am_{J/\psi}$	$af_{J/\psi}$
E5	[11-29]	0.9836(3)	0.1246(16)	[11-29]	1.0202(7)	0.1499(11)
F6	[11-46]	0.9870(1)	0.1236(5)	[11-46]	1.0233(4)	0.1471(9)
F7	[11-45]	0.9855(1)	0.1233(3)	[11-45]	1.0209(3)	0.1460(5)
G8	[12-55]	0.9861(1)	0.1231(3)	[12-55]	1.0217(2)	0.1454(5)
N6	[13-46]	0.7284(3)	0.0944(6)	[13-46]	0.7547(6)	0.1059(8)
O7	[16-55]	0.7297(1)	0.0927(3)	[16-55]	0.7555(3)	0.1037(4)

id	$[t_{\text{min}}, t_{\text{max}}](P')$	$m_{\eta_c(2S)/m_{\eta_c}}$	$f_{\eta_c(2S)}/f_{\eta_c}$	$[t_{\text{min}}, t_{\text{max}}](V')$	$m_{\psi(2S)}/m_{J/\psi}$	$f_{\psi(2S)}/f_{J/\psi}$
E5	[6-13]	1.258(5)	0.67(10)	[6-13]	1.235(5)	0.99(6)
F6	[6-13]	1.257(3)	0.65(4)	[6-13]	1.233(4)	0.95(4)
F7	[6-13]	1.254(2)	0.67(2)	[6-13]	1.233(3)	0.98(2)
G8	[8-15]	1.235(3)	0.57(4)	[8-15]	1.213(3)	0.82(4)
N6	[8-15]	1.290(4)	0.75(6)	[8-15]	1.270(4)	1.09(7)
O7	[8-15]	1.257(4)	0.74(4)	[8-15]	1.236(5)	1.09(5)

TABLE D.1: Masses and decays constants of η_c, $\eta_c(2S)$, J/ψ and $\psi(2S)$, in lattice units, extracted on each CLS ensemble used in our analysis.

Bibliography

[1] C. Patrignani et al. "Review of Particle Physics". In: *Chin. Phys.* C40.10 (2016), p. 100001.

[2] M. B. Voloshin. "Charmonium". In: *Prog. Part. Nucl. Phys.* 61 (2008), pp. 455–511. arXiv: 0711.4556 [hep-ph].

[3] E. S. Swanson. "Hadron Spectroscopy – Theory". In: *Particles and fields. Proceedings, Meeting of the Division of the American Physical Society, DPF 2009, Detroit, USA, July 26-31, 2009*. 2009. arXiv: 0910.3704 [hep-ph].

[4] E. S. Swanson. "Heavy charmonium mini-review". In: *QCD and high energy interactions. Proceedings, 44th Rencontres de Moriond, La Thuile, Italy, March 14-21, 2009*. 2009, pp. 103–106.

[5] N. Brambilla et al. "Heavy quarkonium: progress, puzzles, and opportunities". In: *Eur. Phys. J.* C71 (2011), p. 1534. arXiv: 1010.5827 [hep-ph].

[6] K. M. Ecklund et al. "Two-Photon Widths of the chi(cJ) States of Charmonium". In: *Phys. Rev.* D78 (2008), p. 091501. arXiv: 0803.2869 [hep-ex].

[7] L.-Y. Xiao et al. "A new decay mode of higher charmonium". In: (2018). arXiv: 1805.07096 [hep-ph].

[8] B. Aubert et al. "Evidence for the $\eta_b(1S)$ Meson in Radiative $\Upsilon(2S)$ Decay". In: *Phys. Rev. Lett.* 103 (2009), p. 161801. arXiv: 0903.1124 [hep-ex].

[9] M. Petric et al. "Search for leptonic decays of D^0 mesons". In: *Phys. Rev.* D81 (2010), p. 091102. arXiv: 1003.2345 [hep-ex].

[10] S. E. Csorna et al. "Evidence of new states decaying into $\chi_c'\pi$". In: *Phys. Rev. Lett.* 86 (2001), pp. 4243–4246. arXiv: 0012020 [hep-ex].

[11] J. T. Laverty, S. F. Radford, and W. W. Repko. "gamma gamma and gg rates for equal mass heavy quarkonia". In: (2009). arXiv: 0901.3917 [hep-ph].

[12] D. Diakonov, M. G. Ryskin, and A. G. Shuvaev. "Gluon distribution at very small x from C-even charmonia production at the LHC". In: *JHEP* 02 (2013), p. 069. arXiv: 1211.1578 [hep-ph].

[13] G. Krein, A. W. Thomas, and K. Tsushima. "Nuclear-bound quarkonia and heavy-flavor hadrons". In: *Prog. Part. Nucl. Phys.* 100 (2018), pp. 161–210. arXiv: 1706.02688 [hep-ph].

[14] J. C. Amal et al. "Charmonium states in strong magnetic fields". In: (2018). arXiv: 1803.04322 [nucl-th].

[15] K. G. Wilson. "Confinement of Quarks". In: *Phys. Rev.* D10 (1974), pp. 2445–2459.

[16] G. Aad et al. "Combined Measurement of the Higgs Boson Mass in pp Collisions at $\sqrt{s} = 7$ and 8 TeV with the ATLAS and CMS Experiments". In: *Phys. Rev. Lett.* 114 (2015), p. 191803. arXiv: 1503.07589 [hep-ex].

[17] F. Englert and R. Brout. "Broken Symmetry and the Mass of Gauge Vector Mesons". In: *Phys. Rev. Lett.* 13 (1964), pp. 321–323.

[18] G. S. Guralnik, C. R. Hagen, and T. W. B. Kibble. "Global Conservation Laws and Massless Particles". In: *Phys. Rev. Lett.* 13 (1964), pp. 585–587.

[19] P. W. Higgs. "Broken Symmetries and the Masses of Gauge Bosons". In: *Phys. Rev. Lett.* 13 (1964), pp. 508–509.

[20] P. W. Higgs. "Spontaneous Symmetry Breakdown without Massless Bosons". In: *Phys. Rev.* 145 (1966), pp. 1156–1163.

[21] M. Thomson. *Modern particle physics*. New York: Cambridge University Press, 2013.

[22] R. F. Streater and A. S. Wightman. "PCT, spin and statistics, and all that". In: *Redwood City, USA: Addison-Wesley (1989) 207 p. (Advanced book classics)* (1989).

[23] K. Osterwalder and R. Schrader. "Axioms for Euclidean Green's Functions". In: *Commun. Math. Phys.* 31 (1973), pp. 83–112.

[24] K. Osterwalder and R. Schrader. "Axioms for Euclidean Green's Functions. 2." In: *Commun. Math. Phys.* 42 (1975), p. 281.

[25] M. Luscher and S. Schaefer. "Lattice QCD without topology barriers". In: *JHEP* 07 (2011), p. 036. arXiv: 1105.4749 [hep-lat].

[26] C. Gattringer and C. B. Lang. "Quantum chromodynamics on the lattice". In: *Lect. Notes Phys.* 788 (2010), pp. 1–343.

[27] E. Seiler. "Gauge Theories as a Problem of Constructive Quantum Field Theory and Statistical Mechanics". In: *Lect. Notes Phys.* 159 (1982), pp. 1–192.

[28] K. Symanzik. "Continuum Limit and Improved Action in Lattice Theories. 1. Principles and phi**4 Theory". In: *Nucl. Phys.* B226 (1983), pp. 187–204.

[29] K. Symanzik. "Continuum Limit and Improved Action in Lattice Theories. 2. O(N) Nonlinear Sigma Model in Perturbation Theory". In: *Nucl. Phys.* B226 (1983), pp. 205–227.

[30] P. Weisz. "Continuum Limit Improved Lattice Action for Pure Yang-Mills Theory. 1." In: *Nucl. Phys.* B212 (1983), pp. 1–17.

[31] A. Papa. "Fixed point actions and on-shell tree level Symanzik improvement". In: *Phys. Lett.* B437 (1998), pp. 123–130. arXiv: 9803014 [hep-lat].

[32] Y. Iwasaki. "Renormalization Group Analysis of Lattice Theories and Improved Lattice Action. II. Four-dimensional non-Abelian SU(N) gauge model". In: (1983). arXiv: 1111.7054 [hep-lat].

[33] K. G. Wilson. "Quarks and Strings on a Lattice". In: *New Phenomena in Subnuclear Physics: Proceedings, International School of Subnuclear Physics, Erice, Sicily, Jul 11-Aug 1 1975. Part A*. 1975, p. 99.

[34] H. Panagopoulos and Y. Proestos. "The Critical hopping parameter in O(a) improved lattice QCD". In: *Phys. Rev.* D65 (2002), p. 014511. arXiv: 0108021 [hep-lat].

[35] B. Sheikholeslami and R. Wohlert. "Improved Continuum Limit Lattice Action for QCD with Wilson Fermions". In: *Nucl. Phys.* B259 (1985), p. 572.

[36] M. Luscher and P. Weisz. "O(a) improvement of the axial current in lattice QCD to one loop order of perturbation theory". In: *Nucl. Phys.* B479 (1996), pp. 429–458. arXiv: 9606016 [hep-lat].

[37] K. Jansen and R. Sommer. "O(a) improvement of lattice QCD with two flavors of Wilson quarks". In: *Nucl. Phys.* B530 (1998). [Erratum: Nucl. Phys.B643,517(2002)], pp. 185–203. arXiv: 9803017 [hep-lat].

[38] T. DeGrand and C. E. Detar. *Lattice methods for quantum chromodynamics*. New Jersey, USA: World Scientific (2006) 345 p, 2006.

[39] H. B. Nielsen and M. Ninomiya. "No Go Theorem for Regularizing Chiral Fermions". In: *Phys. Lett.* 105B (1981), pp. 219–223.

[40] H. B. Nielsen and M. Ninomiya. "Absence of Neutrinos on a Lattice. 2. Intuitive Topological Proof". In: *Nucl. Phys.* B193 (1981), pp. 173–194.

[41] P. H. Ginsparg and K. G. Wilson. "A Remnant of Chiral Symmetry on the Lattice". In: *Phys. Rev.* D25 (1982), p. 2649.

[42] M. Luscher. "Exact chiral symmetry on the lattice and the Ginsparg-Wilson relation". In: *Phys. Lett.* B428 (1998), pp. 342–345. arXiv: 9802011 [hep-lat].

[43] R. Frezzotti and G. C. Rossi. "Chirally improving Wilson fermions. 1. O(a) improvement". In: *JHEP* 08 (2004), p. 007. arXiv: 0306014 [hep-lat].

[44] R. Frezzotti et al. "A local formulation of lattice QCD without unphysical fermion zero modes". In: *Nuclear Physics B - Proceedings Supplements* 83-84 (2000). Proceedings of the XVIIth International Symposium on Lattice Field Theory, pp. 941 –946.

[45] R. Frezzotti et al. "Lattice QCD with a chirally twisted mass term". In: *JHEP* 08 (2001), p. 058. arXiv: 0101001 [hep-lat].

[46] A. Shindler. "Twisted mass lattice QCD". In: *Phys. Rept.* 461 (2008), pp. 37–110. arXiv: 0707.4093 [hep-lat].

[47] P. Dimopoulos et al. "Flavour symmetry restoration and kaon weak matrix elements in quenched twisted mass QCD". In: *Nucl. Phys.* B776 (2007), pp. 258–285. arXiv: 0702017 [hep-lat].

[48] S. Duane et al. "Hybrid Monte Carlo". In: *Phys. Lett.* B195 (1987), pp. 216–222.

[49] W. K. Hastings. "Monte Carlo Sampling Methods Using Markov Chains and Their Applications". In: *Biometrika* 57 (1970), pp. 97–109.

[50] T. Lippert. "The Hybrid Monte Carlo algorithm for quantum chromodynamics". In: (1997). [Lect. Notes Phys.508,122(1998)]. arXiv: 9712019 [hep-lat].

[51] R. L. Dobrushin and S. B. Shlosman. "Absence of Breakdown of Continuous Symmetry in Two-Dimensional Models of Statistical Physics". In: *Commun. Math. Phys.* 42 (1975), pp. 31–40.

[52] G. P. Lepage. "The Analysis of Algorithms for Lattice Field Theory". In: *Boulder ASI 1989:97-120*. 1989, pp. 97–120.

[53] J. Foley et al. "Practical all-to-all propagators for lattice QCD". In: *Comput. Phys. Commun.* 172 (2005), pp. 145–162. arXiv: 0505023 [hep-lat].

[54] M. Peardon et al. "A Novel quark-field creation operator construction for hadronic physics in lattice QCD". In: *Phys. Rev.* D80 (2009), p. 054506. arXiv: 0905.2160 [hep-lat].

[55] H. Hamber and G. Parisi. "Numerical Estimates of Hadronic Masses in a Pure SU(3) Gauge Theory". In: *Phys. Rev. Lett.* 47 (1981), p. 1792.

[56] E. Marinari, G. Parisi, and C. Rebbi. "Computer Estimates of Meson Masses in SU(2) Lattice Gauge Theory". In: *Phys. Rev. Lett.* 47 (1981), p. 1795.

[57] B. Povh et al. *Particles and nuclei: An Introduction to the physical concepts*. Graduate Texts in Physics. Springer, 1995.

[58] R. Baron et al. "Status of ETMC simulations with $N_f = 2+1+1$ twisted mass fermions". In: *PoS* LATTICE2008 (2008), p. 094. arXiv: 0810.3807 [hep-lat].

[59] R. Baron et al. "First results of ETMC simulations with $N_f = 2+1+1$ maximally twisted mass fermions". In: *PoS* LAT2009 (2009), p. 104. arXiv: 0911.5244 [hep-lat].

[60] F. Farchioni et al. "Pseudoscalar decay constants from $N_f = 2+1+1$ twisted mass lattice QCD". In: *PoS* LATTICE2010 (2010), p. 128. arXiv: 1012.0200 [hep-lat].

[61] C.-K. Chow and S.-J. Rey. "Quenched and partially quenched chiral perturbation theory for vector and tensor mesons". In: *Nucl. Phys.* B528 (1998), pp. 303–321. arXiv: 9708432 [hep-ph].

[62] M. Creutz. "Partial quenching and chiral symmetry breaking". In: *PoS* LATTICE2014 (2014), p. 070. arXiv: 1410.0883 [hep-lat].

[63] S. Gusken et al. "Nonsinglet Axial Vector Couplings of the Baryon Octet in Lattice QCD". In: *Phys. Lett.* B227 (1989), pp. 266–269.

[64] D. K. Asit, A. Harindranath, and J. Maiti. "Investigation of Lattice QCD with Wilson fermions with Gaussian Smearing". In: (2007). arXiv: 0712.4354 [hep-lat].

[65] M. Albanese et al. "Glueball Masses and String Tension in Lattice QCD". In: *Phys. Lett.* B192 (1987), pp. 163–169.

[66] F. D. R. Bonnet et al. "Improved smoothing algorithms for lattice gauge theory". In: *Phys. Rev.* D65 (2002), p. 114510. arXiv: hep-lat/0106023 [hep-lat].

[67] P. Fritzsch et al. "The strange quark mass and Lambda parameter of two flavor QCD". In: *Nucl. Phys.* B865 (2012), pp. 397–429. arXiv: 1205.5380 [hep-lat].

[68] R. Sommer. "A New way to set the energy scale in lattice gauge theories and its applications to the static force and alpha-s in SU(2) Yang-Mills theory". In: *Nucl. Phys.* B411 (1994), pp. 839–854. arXiv: 9310022 [hep-lat].

[69] K. Jansen. "Lattice QCD: A Critical status report". In: *PoS* LATTICE2008 (2008), p. 010. arXiv: 0810.5634 [hep-lat].

[70] K. Huitu, H. Kurki-Suonio, and J. Maalampi, eds. *Proceedings, International Europhysics Conference on High energy physics (EPS-HEP 1999)*. 2000.

[71] M. Luscher. "Computational Strategies in Lattice QCD". In: *Modern perspectives in lattice QCD: Quantum field theory and high performance computing. Proceedings, International School, 93rd Session, Les Houches, France, August 3-28, 2009*. 2010, pp. 331–399. arXiv: 1002.4232 [hep-lat].

[72] S. Aoki et al. "Finite size effects of hadron masses in lattice QCD: A Comparative study for quenched and full QCD simulations". In: *Phys. Rev.* D50 (1994), pp. 486–494.

[73] M. Fukugita et al. "Finite size effect in lattice QCD hadron spectroscopy". In: *Phys. Rev. Lett.* 68 (1992), pp. 761–764.

[74] G. Colangelo, S. Durr, and C. Haefeli. "Finite volume effects for meson masses and decay constants". In: *Nucl. Phys.* B721 (2005), pp. 136–174. arXiv: 0503014 [hep-lat].

[75] J. R. Green et al. "Nucleon Structure from Lattice QCD Using a Nearly Physical Pion Mass". In: *Phys. Lett.* B734 (2014), pp. 290–295. arXiv: 1209.1687 [hep-lat].

[76] J. Gasser and H. Leutwyler. "Chiral Perturbation Theory to One Loop". In: *Annals Phys.* 158 (1984), p. 142.

[77] J. L. Goity. "Chiral perturbation theory for SU(3) breaking in heavy meson systems". In: *Phys. Rev.* D46 (1992), pp. 3929–3936. arXiv: 9206230 [hep-ph].

[78] Y. Aoki. "Non-perturbative renormalization in lattice QCD". In: *PoS* LAT2009 (2009), p. 012. arXiv: 1005.2339 [hep-lat].

[79] G. Martinelli et al. "A General method for nonperturbative renormalization of lattice operators". In: *Nucl. Phys.* B445 (1995), pp. 81–108. arXiv: 9411010 [hep-lat].

[80] Y. Bi et al. "RI/MOM and RI/SMOM renormalization of overlap quark bilinears on domain wall fermion configurations". In: *Phys. Rev.* D97.9 (2018), p. 094501. arXiv: 1710.08678 [hep-lat].

[81] E. Franco and V. Lubicz. "Quark mass renormalization in the MS-bar and RI schemes up to the NNLO order". In: *Nucl. Phys.* B531 (1998), pp. 641–651. arXiv: 9803491 [hep-ph].

[82] J. A. Gracey. "Three loop anomalous dimension of nonsinglet quark currents in the RI-prime scheme". In: *Nucl. Phys.* B662 (2003), pp. 247–278. arXiv: 0304113 [hep-ph].

[83] M. Bruno et al. "QCD Coupling from a Nonperturbative Determination of the Three-Flavor Λ Parameter". In: *Phys. Rev. Lett.* 119.10 (2017), p. 102001. arXiv: 1706.03821 [hep-lat].

[84] M. Dalla Brida et al. "A non-perturbative exploration of the high energy regime in $N_f = 3$ QCD". In: *Eur. Phys. J.* C78.5 (2018), p. 372. arXiv: 1803.10230 [hep-lat].

[85] A. Bode, P. Weisz, and U. Wolff. "Two loop computation of the Schrodinger functional in lattice QCD". In: *Nucl. Phys.* B576 (2000), pp. 517–539. arXiv: hep-lat/9911018 [hep-lat].

[86] M. Luscher et al. "The Schrodinger functional: A Renormalizable probe for nonAbelian gauge theories". In: *Nucl. Phys.* B384 (1992), pp. 168–228. arXiv: 9207009 [hep-lat].

[87] M. Della Morte et al. "Computation of the strong coupling in QCD with two dynamical flavors". In: *Nucl. Phys.* B713 (2005), pp. 378–406. arXiv: 0411025 [hep-lat].

[88] M. Della Morte et al. "Non-perturbative quark mass renormalization in two-flavor QCD". In: *Nucl. Phys.* B729 (2005), pp. 117–134. arXiv: 0507035 [hep-lat].

[89] S. Aoki et al. "Non-perturbative renormalization of quark mass in $N_f = 2 + 1$ QCD with the Schroedinger functional scheme". In: *JHEP* 08 (2010), p. 101. arXiv: 1006.1164 [hep-lat].

[90] M. Luscher. "The Schrodinger functional in lattice QCD with exact chiral symmetry". In: *JHEP* 05 (2006), p. 042. arXiv: 0603029 [hep-lat].

[91] M. Luscher et al. "Some new results in O(a) improved lattice QCD". In: *Nucl. Phys. Proc. Suppl.* 53 (1997), pp. 905–913. arXiv: hep-lat/9608049 [hep-lat].

[92] M. Luscher and U. Wolff. "How to Calculate the Elastic Scattering Matrix in Two-dimensional Quantum Field Theories by Numerical Simulation". In: *Nucl. Phys.* B339 (1990), pp. 222–252.

[93] D. Richards. "The excited-state spectrum of QCD through lattice gauge theory calculations". In: *J. Phys. Conf. Ser.* 403 (2012), p. 012044.

[94] C. Michael and C. Urbach. "Neutral mesons and disconnected diagrams in Twisted Mass QCD". In: *PoS* LATTICE2007 (2007), p. 122. arXiv: 0709.4564 [hep-lat].

[95] C. McNeile and C. Michael. "Decay width of light quark hybrid meson from the lattice". In: *Phys. Rev.* D73 (2006), p. 074506. arXiv: 0603007 [hep-lat].

[96] C. Alexandrou et al. "Evaluation of disconnected quark loops for hadron structure using GPUs". In: *Comput. Phys. Commun.* 185 (2014), pp. 1370–1382. arXiv: 1309.2256 [hep-lat].

[97] A. Abdel-Rehim et al. "Disconnected quark loop contributions to nucleon observables in lattice QCD". In: *Phys. Rev.* D89.3 (2014), p. 034501. arXiv: 1310.6339 [hep-lat].

[98] R. Gupta. "Introduction to lattice QCD: Course". In: *Probing the standard model of particle interactions. Proceedings, Summer School in Theoretical Physics, NATO Advanced Study Institute, 68th session, Les Houches, France, July 28-September 5, 1997. Pt. 1, 2*. 1997, pp. 83–219. arXiv: 9807028 [hep-lat].

[99] M. Della Morte, R. Sommer, and S. Takeda. "On cutoff effects in lattice QCD from short to long distances". In: *Phys. Lett.* B672 (2009), pp. 407–412. arXiv: 0807.1120 [hep-lat].

[100] M. Della Morte et al. "Non-perturbative renormalization of the axial current with dynamical Wilson fermions". In: *JHEP* 07 (2005), p. 007. arXiv: 0505026 [hep-lat].

[101] B. Blossier et al. "On the generalized eigenvalue method for energies and matrix elements in lattice field theory". In: *JHEP* 04 (2009), p. 094. arXiv: 0902.1265 [hep-lat].

[102] G. P. Engel et al. "Meson and baryon spectrum for QCD with two light dynamical quarks". In: *Phys. Rev.* D82 (2010), p. 034505. arXiv: 1005.1748 [hep-lat].

[103] R. G. Edwards et al. "Excited state baryon spectroscopy from lattice QCD". In: *Phys. Rev.* D84 (2011), p. 074508. arXiv: 1104.5152 [hep-ph].

[104] M. S. Mahbub et al. "Structure and Flow of the Nucleon Eigenstates in Lattice QCD". In: *Phys. Rev.* D87.9 (2013), p. 094506. arXiv: 1302.2987 [hep-lat].

[105] B. J. Owen et al. "Variational Approach to the Calculation of gA". In: *Phys. Lett.* B723 (2013), pp. 217–223. arXiv: 1212.4668 [hep-lat].

[106] J. Bulava, M. Donnellan, and R. Sommer. "On the computation of hadron-to-hadron transition matrix elements in lattice QCD". In: *JHEP* 01 (2012), p. 140. arXiv: 1108.3774 [hep-lat].

[107] B. Yoon et al. "Controlling Excited-State Contamination in Nucleon Matrix Elements". In: *Phys. Rev.* D93.11 (2016), p. 114506. arXiv: 1602.07737 [hep-lat].

[108] H.-W. Lin et al. "Lattice Calculations of Nucleon Electromagnetic Form Factors at Large Momentum Transfer". In: (2010). arXiv: 1005.0799 [hep-lat].

[109] F. James and M. Winkler. "MINUIT User's Guide". In: (2004).

[110] E. Follana et al. "Highly improved staggered quarks on the lattice, with applications to charm physics". In: *Phys. Rev.* D75 (2007), p. 054502. arXiv: hep-lat/0610092 [hep-lat].

[111] T. Burch et al. "Quarkonium mass splittings in three-flavor lattice QCD". In: *Phys. Rev.* D81 (2010), p. 034508. arXiv: 0912.2701 [hep-lat].

[112] C. DeTar. "Charmonium Spectroscopy from Lattice QCD". In: *Int. J. Mod. Phys. Conf. Ser.* 02 (2011), pp. 31–35. arXiv: 1101.0212 [hep-lat].

[113] J. J. Dudek et al. "Charmonium excited state spectrum in lattice QCD". In: *Phys. Rev.* D77 (2008), p. 034501. arXiv: 0707.4162 [hep-lat].

[114] G. Bali et al. "Spectra of heavy-light and heavy-heavy mesons containing charm quarks, including higher spin states for $N_f = 2 + 1$". In: *PoS* LATTICE2011 (2011), p. 135. arXiv: 1108.6147 [hep-lat].

[115] G. S. Bali, S. Collins, and C. Ehmann. "Charmonium spectroscopy and mixing with light quark and open charm states from n_F=2 lattice QCD". In: *Phys. Rev.* D84 (2011), p. 094506. arXiv: 1110.2381 [hep-lat].

[116] J. J. Aubert et al. "Experimental Observation of a Heavy Particle J". In: *Phys. Rev. Lett.* 33 (1974), pp. 1404–1406.

[117] J. E. Augustin et al. "Discovery of a Narrow Resonance in e^+e^- Annihilation". In: *Phys. Rev. Lett.* 33 (1974). [Adv. Exp. Phys.5,141(1976)], pp. 1406–1408.

[118] G. S. Abrams et al. "The Discovery of a Second Narrow Resonance in e+ e- Annihilation". In: *Phys. Rev. Lett.* 33 (1974). [Adv. Exp. Phys.5,150(1976)], pp. 1453–1455.

[119] J. J. Dudek and E. Rrapaj. "Charmonium in lattice QCD and the non-relativistic quark-model". In: *Phys. Rev.* D78 (2008), p. 094504. arXiv: 0809.2582 [hep-ph].

[120] A. B. Henriques. "Light Mesons With a Nonrelativistic Potential Model". In: *Z. Phys.* C18 (1983), p. 213.

[121] W. Lucha and F. F. Schoberl. "Phenomenological Aspects of Nonrelativistic Potential Models". In: (1989).

[122] S. K. Choi et al. "Observation of the eta(c)(2S) in exclusive B —> K K(S) K- pi+ decays". In: *Phys. Rev. Lett.* 89 (2002). [Erratum: Phys. Rev. Lett.89,129901(2002)], p. 102001. arXiv: 0206002 [hep-ex].

[123] B. Aubert et al. "Evidence for $X(3872) \to \psi_{2S}\gamma$ in $B^{\pm} \to X_{3872}K^{\pm}$ decays, and a study of $B \to c\bar{c}\gamma K$". In: *Phys. Rev. Lett.* 102 (2009), p. 132001. arXiv: 0809.0042 [hep-ex].

[124] S.-L. Zhu. "New hadron states". In: *Int. J. Mod. Phys.* E17 (2008), pp. 283–322. arXiv: 0703225 [hep-ph].

[125] S. L. Olsen. "What ' s new with the XYZ mesons?" In: *BES-Belle-CLEO-Babar 2007 Joint Workshop on Charm Physics Beijing, China, November 26-27, 2007*. 2008. arXiv: 0801.1153 [hep-ex].

[126] J. Zhang. "Charmonium Decays at BESIII". In: *Int. J. Mod. Phys. Conf. Ser.* 46 (2018), p. 1860025.

[127] J. S. Lange. "Results on Charmonium and Charmonium-like States at the Belle Experiment". In: *Proceedings, 14th International Conference on Hadron spectroscopy (Hadron 2011): Munich, Germany, June 13-17, 2011*. 2011. arXiv: 1109.1699 [hep-ex].

[128] S. Schrenk. "B-meson decay to charmonium". In: *Conf. Proc.* C9510211 (1995), pp. 587–589.

[129] D. Bettoni and R. Calabrese. "Charmonium spectroscopy". In: *Prog. Part. Nucl. Phys.* 54 (2005), pp. 615–651.

[130] J. Zhang. "Experimental overview of charmonium spectroscopy". In: *Proceedings, 6th International Workshop on Charm Physics (Charm 2013): Manchester, UK, August 31-September 4, 2013*. 2013. arXiv: 1311.3370 [hep-ex].

[131] F. A. Harris. "Charmonium Review". In: *Nucl. Phys. Proc. Suppl.* 167 (2007), pp. 83–86. arXiv: 0610011 [hep-ex].

[132] B. H. Wiik. "New particles in e+ e- annihilation". In: *Cargese Summer Institute: Hadron Structure and Lepton-Hadron Interactions Cargese, France, July 4-24, 1977*. 1977, pp. 59–199.

[133] H.-B. Li. "Highlights from BESIII experiment". In: *Proceedings, 14th International Conference on Hadron spectroscopy (Hadron 2011): Munich, Germany, June 13-17, 2011*. 2011. arXiv: 1108.5789 [hep-ex].

[134] J. Z. Bai et al. "Measurements of the mass and full width of the eta(c) meson". In: *Phys. Lett.* B555 (2003), pp. 174–180. arXiv: 0301004 [hep-ex].

[135] K. Nakamura et al. "Review of particle physics". In: *J. Phys.* G37 (2010), p. 075021.

[136] B. Aubert et al. "Measurements of the mass and width of the η_c meson and of an $\eta_c(2S)$ candidate". In: *Phys. Rev. Lett.* 92 (2004), p. 142002. arXiv: 0311038 [hep-ex].

[137] D. M. Asner et al. "Observation of eta-prime(c) production in gamma gamma fusion at CLEO". In: *Phys. Rev. Lett.* 92 (2004), p. 142001. arXiv: 0312058 [hep-ex].

[138] H. Nakazawa. "Recent two-photon results at Belle". In: *25th Lake Louise Winter Institute: Celebrating 25 years (LLWI 2010) Lake Louise, Alberta, Canada, February 15-20, 2010*. 2010. arXiv: 1006.1977 [hep-ex].

[139] A. D. Martin and M. G. Ryskin. "Advantages of exclusive $\gamma\gamma$ production to probe high mass systems". In: *J. Phys.* G43.4 (2016), 04LT02. arXiv: 1601.07774 [hep-ph].

[140] M. Ablikim et al. "Measurements of the mass and width of the η_c using $\psi' - > \gamma\eta_c$". In: *Phys. Rev. Lett.* 108 (2012), p. 222002. arXiv: 1111.0398 [hep-ex].

[141] S. L. Olsen. "News from BESIII". In: *PoS* BORMIO2017 (2017), p. 038. arXiv: 1203.4297 [nucl-ex].

[142] C. DeTar et al. "Charmonium mass splittings at the physical point". In: *PoS* LATTICE2012 (2012), p. 257. arXiv: 1211.2253 [hep-lat].

[143] K. Abe et al. "Observation of a near-threshold omega J/psi mass enhancement in exclusive B —> K omega J/psi decays". In: *Phys. Rev. Lett.* 94 (2005), p. 182002. arXiv: 0408126 [hep-ex].

[144] P. del Amo Sanchez et al. "Observation of $\eta_c(1S)$ and $\eta_c(2S)$ decays to $K^+K^-\pi^+\pi^-\pi^0$ in two-photon interactions". In: *Phys. Rev.* D84 (2011), p. 012004. arXiv: 1103.3971 [hep-ex].

[145] L. Wang. "Study of charmonium spectroscopy at BESIII". In: *Proceedings, 14th International Conference on Hadron spectroscopy (Hadron 2011): Munich, Germany, June 13-17, 2011*. 2011. arXiv: 1110.2560 [hep-ex].

[146] X.-R. Lu. "Study on the two-photon transition from psi(2S) to J/psi at BESIII". In: *Int. J. Mod. Phys.* A26 (2011), pp. 552–554.

[147] T. Skwarnicki. "Heavy quarkonium". In: *Int. J. Mod. Phys.* A19 (2004), pp. 1030–1045. arXiv: 0311243 [hep-ph].

[148] R Aaij et al. "Measurement of $\psi(2S)$ meson production in pp collisions at $\sqrt{s}$=7 TeV". In: *Eur. Phys. J.* C72 (2012), p. 2100. arXiv: 1204.1258 [hep-ex].

[149] G. Bailas et al. "On the D_s^* and charmonia leptonic decays". In: *EPJ Web Conf.* 175 (2018), p. 13002. arXiv: 1711.05661 [hep-lat].

[150] G. Bailas, B. Blossier, and V. Morénas. "Some hadronic parameters of charmonia in $N_f = 2$ lattice QCD". In: (2018). arXiv: 1803.09673 [hep-lat].

[151] L. Liu et al. "Excited and exotic charmonium spectroscopy from lattice QCD". In: *JHEP* 07 (2012), p. 126. arXiv: 1204.5425 [hep-ph].

[152] C. B. Lang et al. "Vector and scalar charmonium resonances with lattice QCD". In: *JHEP* 09 (2015), p. 089. arXiv: 1503.05363 [hep-lat].

[153] D. Bečirević et al. "Lattice QCD and QCD sum rule determination of the decay constants of η_c, J/ψ and h_c states". In: *Nucl. Phys.* B883 (2014), pp. 306–327. arXiv: 1312.2858 [hep-ph].

[154] J. J. Dudek et al. "Toward the excited meson spectrum of dynamical QCD". In: *Phys. Rev.* D82 (2010), p. 034508. arXiv: 1004.4930 [hep-ph].

[155] D. Mohler, S. Prelovsek, and R. M. Woloshyn. "$D\pi$ scattering and D meson resonances from lattice QCD". In: *Phys. Rev.* D87.3 (2013), p. 034501. arXiv: 1208.4059 [hep-lat].

[156] M. Kurth and R. Sommer. "Renormalization and O(a) improvement of the static axial current". In: *Nucl. Phys.* B597 (2001), pp. 488–518. arXiv: 0007002 [hep-lat].

[157] P. Fritzsch, J. Heitger, and N. Tantalo. "Non-perturbative improvement of quark mass renormalization in two-flavour lattice QCD". In: *JHEP* 08 (2010), p. 074. arXiv: 1004.3978 [hep-lat].

[158] M. Della Morte, R. Hoffmann, and R. Sommer. "Non-perturbative improvement of the axial current for dynamical Wilson fermions". In: *JHEP* 03 (2005), p. 029. arXiv: 0503003 [hep-lat].

[159] S. Sint and P. Weisz. "Further results on O(a) improved lattice QCD to one loop order of perturbation theory". In: *Nucl. Phys.* B502 (1997), pp. 251–268. arXiv: 9704001 [hep-lat].

[160] M. Guagnelli et al. "Nonperturbative results for the coefficients b(m) and b(a) - b(P) in O(a) improved lattice QCD". In: *Nucl. Phys.* B595 (2001), pp. 44–62. arXiv: 0009021 [hep-lat].

[161] M. Luscher et al. "Nonperturbative O(a) improvement of lattice QCD". In: *Nucl. Phys.* B491 (1997), pp. 323–343. arXiv: 9609035 [hep-lat].

[162] M. Luscher. "Solution of the Dirac equation in lattice QCD using a domain decomposition method". In: *Comput. Phys. Commun.* 156 (2004), pp. 209–220. arXiv: 0310048 [hep-lat].

[163] M. Luscher. "Schwarz-preconditioned HMC algorithm for two-flavour lattice QCD". In: *Comput. Phys. Commun.* 165 (2005), pp. 199–220. arXiv: 0409106 [hep-lat].

[164] M. Luscher. "Deflation acceleration of lattice QCD simulations". In: *JHEP* 12 (2007), p. 011. arXiv: 0710.5417 [hep-lat].

[165] M. Marinkovic and S. Schaefer. "Comparison of the mass preconditioned HMC and the DD-HMC algorithm for two-flavour QCD". In: *PoS* LATTICE2010 (2010), p. 031. arXiv: 1011.0911 [hep-lat].

[166] H. B. Meyer et al. "Exploring the HMC trajectory-length dependence of autocorrelation times in lattice QCD". In: *Comput. Phys. Commun.* 176 (2007), pp. 91–97. arXiv: 0606004 [hep-lat].

[167] M. Foster and C. Michael. "Hadrons with a heavy color adjoint particle". In: *Phys. Rev.* D59 (1999), p. 094509. arXiv: 9811010 [hep-lat].

[168] A. A. Pivovarov. "Running electromagnetic coupling constant: Low-energy normalization and the value at M(Z)". In: *Phys. Atom. Nucl.* 65 (2002), pp. 1319–1340. arXiv: 0011135 [hep-ph].

[169] O. Lakhina and E. S. Swanson. "Dynamic properties of charmonium". In: *Phys. Rev.* D74 (2006), p. 014012. arXiv: 0603164 [hep-ph].

[170] W. Lucha and D. Melikhov. "The $\gamma^*\gamma^* \to \eta_c$ transition form factor". In: *Phys. Rev.* D86 (2012), p. 016001. arXiv: 1205.4587 [hep-ph].

[171] J. P. Lansberg and T. N. Pham. "Two-photon width of eta(c) and eta(c)-prime from heavy-quark spin symmetry". In: *Phys. Rev.* D74 (2006), p. 034001. arXiv: 0603113 [hep-ph].

[172] T. Feldmann and P. Kroll. "A Perturbative approach to the eta(c) gamma transition form-factor". In: *Phys. Lett.* B413 (1997), pp. 410–415. arXiv: 9709203 [hep-ph].

[173] H. Na et al. "The $D \to K, l\nu$ Semileptonic Decay Scalar Form Factor and $|V_{cs}|$ from Lattice QCD". In: *Phys. Rev.* D82 (2010), p. 114506. arXiv: 1008.4562 [hep-lat].

[174] C. McNeile et al. "High-Precision c and b Masses, and QCD Coupling from Current-Current Correlators in Lattice and Continuum QCD". In: *Phys. Rev.* D82 (2010), p. 034512. arXiv: 1004.4285 [hep-lat].

[175] H. Na et al. "$|V_{cd}|$ from D Meson Leptonic Decays". In: *Phys. Rev.* D86 (2012), p. 054510. arXiv: 1206.4936 [hep-lat].

[176] J. Koponen, C. T. H. Davies, and G. Donald. "D to K and D to pi semileptonic form factors from Lattice QCD". In: *Proceedings, 5th International Workshop on Charm Physics (Charm 2012): Honolulu, Hawaii, USA, May 14-17, 2012*. 2012. arXiv: 1208.6242 [hep-lat].

[177] C. Doran et al. "Lie groups as spin groups". In: *J. Math. Phys.* 34.8 (1993), pp. 3642–3669.

[178] H. Wittig. "Lattice gauge theory". In: *Proceedings, International Europhysics Conference on High energy physics (EPS-HEP 1999): Tampere, Finland, July 15-21, 1999*. 1999, pp. 181–200. arXiv: 9911400 [hep-ph].

[179] D. Bečirević, M. Kruse, and F. Sanfilippo. "Lattice QCD estimate of the $\eta_c(2S) \to J/\psi\gamma$ decay rate". In: *JHEP* 05 (2015), p. 014. arXiv: 1411.6426 [hep-lat].

[180] D. Bečirević et al. "D-meson decay constants and a check of factorization in non-leptonic B-decays". In: *JHEP* 02 (2012), p. 042. arXiv: 1201.4039 [hep-lat].

[181] B. Blossier, J. Heitger, and M. Post. "Leptonic D_s decays in two-flavour lattice QCD". In: (2018). arXiv: 1803.03065 [hep-lat].

[182] G. C. Donald et al. "Prediction of the D_s^* width from a calculation of its radiative decay in full lattice QCD". In: *Phys. Rev. Lett.* 112 (2014), p. 212002. arXiv: 1312.5264 [hep-lat].

[183] V. Lubicz, A. Melis, and S. Simula. "Masses and decay constants of D*$_{(s)}$ and B*$_{(s)}$ mesons with $N_f = 2+1+1$ twisted mass fermions". In: *Phys. Rev.* D96.3 (2017), p. 034524. arXiv: 1707.04529 [hep-lat].

[184] B. Colquhoun et al. "Υ and Υ′ Leptonic Widths, a_μ^b and m_b from full lattice QCD". In: *Phys. Rev.* D91.7 (2015), p. 074514. arXiv: 1408.5768 [hep-lat].

[185] G. C. Branco et al. "Theory and phenomenology of two-Higgs-doublet models". In: *Phys. Rept.* 516 (2012), pp. 1–102. arXiv: 1106.0034 [hep-ph].

[186] D. Bečirević et al. "Seeking a CP -odd Higgs boson via $h \to \eta_{c,b}\ell^+\ell^-$". In: *Phys. Rev.* D97.1 (2018), p. 015008. arXiv: 1705.01112 [hep-ph].

[187] D. Bečirević and F. Sanfilippo. "Lattice QCD study of the radiative decays $J/\psi \to \eta_c\gamma$ and $h_c \to \eta_c\gamma$". In: *JHEP* 01 (2013), p. 028. arXiv: 1206.1445 [hep-lat].

[188] S. Andreas et al. "Constraints on a very light CP-odd Higgs of the NMSSM and other axion-like particles". In: *JHEP* 08 (2010), p. 003. arXiv: 1005.3978 [hep-ph].

[189] R. Dermisek and J. F. Gunion. "New constraints on a light CP-odd Higgs boson and related NMSSM Ideal Higgs Scenarios". In: *Phys. Rev.* D81 (2010), p. 075003. arXiv: 1002.1971 [hep-ph].

[190] F. Domingo, U. Ellwanger, and M.-A. Sanchis-Lozano. "Bottomoniom spectroscopy with mixing of eta(b) states and a light CP-odd Higgs". In: *Phys. Rev. Lett.* 103 (2009), p. 111802. arXiv: 0907.0348 [hep-ph].

[191] E. Fullana and M.-A. Sanchis-Lozano. "Hunting a light CP-odd non-standard Higgs boson through its tauonic decay at a (Super) B factory". In: *Phys. Lett.* B653 (2007), pp. 67–74. arXiv: 0702190 [hep-ph].

[192] G. Bali et al. "Pion structure from lattice QCD". In: *PoS* LATTICE2013 (2014), p. 447. arXiv: 1311.7639 [hep-lat].

[193] B. Blossier et al. "Pseudoscalar decay constants of kaon and D-mesons from $N_f = 2$ twisted mass Lattice QCD". In: *JHEP* 07 (2009), p. 043. arXiv: 0904.0954 [hep-lat].

[194] G. S. Bali et al. "Lattice simulations with $N_f = 2+1$ improved Wilson fermions at a fixed strange quark mass". In: *Phys. Rev.* D94.7 (2016), p. 074501. arXiv: 1606.09039 [hep-lat].

[195] Y.-C. Chen and T.-W. Chiu. "Lattice QCD with $N_f = 2+1+1$ domain-wall quarks". In: *Phys. Lett.* B767 (2017), pp. 193–198. arXiv: 1701.02581 [hep-lat].

[196] A. Le Yaouanc et al. *Hadron Transitions in the Quark Model*. New York: Gordon and Breach, 1988.